# Universidade do Algarve

Faculdade de Engenharia e Recursos Naturais


# Nanoparticle-Based Biosensors:

# Development and Application

Tese para a obtenção do grau de doutor no ramo de Ciências Biotecnológicas, especialidade de Biotecnologia Molecular


Raul Baltazar



Faro

2009

# Universidade do Algarve

Faculdade de Engenharia e Recursos Naturais

# Nanoparticle-Based Biosensors: Development and Application

Tese para a obtenção do grau de doutor no ramo de Ciências Biotecnológicas, especialidade de Biotecnologia Molecular

Raul Baltazar

**Orientador**: Doutor Guilherme Ferreira

*Constituição do Júri*:

***Presidente***: Reitor da Universidade do Algarve

**Vogais**:

Doutor João Pedro Estrela Rodrigues Conde;

Doutor Alfredo Jaime Cravador;

Doutor Tito da Silva Trindade (*relator*);

Doutor Guilherme Nuno de Passos Correia Matos Ferreira;

Doutor Carlos dos Santos Silva e Pereira de Lima (*relator*).

Faro

2009

# Abstract

The development of technologies for imaging systems is a key issue in Medical Bioengineering. Within that context, the establishment of methodologies to link biomolecules to metallic and/or semiconductor nanoparticles, generating biologically active colorimetric sensors, constitutes an important research field towards the detection of molecular interactions both *in vivo* and *in vitro*. This thesis deals with the study and application of nanoparticle-based colorimetric sensors, namely gold nanoparticles (AuNPs) and quantum dots (QDs), for the study of biomolecular interactions and for biosensing purposes.

AuNPs are well known for their strong interactions with light that result on surface plasmon resonances (SPRs) which are transduced by characteristic optical absorption profiles. The wavelength peak of those plasmon resonances is found to depend greatly on three major factors: the nanoparticles morphology, the dielectric characteristics of the medium in which the nanoparticles are embedded and the interparticle distances. Since the SPR peak shifts to higher wavelengths and broadens when nanoparticles are brought close together, due to interparticle plasmon coupling, the biorecognition-induced aggregation of AuNPs has become a very attractive tool as colorimetric transduction signal in a variety of biosensing platforms. In this thesis, the colorimetric signal changes generated upon AuNPs aggregation was explored for the development of strategies for immunosensing and DNA-detection.

QDs, on their hand, possess unique photophysical properties for the development of robust and efficient fluorescent sensors, including high quantum yields, broad absorption spectra, narrow size-tunable photoluminescent emissions and exceptional resistance to both photobleaching and chemical degradation. Additionally, scientific research over the last few years proved that these nanometer-sized semiconductor particles can be linked with a range of biomolecules (including: peptides, antibodies, nucleic acids, and small-molecule ligands) and be used as biological labels. In this thesis, a few critical steps were taken on the characterization of the QDs photoluminescence properties, namely: under long-term photo-excitation with laser light and, when exposed to range of different temperatures.

**Keywords**: gold nanoparticles; surface plasmon resonance; quantum dots; biosensing.

# Resumo

O desenvolvimento de tecnologias para sistemas de produção de imagem é de importância chave do ponto de vista da Bioengenharia Médica. Neste âmbito, o estabelecimento de metodologias para ligar moléculas biológicas a nanopartículas metálicas e/ou semiconductoras, gerando assim sensores colorimétricos biologicamente activos, é uma área científica de grande importância para a detecção de interacções moleculares tanto *in vivo* como *in vitro*. Nesta tese faz-se o estudo e a aplicação de sensores colorimétricos baseados em nanopartículas (nomeadamente: nanopartículas de ouro e *quantum dots*) para a detecção de interacções moleculares e no desenvolvimento de biosensores.

As nanopartículas de ouro são conhecidas pelas interacções fortes que têm com a luz, resultando em ressonâncias do plasmão de superfície que são transduzidas por um perfil característico no espectro de absorção óptica. O comprimento de onda a que se encontra o máximo dessas ressonâncias depende fortemente de três factores principais: a morfologia das nanopartículas, as características dieléctricas do meio no qual as partículas estão inseridas e a distância entre partículas. Devido ao acoplamento das ressonâncias das partículas que ocorre quando distância entre elas suficientemente reduzida, o pico da ressonância do plasmão alarga-se e é desviado para maiores comprimentos de onda. Por isso, a indução da agregação de nanopartículas de ouro através de reconhecimento biomolecular tem-se revelado como ferramenta geradora de sinais colorimétricos numa variedade cada vez maior de plataformas bio-sensoras. Nesta tese, os sinais colorimétricos gerados pela agregação de nanopartículas de ouro são explorados no desenvolvimento de estratégias para sensores imunológicos e para detecção de DNA.

Os *quantum dots* possuem propriedades fotofísicas únicas para o desenvolvimento de sensores de fluorescência robustos e eficientes. Estas propriedades incluem: altas eficiências quânticas, espectro de absorção largo, emissões foto-luminescentes com bandas estreitas cuja posição no espectro óptico é ajustável pelo ajuste do tamanho físico destas nanopartículas, e uma resistência excepcional tanto à perda de eficiência luminescente como à degradação química. Adicionalmente, nos últimos anos, a investigação científica tem vindo a provar que estas partículas semiconductoras de tamanho nanométrico podem ser ligadas a uma grande variedade de biomoléculas (incluindo: péptidos, anticorpos, ácidos nucleicos, e pequenas moléculas ligantes), permitindo o seu uso na marcação óptica dessas biomoleculas. Nesta tese, foram dados alguns passos críticos na caracterização das propriedades foto-luminescentes dos quantum dots, nomeadamente quando sujeitos a duas condições particulares: exposição à excitação laser por tempos prolongados, e exposição diferentes temperaturas.

**Palavras-chave:** nanopartículas de ouro, ressonância do plasmão de superfície, *quantum dots*; biosensores.

# Acknowledgments

Four years ago biotechnology seemed to me as an exotic and futuristic world. Today, I see it as a window that allows me to look inside a beaker and see a whole universe of atomic dimensions with amazing properties.

I am deeply grateful to Prof. Guilherme Ferreira, my supervisor, for a number of reasons, among which: for believing that, as a physicist, I could give a positive input into to the research developed in his laboratory as a member of his recently formed research team; for pushing me through in my scientific quest within the biotechnology world, even when I stumbled at the some difficulty; for his guidance; and, perhaps most of all, for teaching me to ask questions – the right questions! – and then to search for the answers.

I am grateful to my lab mates and friends: Luís Rosa, Luísa Pedro, Rogério Rodrigues, João Encarnação and more recently to Sandra Soares, first for their joyful team-spirit and second for helping me "getting this job done". I must devote a special thanks to Luís and to Luísa, for their continuous efforts (and unending patience!) in trying to make a biotechnologist out of me.

I thank to my closest friends outside the lab (Dário, Sandra, Patrick, Marlene, Rui, Zézinha, Viktor, Dina, Elsa, Helder, Gonçalo) who, in times of despair, told me: Fight! You can do it!

Thanks to my family for their spiritual support, their love and for believing in me. The words to thank my parents, Fernanda e António, are still to be invented! This achievement is yours.

I thank to my wife, Sónia, for her love and understanding, for keeping me in track towards what, in the end, matters - US.

I devote this work to my daughter, Lia. Her little smile, her happy laughing have the healing properties that no science can ever reach.

I acknowledge the Portuguese Foundation for Science and Technology, for my PhD grant number SFRH/BD/17286/2004 and for the funding to the projects POCTI/BIO/38922 and POCTI/CTM/37719.

# Index

# List of Tables

# List of Figures

# List of abbreviations

AuNP – gold nanoparticle

BSA – bovine

cDNA – complementary DNA

Cy - *cyanine*

DMF – Dimethylformamide

DNA – deoxyribonucleic acid

dsDNA – double-stranded deoxyribonucleic acid

DSU – Dithiobis-succinimydil undecanoate

EDC – 1-Ethyl-3-[3-dimethylaminopropyl]carbodiimide hydrochloride

EDL – electrical double layer

EDTA - ethylenediaminetetraacetic acid

FWHM – full width at half maximum

HA – haemagglutinin

IRIV – Immunopotentiating Reconstituted Influenza Virosome

$MgCl_2$ – magnesium chloride

NaCl – Sodium Chloride

NHS – N-hydroxysulfosuccinimide

RET – resonance energy transfer

SAM – self-assembled-monolayer

SH - thiol

SNP – single nucleotide polymorphism

SPR – surface plasmon resonance

ssDNA – single-stranded deoxyribonucleic acid

Tween-20 - Polysorbate 20

UV – ultraviolet light

UV-Vis – ultraviolet-visible light

# 1. Introduction

Nanotechnology (defined as the creation and utilization of materials, devices and systems through the control of matter on the nanometer scale) is a recent revolutionary development of science and engineering that is evolving at a very fast pace. It is driven by the desire to fabricate materials with novel and improved properties that are likely to impact virtually all areas of physical and chemical sciences, biological sciences, health sciences, and other interdisciplinary fields of science and engineering. Particularly, one of the major breakthroughs in nanotechnology science lies on the development of nanoparticles-based biomedicine applications. In that context, this dissertation presents studies performed aiming the design and development of nanoparticle-based biosensors.

## 1.1. Biosensors: a definition

From a general point of view, a biosensor may be defined as a measurement system, operating under the fundamental principles of biological recognition and sensing, consisting in two basic components: (1) a probe with a biological recognition element (the bioreceptor), which should provide the sensor with a high degree of selectivity and sensitivity towards the analyte to be detected and; (2) a transducer, which converts the interaction of the analyte with the bioreceptor into some kind of detectable and/or measurable signal (Vo-Dinh, 2004).

Transduction has been accomplished through a large variety of methods, and biosensors may be classified accordingly to the transduction methods employed. New types of transducers are constantly being developed for use in biosensors but, most forms of transduction can be categorized in one of the following main classes: (1) optical detection methods; (2)

electrochemical detection methods; (3) mass-based detection methods, and (4) voltaic and magnetic. Naturally, each of these main classes contains many different subclasses, creating a large number of possible transduction methods or combinations of methods. (Vo-Dinh, 2004).

Bioreceptors, on their hand, are key elements to the specificity and sensitivity on biosensor-based technologies, given that signal transduction by the biosensor is triggered as a consequence of the interaction of the bioreceptors with the target analyte of interest. The different existing bioreceptors are, at least, as numerous as the different analytes that have been detected in biosensing, and may be classified into five major categories: (1) antibody/antigen, (2) enzymes, (3) nucleic acids/DNA, (4) cellular structures/cells, and (5) biomimetic (Vo-Dinh, 2004).

## 1.2. Nanoparticles: a definition

Nanoparticles are, by definition, particles where all the three dimensions are at the nanometer scale (ranging from 1 to 100 nm) and are composed of up to $10^6$ atoms (Kreibig *et al.*, 2006). Since their size is intermediate between that of individual atoms and that of the bulk material, typically, these materials show behaviors that are intermediate between that of a macroscopic solid and that of an atomic or molecular system (Schmid, 1994).

Due to smallness of their size, nanoparticles have a very high percentage of surface atoms which translates in surface related properties (chemical and physical) that can be greatly affected if any modification is made in parameters such as: size, size dispersity, structure, chemical composition, particle coverage, particle shape or the dielectric constant of the medium surrounding the nanoparticle (Brust and Kiely, 2002; Schmid and Corain, 2003; Zhang *et al.*, 2003; Schmid *et al.*, 1999; Ratner and Ratner, 2003; Dabbousi *et al.*, 1997; Chan and Nie, 1998; Hines and Guyot-Sionnest, 1996). Therefore, nanoparticles are amenable to ‘‘tuning’’. Furthermore, the range of sizes of nanoparticles is comparable to that of the biomolecules encountered at the cellular level, which facilitates the development of biosensors that can probe, for instance, proteins, antibodies or DNA.

Their distinct properties and the fact that nowadays nanoparticles may be controllably synthesized in variety of materials (such as: gold, silver, platinum, iridium, palladium, iron oxide, etc.) and shapes (such as: spherical, triangular, cubical, pentagonal, rod-shaped, shells, ellipsoidal and so forth) allows them to find a large variety of applications in a number of fields

such as electronics (Thelander *et al.*, 2001), chemical (Darbha *et al.*,2008) and biological sensors (Simonian *et al.*,2005; Montmeat *et al.*, 2003; Pingarrón *et al.*, 2008; Stringer *et al.*, 2008), biotechnology (Cui *et al.*, 2005; Liu *et al.*, 2008; Dobrovolskaia *et al.*, 2009) and medicine (Huang *et al.*, 2005; Visaria *et al.*, 2006; Nath *et al.*, 2008), just to mention few.

On the current work, two types of spherical nanoparticles were addressed aiming biosensing applications, where biorecognition signals are transduced colorimetrically: gold nanoparticles (applications in chapters 3, 4 and 5) and semiconductor quantum dots (chapter 6). The following sections 1.3 and 1.4, detail the main characterizing properties of these two types of nanoparticles.

## 1.3. Gold Nanoparticles

Up until now, a variety of bio-functionalized metal nanoparticles has been produced and investigated for their potential applications in the biological field. From within those investigations, gold nanoparticles (AuNPs) have emerged as favorites in biomedical, biosensing, imaging and therapy applications owing to their biocompatibility, dimensions, ease of characterization and very high chemical reactivity at the nanometer scale, allowing surface modification reactions with a wide variety of chemical and biochemical vectors (Kell *et al.*, 2005; Xue *et al.*, 2005).

### 1.3.1. Surface Plasmon Resonance

Presently, it is widely recognized that both structural and electronic properties of solid state matter change as the samples sizes are diminished down to the nanometer scale. For instance, if a metal particle with bulk properties is reduced to a size of a few dozen or a few hundred atoms, the density of states in both the valence and conductions bands decreases to such an extent that electronic properties of the particles change dramatically. The justification is that, in a bulky metal, electrons are highly delocalized (least confined), because there is no separation between the valence and conduction bands (Figure 1.1a), which renders metals their conducting properties. As the size of the metal is decreased, the continuous density of electronic states in its band structure changes until, at small enough sizes, it is finally broken into discrete energy levels. At an initial “shrinking” stage, the electronic motion confinement produces a separation between the valence and the conduction bands such that the metal becomes a semiconductor

(Figure 1.1b). Even smaller particle sizes imply higher electronic confinement, increasing even further the separation of the energetic levels, which results on the formation well-defined bonding and anti-bonding molecular orbitals, and the material becomes an insulator (Figure 1.1c) (Tan *et al.*, 2004).

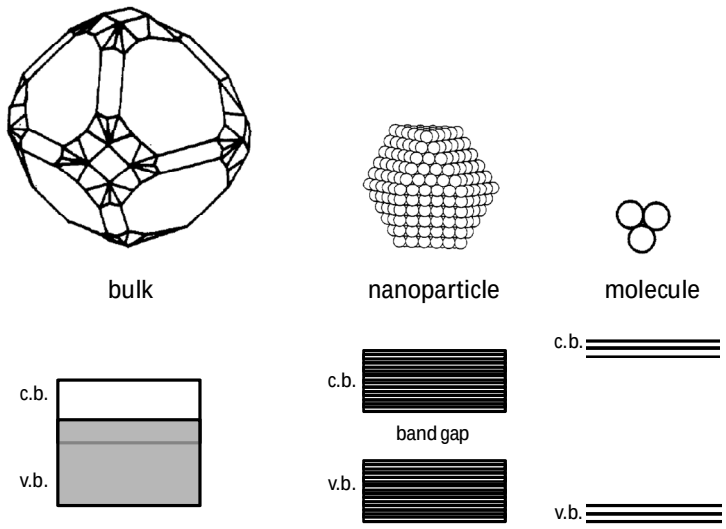


**Figure 1.1** - Illustration of the typical band structure of: (a) metal particle with bulk properties, (b) a large cluster of cubic close-packed atoms, and (c) a simple tri-atomic cluster. c.b. = conduction band; v.b. = valence band. (Adapted from: Schmid, 1992).

By decreasing the metal particle size below the electron mean-free-path (the average distance each electron travels between scattering collisions with the lattice centers in a bulk material), the conduction electrons in the metal become "not-free" (or confined). Hence, during their random motion, electrons are backscattered in the particle surfaces after penetrating into the potential barrier created by the unsaturated chemical bonds of the superficial metal atoms. Due to their extremely high densities and high levels of interactions, these confined electrons may be considered as members of a strongly coupled Fermi liquid (Kreibig *et al.*, 2006). Hence, they act collectively when experiencing an incident electric field, with an additional "in-phase motion" superimposing to the random individual movements of the electrons in the plasma. This leads to a dipole excitation across the nanoparticle due to the periodic "elongation" of the electron density beyond the surface defined by the outermost ions (Figure 1.2), giving rise to the appearance of a restoring Coulomb force that makes the electrons oscillate collectively with a particular time period – the so called "surface plasmon resonance" (SPR) – which results in intensive optical extinction of near-UV and visible light (Kreibig and Quinten, 2004; Ghosh and Pal, 2007).

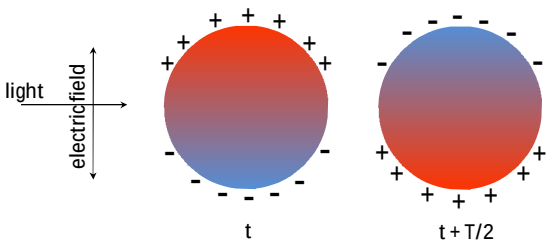


**Figure 1.2** – Scheme illustrating the oscillation of the surface plasmon dipole. The electric field of an incoming light wave induces a polarization of the (free) conduction electrons with respect to the much heavier ionic core of a spherical AuNP. The net charge difference occurs only at the nanoparticle surfaces, and act as restoring force. Consequently, a dipolar oscillation of the plasmon electrons is created with period ***T***. (Adapted from: Link and El-Sayed, 2000).

According to Mulvaney (Mulvany, 2001), in dilute dispersions, the surface plasmon absorption band of spherical nanoparticles much smaller than the wavelength of the incident light may be predicted by Equation 1.1, relating the amount of light scattered and/or absorbed by a particle in a certain solution with the properties of both the particle and the solvent.

$$C_{ext} = \frac{24\pi^2 R^3 \varepsilon_m^{3/2}}{\lambda} \frac{\varepsilon''}{(\varepsilon' + 2\varepsilon_m)^2 + \varepsilon''^2} \qquad \text{Equation 1.1}$$

Here, $\boldsymbol{\lambda}$ is the wavelength of the incident light, $\boldsymbol{R}$ is the particle radius, $\boldsymbol{\varepsilon_m}$ is the dielectric function of the medium in which the nanoparticles are dispersed, and $\boldsymbol{\varepsilon'}$ and $\boldsymbol{\varepsilon''}$ are the real and imaginary parts the particle's complex dielectric function, given by $\boldsymbol{\varepsilon = \varepsilon' + i\varepsilon'' = (n + ik)^2}$, where $\boldsymbol{n^2 = \varepsilon_m}$ is the refraction index and $\boldsymbol{k}$ is the absorption coefficient (Pérez-Luna *et al.*, 2004). If "free" electrons are considered (6s electrons of the conduction band in the case of gold), the real and imaginary parts of this function are given by:

$$\varepsilon' = \varepsilon_\infty - \frac{\omega_p^2}{\omega^2 + \omega_p^2} \qquad \text{Equation 1.2}$$

$$\varepsilon'' = \frac{\omega_d \omega_p^2}{\omega(\omega^2 + \omega_d^2)} \qquad \text{Equation 1.3}$$

where $\boldsymbol{\varepsilon_\infty}$ is the high frequency dielectric constant due to interband and core transitions, $\boldsymbol{\omega}$ is the

incident radiation frequency, $\boldsymbol{\omega_p}$ is the bulk plasma frequency, and $\boldsymbol{\omega_d}$ is the damping frequency given by:

$$\omega_d = \frac{\upsilon_F}{R_{bulk}} \qquad \text{Equation 1.4}$$

where $\boldsymbol{\upsilon_F}$ is the velocity of free electrons at the Fermi energy and $\boldsymbol{R_{bulk}}$ is the mean free path of the conduction electrons. Thus, if nanoparticles and/or solvent properties change, so does their complex dielectric function, producing the corresponding alterations on the surface plasmon absorption band as given by $\boldsymbol{C_{ext}}$.

Experimentally, it has been observed that within each metal type, the position and magnitude of the surface plasmon absorption band depends critically of three major factors (Link and El-Sayed, 1999; Templeton *et al.*, 2000; Rechberger *et al.*; 2003; Su *et al.*, 2003; Swanson and Billard, 2003): (1) the size and shape of the particles; (2) the dielectric properties of particles and solvent; and (3) inter-particle interactions.

As the nanoparticles radii become smaller than the electrons mean-free-path ($\boldsymbol{R} < \boldsymbol{R_{bulk}}$), the mean-free-path becomes a function of the nanoparticle size ($\boldsymbol{R_{bulk}} \propto \boldsymbol{R}$). Changing the electrons mean-free-path will affect the damping frequency, $\boldsymbol{\omega_d}$, and consequently $\boldsymbol{\varepsilon'}$. Particularly, when $\boldsymbol{\varepsilon'} = -\boldsymbol{2\varepsilon_m}$ (and $\boldsymbol{\varepsilon''}$ is small enough), Equation 1.1 predicts the existence of an extinction peak, whose position is strongly affected by the particle size (Mulvany, 2001; Baker and Pradhan, 2004). This prediction is experimentally verified and the SPR peak is observed to shift to higher energies as the particle size decreases (Figure 1.3A). However, decreasing the particle size also decreases the absorption intensity, until it is practically unidentifiable for particles of effective diameter less than 2 nm (Alvarez *et al.*, 1997). Additionally, experience has shown that the optical absorption profile depends also very sensitively on the particles shapes (Tan *et al.*, 2004). For instance, while a spherical AuNP presents one SPR peak around 520 nm, elongated nanoparticles (nanorods) exhibit two plasmon resonances: one transverse and the other longitudinal (Figure 1.3B). The transverse plasmon results from the dipole oscillation across the nanorod diameter and is similar to plasmon resonances in spherical gold colloids, showing an extinction peak around 520 nm. The longitudinal plasmon, on its hand, derives from the dipole oscillation along the nanorod length

and results in an extinction peak that is tunable from the visible through the near-infrared by adapting the nanorods aspect ratio (Liao and Hafner, 2005).

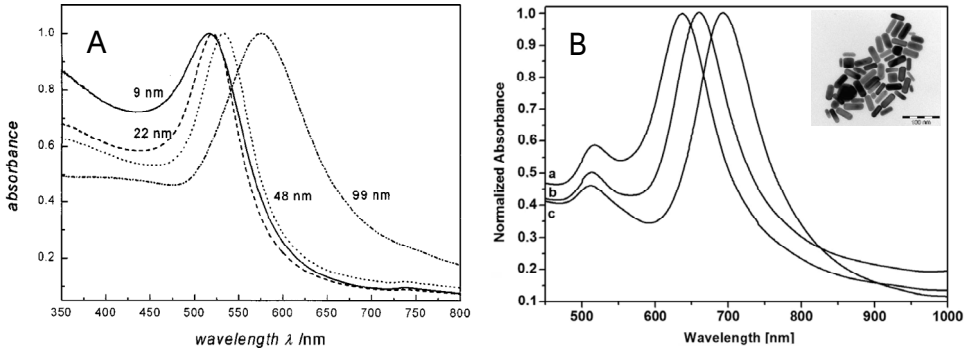


**Figure 1.3** – (A) UV-Vis absorption spectra of 9, 22, 48 and 99 nm diameter AuNPs in water. All spectra are normalized at their absorption maxima, which are 517, 521, 533 and 575 nm, respectively. (B) UV-Vis spectra of gold nanorods with aspect ratios of (a) 1.5, (b) 2.0 and (c) 2.5. (Adapted from: Link and El-Sayed, 1999; Todera *et al.*, 2009)

Equation 1.1, predicts also a variation on the extinction coefficient if there is a change of the dielectric properties of the medium in which the nanoparticles are embedded. Figure 1.4 shows that the SPR peak shifts to higher wavelengths and increases intensity with the increase of the refraction index of the medium (Pérez-Luna *et al.*, 2004).

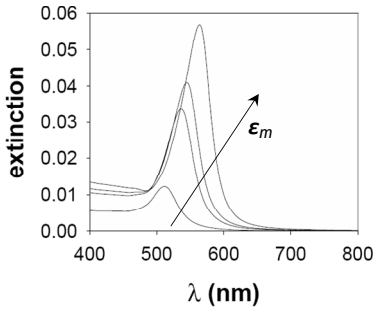


**Figure 1.4** – Simulated optical absorption spectra for 10 nm AuNPs embedded in media with $\varepsilon_m$ = 1.0. 1.77, 2.0 and 2.5. (Adapted from: Pérez-Luna *et al.*, 2004).

Additionally, the optical properties of AuNP solutions depend strongly on the degree of interaction between the individual particles. When the density of nanoparticles is large, each particle will be subject to an average polarization field due to the surrounding particles and, hence, an effective dielectric constant should be considered (Pérez-Luna *et al.*, 2004):

$$\varepsilon_{eff} = \varepsilon_m \frac{1 + \frac{2N\alpha}{3\varepsilon_0\varepsilon_m}}{1 - \frac{N\alpha}{3\varepsilon_0\varepsilon_m}} = \varepsilon_m \frac{1 + 2f\Lambda}{1 - f\Lambda} \qquad \text{Equation 1.5}$$

where $\boldsymbol{N}$ is the number density of nanoparticles, $\boldsymbol{\varepsilon_0}$ is the dielectric constant of vacuum, $\boldsymbol{f} = \boldsymbol{4N/3\pi R^3}$ is the filling factor, $\boldsymbol{\alpha} = \boldsymbol{4\pi\varepsilon_0\varepsilon_m R^3[(\varepsilon - \varepsilon_m)/(\varepsilon + 2\varepsilon_m)]}$ is the polarizability of a small spherical particle in a static electric field and

$$\Lambda = \frac{\varepsilon - \varepsilon_m}{\varepsilon + 2\varepsilon_m} = \frac{\alpha}{3\varepsilon_0\varepsilon_m V} \qquad \text{Equation 1.6}$$

is the Maxwell-Garnet formula. In this context, the extinction cross section is given by:

$$C_{ext} = \frac{4\pi}{\lambda} \sqrt{0.5\left(-\varepsilon_{eff,1} + \sqrt{\varepsilon_{eff,1}^2 + \varepsilon_{eff,2}^2}\right)} \qquad \text{Equation 1.7}$$

Considering even the simplest case of a pair of spherical nanoparticles with small enough center-to-center separation ($\boldsymbol{D}$), the surface plasmon resonances are observed to differ significantly from those of isolated particles due to mutually induced dipoles. The oscillating electrons in one particle feel the electric field due to the oscillations in a second particle, leading to a coupled plasmon oscillation. In this specific case, two oscillation modes exist: one transversal and one longitudinal (relative to the axis of the pair). The absorption peak corresponding to the transversal-mode shifts to only slightly higher wavelengths as the nanoparticles separation decreases, while longitudinal in-phase oscillations are significantly different from non-interacting particles (Mulvany, 2001; Perez-Luna *et al.*, 2004). The average polarizability of the nanoparticles pair is obtained integrating over all possible orientations of the longitudinal and transversal modes, giving:

$$\Lambda_{pair} = \frac{\eta}{2}[(1 - 2\eta(R/D)^3)^{-1} + (1 + \eta(R/D)^3)^{-1}] \qquad \text{Equation 1.8}$$

where $\eta = (\varepsilon_0 - \varepsilon_m)(\varepsilon_0 + 2\varepsilon_m)$. Thus, with the average polarizability, an effective dielectric

constant and the absorption can be calculated using equations 1.6 and 1.7, respectively.

Effectively, theoretical and experimental data show that the shift and magnitude of the absorption peak corresponding to the longitudinal-mode decreases exponentially as the particle-pair center-to-center separation increases, dropping to zero at distances greater than around 2.5 times the nanoparticle size (Figure 1.5, Su *et al.*, 2003; Zhong *et al.*, 2004).

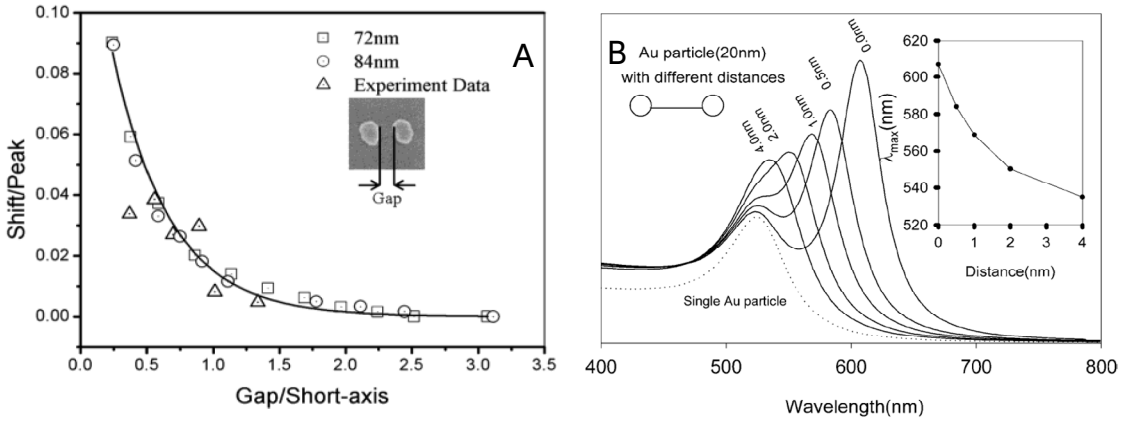


**Figure 1.5** – (A) Comparison of computer-simulated (⊡ = 72 nm nanoparticles, ⊙ = 84 nm nanoparticles) and experimentally measured (△) resonant wavelength shifts as a function of the gap between two particles. The longitudinal-mode absorption peak-shift decays exponentially with increasing particle spacing, and the decay function is size independent because the shift and the gap are scaled by the wavelength peak and particle size, respectively. Computer simulations were performed using the Discrete Dipole Approximation. (B) Electrodynamic calculations of the extinction spectra variation of a pair of 20 nm diameter AuNPs as a function of the interparticle distance. Inset is the peak shift *vs.* interparticle distance. Spectra calculated considering the Generalized Multiparticle Mie (GMM) method (Adapted from: Su *et al.*, 2003; Zhong *et al.*, 2004).

In many-particle aggregates, additional resonances are typically observed to appear at even longer wavelengths that may extend into to the near-infrared region of the optical spectrum, depending on the size of the aggregates and the number of nanoparticles in the aggregate. In fact, the absorption spectra profile in these aggregated nanoparticles systems may depend on many factors, including the aggregate morphology (size and shape) and nanoparticle density. Thus, much more complex calculations are needed to model the extinction properties of multiple nanoparticles aggregates (Perez-Luna *et al.*, 2004; Ghosh and Pal, 2007; Yurkin and Hoekstra, 2007).

## 1.3.2. Synthesis and Functionalization

### 1.3.2.1. Synthesis

Synthesis is a key issue on the development of AuNPs-based biosensing assays, because it defines very important AuNPs properties such as the solubility in water, morphology, size dispersion, and surface functionalities. A "countless" number of methods has been reported on the synthesis of gold nanoparticles (Daniel and Astruc, 2004). Nevertheless, the most commonly used synthesis methods may be divided in two major groups:

(1) the chemical or electrochemical reduction of a gold(III) precursor compound in the presence of a capping agent; or,
(2) the citrate reduction of $HAuCl_4$ in water, first introduced by Turkevich (Turkevich *et al.*, 1951).

The first strategy relies on the ability of the capping agent to bind to the surfaces of the nanoparticles in formation, limiting its growth beyond a chosen range and stabilizing the colloid in the particular solvent used. Additionally, by selecting the adequate experimental conditions (such as: reducing agent, reaction time, temperature and capping agent) the shape and size of the AuNPs can be finely controlled. Given their strong affinity for gold, thiol-based capping agents have been considered of particular interest in the synthesis of gold nanoparticles, resulting in colloidal solutions with narrow size distributions. However, usually, the nanoparticles produced by these methods are soluble only in organic solvents, requiring a further step for solubilization in water. Another downside of this technique is that, most of the times, a cumbersome exchange of the strongly bound capping agents is required, making this type of AuNPs less versatile for biological applications (Baptista *et al.*, 2007).

Due to its simplicity and high yield, spherical gold nanoparticles for biological applications are prepared mainly through some variation of the Turkevich method. One of the great advantages of synthesizing AuNPs through this method relies on the use of citrate as capping agent. In fact, the citrate ions remaining on the AuNPs surfaces after the synthesis procedures not only contribute for the electrostatic stabilization of the nanoparticles in the colloidal solution (overcoming the van der Walls attraction forces) but, also are easily replaced by other capping agents (such as those thiol-based) bearing appropriate functionalities that allow binding almost any biological analyte of interest (Baptista *et al.*, 2007; Tan *et al.*, 2004).

### 1.3.2.2. Functionalization

In most of the cases, the development of AuNP-based biosensors demands a crucial step of labeling their surfaces with specific biomolecular recognition capabilities. Subsequently, depending on the particular characteristics of the biosensing system under study, the AuNPs may or may not need to be previously coated with a layer of ligands possessing particular functionalities.

In practice, in most of the cases, the presence of a ligands layer is desirable for introducing a specific functionality on the AuNPs surfaces. Citrate-coated AuNPs, particularly, have been covered with a large variety of ligand types, following a wide range of strategies. Nevertheless, most of the reported methods follow one of the two main routes depicted in Figure 1.6. In route named R1, the biologically-active functional group is introduced in a single-step reaction. This method requires the use of bifunctional ligands composed by a functional group (X) that binds the ligand to the AuNPs surfaces (such as those thiol-based) and by a second functional group (Z) by which the nanoparticles acquire the desired biological functionality (for instance, carboxylic acid based groups). In the alternative functionalization route (named R2), an "intermediary" bifunctional compound (X-Y) is first reacted with the nanoparticles, where the Y-group acts as a coupling site for the desired functionality (Z) being introduced in a second-step reaction.

Naturally, route R1 is preferred whenever possible since it is a one-step reaction only. However, limitations may occur when, for instance, the Z-group is also prone to react with the gold surfaces, resulting in ineffective functional coatings. In such cases, the route R2 is preferred because it introduces a bifunctional ligand with an intermediate Y-group that avoids non-specific interactions during the coating process and, at the same time, can be further reacted to impart the Z-group functionality in the second-step reaction.

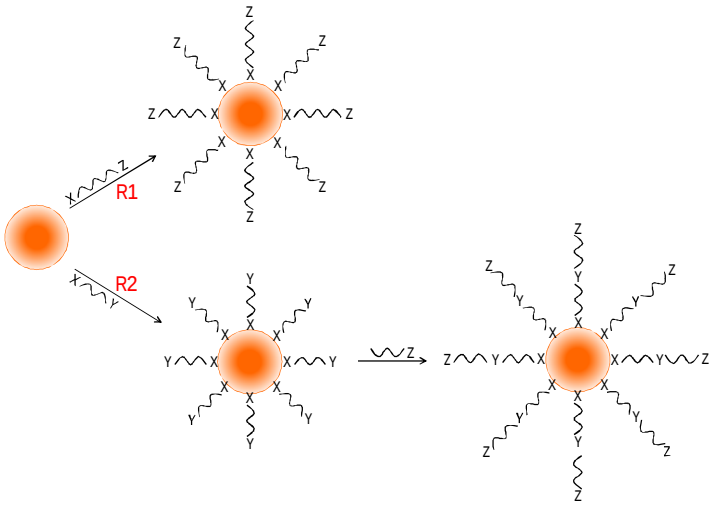


**Figure 1.6 –** Two main routes to attach bio-functional ligands to AuNPs surfaces. **R1**: ligands with the desired Z functionality react directly with the nanoparticles; **R2**: a ligand with a Y functionality reacts directly with the nanoparticles and, in a second step, is converted in the desired functionality Z. Notice that both methods may be applied, in principle, both to citrate-coated AuNPs and to AuNPs synthesized with coating ligands; the difference is that, in the later case, the direct attachment of the "primary" ligands is made through a ligand-exchange-reaction (Adapted from: Neouze and Schubert, 2008).

Figure 1.7 presents, schematically, the four most used strategies to attach biomolecular probes are to AuNPs surfaces:

(A) electrostatic interactions between the negatively charged AuNPs surfaces and positively charged biomolecules;

(B) direct covalent-coupling of biomolecules through thiol groups;

(C) covalent coupling of biomolecules to bifunctional ligands previously immobilized on the AuNPs surfaces; and

(D) specific affinity interactions.

Electrostatic adsorption of positively charged biomolecules can be made either directly on the negatively charged surfaces of citrate coated AuNPs or over a negatively charged layer of anionic ligands (such as the carboxylic acid derivatives) (Figure 1.7A). For instance, AuNPs produced by citrate reduction have been functionalized with immunoglobulin G through electrostatic binding between the positively charged amino acid side chains of the protein and the negatively charged citrate groups of the colloids (Shenton *et al.*, 1999). On the other hand, it has been reported the efficient electrostatic immobilization of recombinant esterases onto carboxylic acid coated AuNPs without eliminating their enzymatic activity. (Ha *et al.*, 2005)

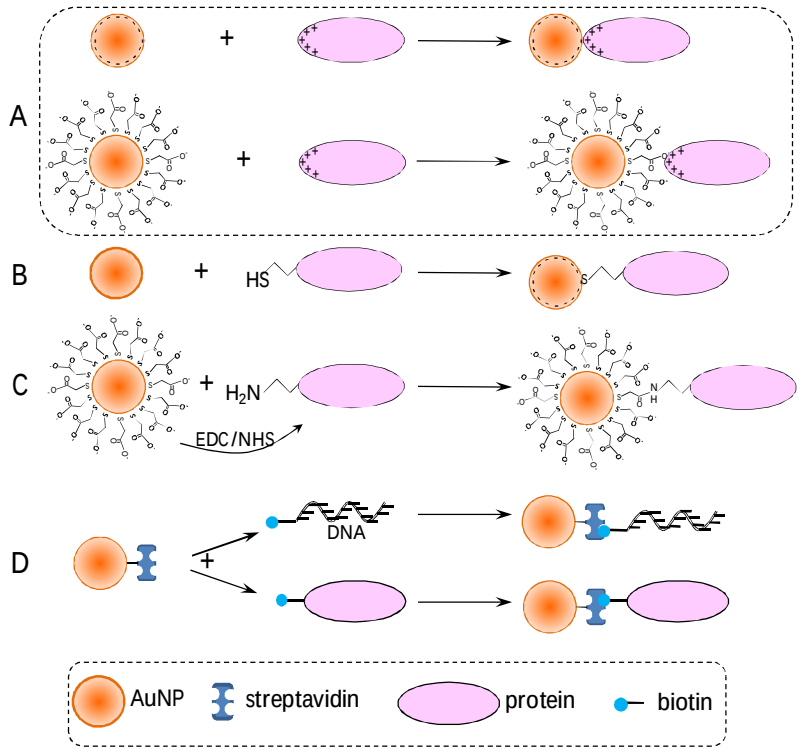


**Figure 1.7** – Main routes for the attachment of biomolecules to AuNPs surfaces. (A) electrostatic interaction between the negatively charged AuNPs surfaces and positively charged domains on the biomolecules; (B) covalent binding between thiol groups present on the biomolecule (innately or modified) and gold surfaces; (C) amide bond formation between carboxyl groups on the AuNPs surfaces and amine groups present on the biomolecule (innately or modified), through EDC/NHS chemistry; (D) affinity interactions between streptavidin labeled AuNPs and biotin-modified biomolecules. (Adapted from: Katz and Willner, 2004)

In another strategy to attach biomolecules to AuNPs, advantage is taken from the thiol groups existing on cysteine/lysine residues of the proteins to directly attach them to the surfaces of citrate coated AuNPs (Figure 1.7B). This method was employed, for instance, to conjugate AuNPs with anti-VEGF proteins (which are known for inducing apoptosis of certain tumor cells; Mukherjee *et al.*, 2007). Additionally, biomolecules without native thiolated residues (proteins, DNA, enzymes, etc.) can be "artificially" modified by chemical means to possess such functionality and, then, attached to the AuNPs using the same strategy. This is a common method to immobilize, for instance, thiol-modified DNA sequences on AuNPs surfaces (Storhoff *et al.*, 2000). Noteworthy, upon direct attachment on nanoparticles surfaces, some proteins and enzymes not only confer higher colloidal stability, but are able also to preserve their native structures and activities.

Alternatively, in order to reduce non-specific adsorption of proteins on gold surfaces, biomolecules can be covalently coupled to AuNPs previously coated with bifunctional ligands (Figure 1.7C). A common example is the attachment of biomolecules to AuNPs covered with a layer of carboxylic acid based ligand through the very well known EDC/NHS (1-Ethyl-3-[3-

dimethylaminopropyl]carbodiimide hydrochloride / N-hydroxysulfosuccinimide ) chemistry. EDC converts the carboxylic acids into amine-reactive *O*-acylisourea intermediates which, on their turn, are converted into more stable amine-reactive sulfo-NHS esters by the NHS reagent. The modified nanoparticles can thus be covalently coupled to biomolecules of interest possessing primary amino functional groups by the formation of amide bonds. As an example, AuNPs have been functionalized with the glucose oxidase enzyme which demonstrated great activity even under typically harsh conditions (Li *et al.*, 2007). As before, biomolecules not possessing the amine functionality may chemically reacted to have it and also attached to the carboxyl ligands on the gold surfaces.

Finally, AuNPs may also be functionalized with groups that provide affinity sites for the specific binding of biomolecules such as proteins and oligonucleotides (Figure 1.7D). For example, streptavidin-coated AuNPs have been used for the affinity binding of biotinylated immunoglobulins, serum albumins and oligonucleotides (Gestwicki *et al.*, 2000; Niemeyer, 2001).

### 1.3.3. Biosensing

As discussed in the section 1.3.1, the exact position and magnitude of the absorption peak(s) of a colloidal solution of AuNPs depends strongly on the nanoparticles morphology, on the dielectric constant of medium in which the nanoparticles are embedded and on the degree of interaction between nanoparticles (Storhoff *et al.*, 2000; Su *et al.*, 2003). In particular, the later parameter has been increasingly exploited over the last years as transduction signal in a variety of biosensing platforms, where the controlled biorecognition-induced aggregation (or disaggregation) of AuNPs produces predictable colorimetric variations through interparticle plasmon coupling (Figure 1.8) (Ghosh and Pal, 2007; Daniel and Astruc, 2004). To date, a large variety of targets have been detected using this colorimetric method, including nucleic acids (Storhoff *et al.*, 2000; Li and Rotheberg, 2004), proteins (Hazarika *et al.*, 2006; Thanh and Rosenzweig, 2002), saccharides (Schofield *et al.*, 2007), metal ions (Kim *et al.*, 2001) and cells (Medley *et al.*, 2008), in applications that range from clinical diagnostics (Nath *et al.*, 2008), to drug discovery (Dobrovolskaia *et al.*, 2009) and to environmental contaminant analysis (Darbha *et al.*,2008).

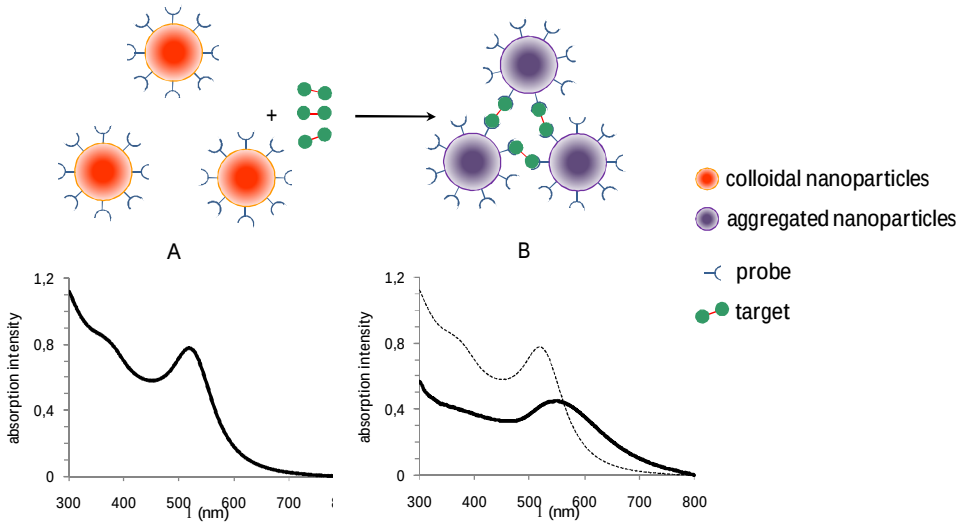


**Figure 1.8** – Schematic example of biorecognition-induced aggregation of AuNPs. (A) Colloidal solution of probe-functionalized AuNPs and its typical optical absorption spectrum. (B) The biorecognition-induced aggregation of the functionalized AuNPs by means of interaction with the target analyte results in a plasmon peak shift towards higher wavelength as well as in broadening of the spectrum, which can be detected with the naked eye by a color change from red-to-blue of the colloidal solution.

Typically, the surface plasmon resonances of colloidal solutions of AuNPs generate strong absorptions at the 520 nm band (corresponding to green light) causing their well known reddish color. Given that the interparticle coupling at close distances generates absorption band shifts towards higher wavelengths, a color change from red to blue may be readily observed by the naked eye (Figure 1.9A), thus avoiding the need of expensive/sophisticated instruments for a qualitative analysis. On the other hand, extinction data recorded using a spectrophotometer may provide high-sensitivity quantitative-analysis of the degree of aggregation of AuNPs. To that end, three quantitative parameters may be considered: (1) the shift of the SPR peak position, $\Delta\lambda$, (and/or the appearance/disappearance of additional peaks); (2) the variation of the absorption intensity, $\Delta abs$; and (3) the variation of the *flocculation parameter* (Figure 1.9 B and C, description below).

Specifically, upon aggregation, the SPR peak occurring around 520 nm for the un-aggregated system is expected to shift towards higher wavelengths due to the coupling of the individual resonances of the particles composing each aggregate (Figure 1.9B). This effect may be also regarded in terms of absorption intensity variation which, in an aggregating system, is expected to decrease in the band around 520 nm and to increase at a higher wavelength band (typically above 600 nm). The flocculation parameter is defined semi-empirically as the integrated absorbance between 600 and 800 nm of the optical absorption spectrum normalized to

the absorption intensity at the SPR peak (Weisbecker *et al.*, 1996) and may be regarded as containing the joint information of the other two parameters. Consequently, the flocculation parameter is closely related to the extent of aggregation of AuNPs samples, such that it increases with increasing degree of aggregation as a result of the absorbance shift to longer wavelengths (Figure 1.9C).

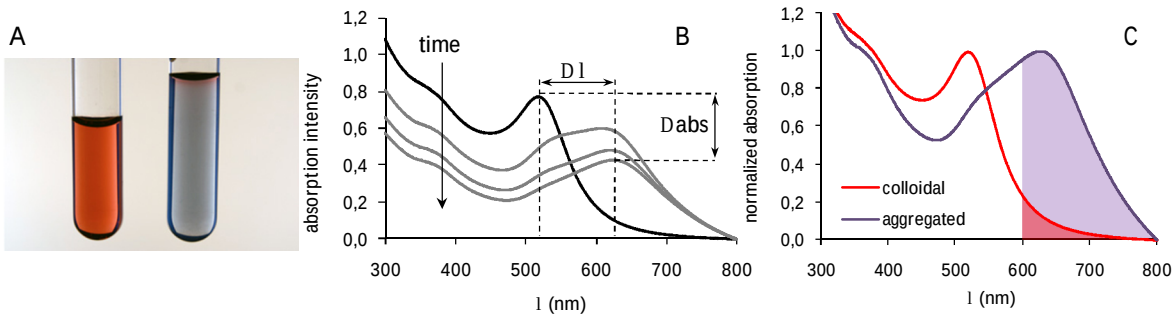


**Figure 1.9** – (A) left vial: colloidal solution of AuNPs; right-vial: solution of aggregated AuNPs; (B) Optical absorption spectrum evolution along time of an example of an aggregating system consisting of a solution of ~10 nm AuNPs to which NaCl was mixed ($[NaCl]_f$ = 150 mM); (C) spectra of colloidal (red) and aggregated (purple) AuNPs normalized to the intensity at the absorption peak. Each of the shaded areas corresponds to the flocculation parameter value at each aggregation status.

Thus, the key to colorimetric biosensing using the distinguished optical properties of AuNPs is the control of the degree of dispersion/aggregation of the colloidal solutions with a biological process (or analyte) of interest. From a general standpoint, in biosensing assays, there are two main routes by which the controlled aggregation of colloidal AuNPs has been promoted:

(1) interparticle bonding formation (interparticle crosslinking aggregation mechanism); or
(2) removal of the colloidal stabilization effects (*non-crosslinking aggregation mechanism*).

### 1.3.3.1. Crosslinking-based biosensing

The interparticle crosslinking aggregation based assays seem to be, so far, the most common approach through which AuNPs are brought into close proximity. In this context, the aggregation may be induced either by (1) target molecules possessing multiple binding sites for the receptor molecules previously attached to the nanoparticles surfaces; or (2) by the direct interaction between receptor-modified nanoparticles and *anti-receptor*-modified nanoparticles. In either case, the interparticle bond formation through biological recognition is strong enough to overcome the interparticle repulsive forces (electrostatic and/or steric), leading to aggregation

and thus to spectral changes.

Several strategies have been designed for the detection of target analytes bearing multiple binding sites that act as crosslinkers of receptors attached on the nanoparticles surfaces (Figure 1.10, pag. 40, top scheme). Such strategies include the use of DNA hybridization, aptamer-target interactions, antibody-antigen interactions, streptavidin-biotin interactions, lectin-sugar interactions or metal-ligand coordination to induce the aggregation of the colloidal solutions (or the redispersion of aggregated colloids), thus promoting a detectable colorimetric variation that translated detection.

Pathway-A in Figure 1.10 represents a biosensing strategy where probe-functionalized AuNPs are induced to aggregate upon mixing with specific targets that possess multiple binding sites for the probes. The biosensing transducing signal is a red-to-blue color change of the samples, associated with a shift of the SPR peak to higher wavelengths. In this context, for instance, Storhoff and coworkers developed a DNA biosensing strategy (Storhoff ***et al.***, 2000). The presence of the complemetary target-DNA strands in solution was detected by a SPR peak shift to higher wavelengths as probe-functionalized AuNPs aggregated owing to hybridization-induced crosslinking. Using the well known oligonucleotide length as ruler, this strategy was further used to demonstrate that the SPR peak position is highly dependent on the on the interparticle distance, with SPR coupling decreasing significantly with increasing distance. Potential applications of this strategy in the detection of ligands-to-proteins binding events have also been explored. For instance, the aggregation of biotin-modified AuNPs was induced by the presence of streptavidin in solution, which upon binding to biotin molecules generated crosslinking between the AuNPs (Caswell ***et al.***, 2003).

The possibility of reversing the AuNPs aggregation elicits the use of crosslinked aggregates on the detection of analytes (or biological processes) that act over the crosslinker molecules in such a way that crosslinking mechanism is eliminated. In this case, the biorecognition signal is transduced by a SPR peak shift to lower wavelengths due to the redispersion of the AuNPs (Figure 1.10, pathway B). Liu and Lu, for instance, developed assays where AuNPs previously aggregated through crosslinking of specially designed DNA sequences, were used to detect analytes that induce AuNPs disaggregation by disrupting the DNA crosslinking effect (Figure 1.11; Liu and Lu, 2005; Liu and Lu, 2006). Another strategy consists in inducing AuNPs disaggregation through competitive binding of the target analytes on biorecognition sites of molecules involved in the crosslinking of the AuNPs (Figure 1.12; Aslan ***et al.***, 2004).

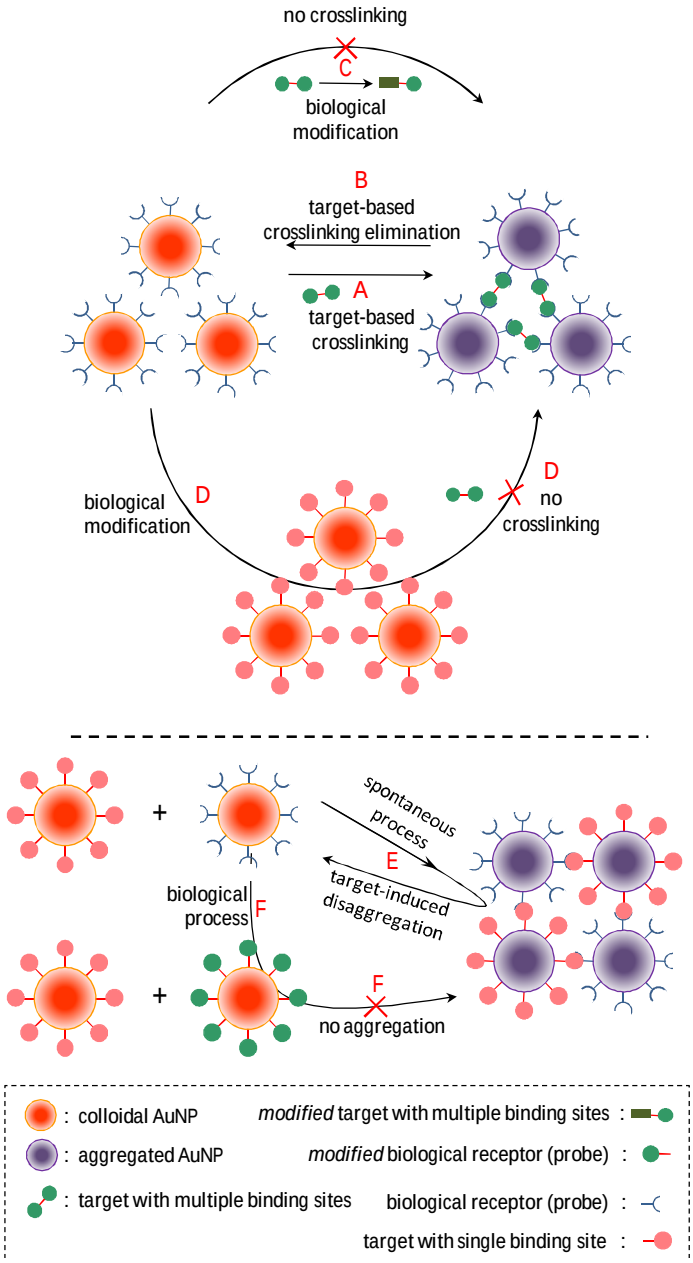


**Figure 1.10** – *Top scheme*: AuNPs aggregation through interparticle crosslinking: A) AuNPs are brought close together by target molecules having multiple binding sites for the corresponding receptors previously attached on nanoparticles surfaces; B) biological recognition events (or processes) that remove (or break) crosslinking molecules, causing redispersion of the nanoparticles; C) biological recognition events (or processes) that can modify crosslinking molecules, avoiding aggregation, and D) biological recognition events (or processes) that can modify the receptors on the nanoparticles surfaces, can indirectly control aggregation and redispersion. *Bottom scheme*: AuNPs aggregation induced by direct recognition (without crosslinkers) of receptor-modified nanoparticles and complementary-modified nanoparticles: E) biological recognition events (or processes) that break these interparticle interactions result redispersion of the nanoparticles; F) aggregation can be regulated by biological processes that modify surface-attached receptors (equivalent to pathway D in the top scheme). (Adapted from: Zhao *et al.*, 2008).

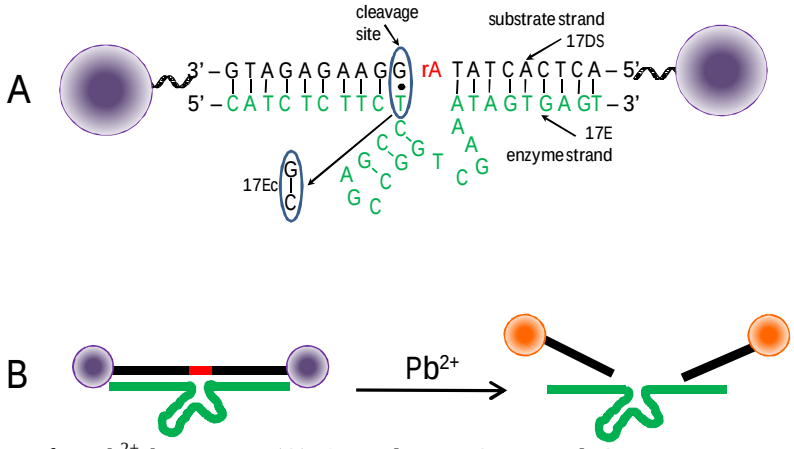


**Figure 1.11** – Scheme of a $Pb^{2+}$ biosensor. (A) Special ssDNA-covered AuNPs are aggregated by means of crosslinking with a specific DNA-enzyme (17E). In the presence of $Pb^{2+}$, the enzyme cleaves the substrate (17DS) at the RNA (rA) linkage, leading to redispersion of the aggregated AuNPs. (Adapted from: Liu and Lu, 2005 ).

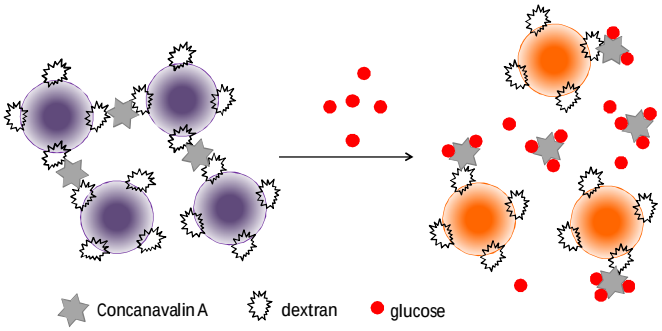


**Figure 1.12** – Glucose sensing mechanism. Dextran-coated AuNPs are induced to aggregate through crosslinking with concanavalin-A. When mixed in solution, glucose competitively binds to concanavalin-A resulting in the redispersion of the AuNPs (Adapted from: Aslan *et al.*, 2004).

The two sensing strategies described above rely on SPR peak shifts, originated either by aggregation or by disaggregation of AuNPs, to detect analytes (or biological processes) of interest. Alternatively, strategies have been designed where the non-shift of the SPR peak is itself the biorecognition signal (Figure 1.10, pathways C and D). Such is the case when target analytes (or biological processes) modify molecules that otherwise would be involved in crosslinking the AuNPs. These strategies have been applied to detect, for instance, enzymatic activity (Guarise *et al.*, 2006; Wang *et al.*, 2006). Guarise and coworkers detected the presence of a protease in solution due to its activity in cleaving specific cysteine-terminated peptide sequences that otherwise would crosslink AuNPs. Thus the SPR peak shift to higher wavelengths was prevented due to the modification imparted on the "probe-crosslinker" molecules by the target molecules (Figure 1.13). A similar approach was followed by Wang, who were able to detect the presence of kinase-inhibitors in solution, relying on their effect in preventing modification of probes immobilized on AuNPs surfaces which otherwise would induce aggregation.

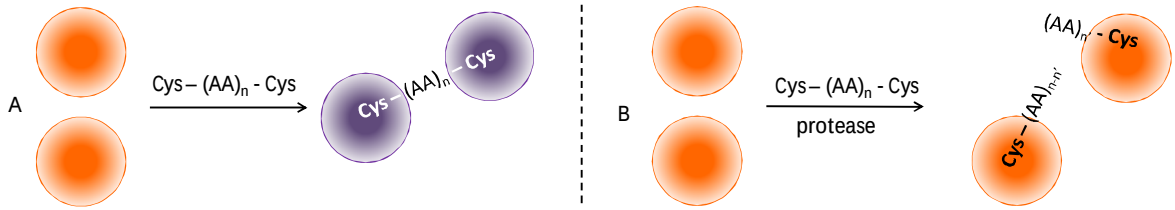


**Figure 1.13** – (A) bare AuNPs are induced to aggregate through crosslinking with cysteine-terminated peptides. (B) the specific protease (target) cleaves the crosslinking peptide in two, eliminating the aggregation mechanism.

Aggregation of AuNPs can be also induced without the presence of free crosslinker molecules in solution (Figure 1.10, bottom scheme). For instance, when receptor-modified AuNPs are mixed with *anti-receptor*-modified AuNPs, aggregation spontaneously follows through biorecognition and the characteristic SPR peak shift to higher wavelengths is observed. These aggregated AuNPs systems may then be used to detect targets that induce their disaggregation by breaking the receptor/anti-receptor linkage, which leads to an SPR peak shift to lower wavelengths (Figure 1.10, pathway E). Such strategy has been used, for instance by Xu and coworkers, to detect the activity of endonucleases as well as the presence of their inhibitors in solution (Xu *et al.*, 2007). The method relied in systems of AuNPs aggregated by means of the hybridization of specially designed DNA sequences (Figure 1.14). It was observed that by mixing a specific endonuclease to the aggregated solution lead to a SPR peak shift to lower wavelengths due enzymatic-induced cleavage of the DNA strands. However, the presence of a specific endonuclease inhibitor in the aggregated solution prior to the introduction of the endonuclease, prevented the enzymatic cleavage mechanism and thus the SPR peak shift to lower wavelengths.

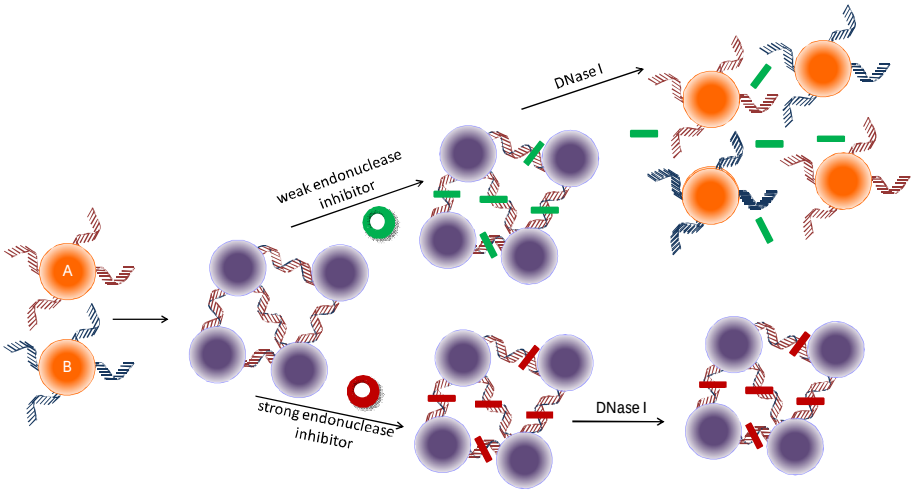


**Figure 1.14** – Illustration of the application of DNA-aggregated AuNP probes for colorimetric screening of endonuclease inhibitors. (Adapted from: Xu et al., 2007)

The biosensing strategy represented by pathway-F in Figure 1.10 is somewhat similar to that represented by pathway-D. The difference is that in the former case there are no free crosslinkers in solution. In this context, a strategy has been reported to detect pH variations relying in a special oligonucleotide single-stranded sequence that shows highly pH-dependent tridimensional configurations (Sharma *et al.*, 2007). In acid environments, the special DNA sequences (attached to AuNPs) fold in such a way that hybridization with the complementary strands immobilized on the surfaces of other AuNPs is inhibited, thus preventing aggregation (Figure 1.15). On the other hand, in basic solutions, the special DNA sequence unfolds, enabling hybridization and crosslinking AuNPs which leads to as SPR peak shift to higher wavelengths.

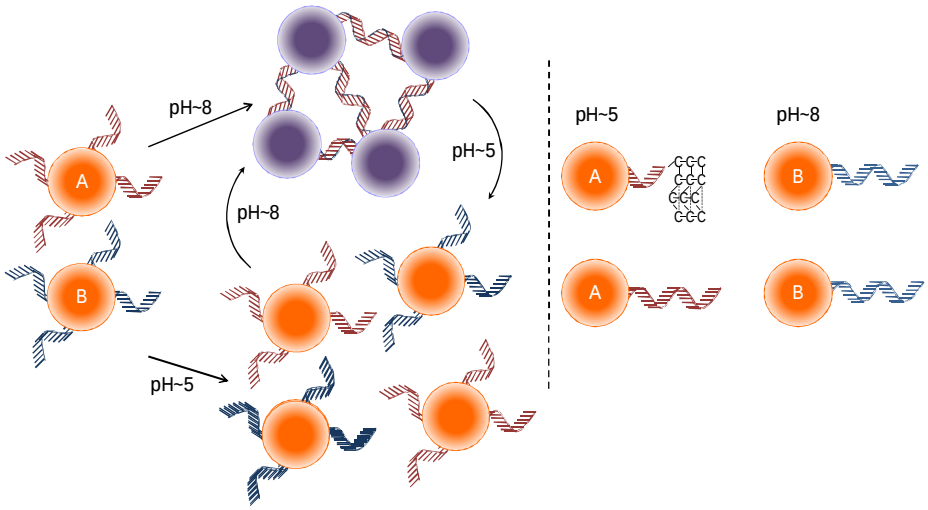


**Figure 1.15** – Schematic illustration of the working cycle and color change of the special ssDNA-functionalized AuNP under acid and basic pH. (Adapted from: Sharma *et al.*, 2007)

### 1.3.3.2. Non-Crosslinking-based biosensing

"Non-crosslinking aggregation" or "destabilization-induced aggregation" mechanisms may also be used as alternatives to control AuNPs aggregation in colorimetric-based biosensing assays. Herein, the induced loss of electrostatic, steric or electrosteric stabilizations of the AuNPs colloids results in a domination of the Van der Walls attractive forces between nanoparticles, which leads to aggregation without the need of formation of interparticle bonds. Specifically, depending on the capping agents coating the surfaces of colloidal AuNPs, the colloidal stability may be significantly reduced by 3 main routes:

(1) induced loss of electrostatic stabilization;

(2) induced loss of (electro)steric stabilization and;

(3) induced loss of colloidal stability upon (charged) polymer conformational transitions.

It is very well know fact that electrostatically-stabilized citrate-coated AuNPs tend to aggregate under the effect of the Van der Walls forces when exposed to certain levels of a salt, which occurs because the salt tends to screen the electrostatic repulsion forces that keep the AuNPs dispersed in solution. For instance, Li and Rothberg reported a strategy where the particular electrostatic properties of ssDNA, dsDNA and citrate-coated AuNPs were used to detect DNA hybridization (Li and Rothberg, 2004). The researchers observed that, while the presence of ssDNA in solution resulted in enhanced colloidal stability of AuNPs against salt induced aggregation, the presence of DNA double-strands had little or no effect over the colloidal stability. Thus, exposing AuNPs solutions containing either ssDNA or dsDNA to the identical levels of salt, produced different SPR variations which allowed differentiating between hybridized and non-hybridized DNA (Figure 1.16).

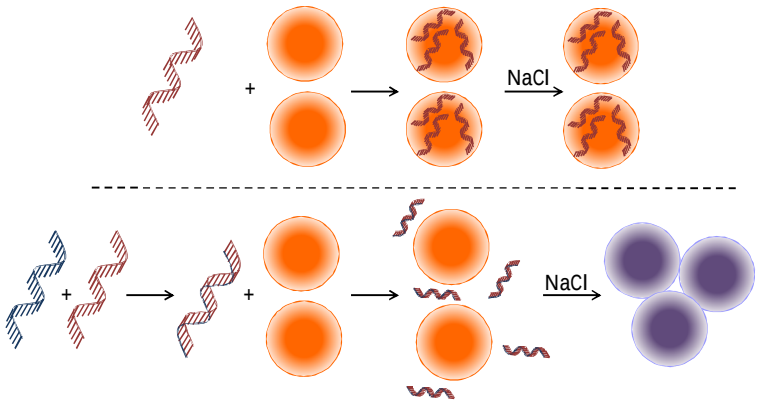


**Figure 1.16** – Representation of the colorimetric method for differentiating between single- and double-stranded oligonucleotides. (Adapted from: Li and Rothberg, 2004).

Zhao and colleagues, on the other hand, took advantage of the (electro)steric stabilization effect conferred by thiol-terminated dsDNA bound to AuNPs surfaces to detect the activity of a DNase (Zhao *et al.*, 2008). Since the dsDNA is cleaved by the DNase, the activity of the later may be detected by an SPR peak shift to higher wavelengths when the colloidal solution to which the DNase was mixed is challenged with certain amounts of salt (Figure 1.17).

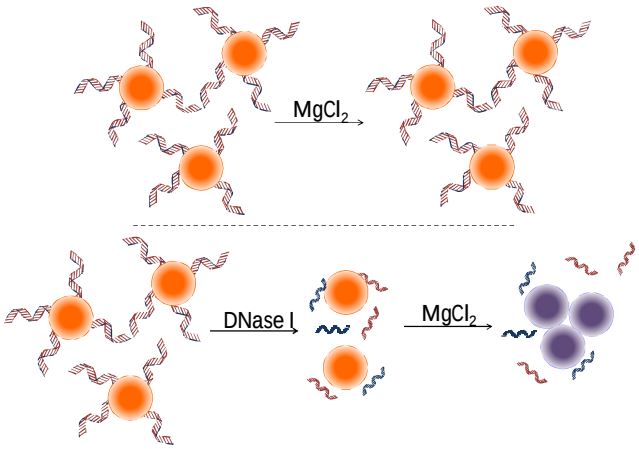


**Figure 1.17** – Schematic illustration of AuNP aggregation and color change triggered by the enzymatic cleavage of DNA on AuNPs. Before enzymatic cleavage, DNA-modified AuNPs are stable at a relatively high salt concentration owing to the electrostatic and steric stabilization. The removal of DNA (colloidal stabilizer) on the AuNP surface by enzymatic cleavage destabilizes the AuNP and results in a rapid aggregation. (Adapted from: Zhao *et al.*, 2008)

In the context of induced loss of colloidal stability upon (charged) polymer conformational transitions, Sato and coworkers published an alternative DNA biosensing strategy that allows differentiating between target DNA that is fully complementary to probe DNA immobilized on the AuNPs surfaces and target DNA possessing a single base mismatch at the 5' terminus (Sato *et al.*, 2003). Researchers observed that, while AuNPs with fully complementary dsDNA immobilized on their surfaces (through thiol bonds) aggregate under the influence of certain amounts of salt, on the other hand, AuNPs covered with dsDNA possessing a single-base mismatch at the 5´terminus did not aggregated under similar conditions. Thus, in the former case a SPR peak shift to higher wavelengths was observed, while in the later case the colloidal solutions remained stable and no color change was observed.

*In summary*, a wide variety of biosensing strategies have been developed that take advantage of the unique optical properties of colloidal solutions of gold nanoparticles. Particularly, many bioassays have been reported based on the high sensitivity of the SPR band to the distance between AuNPs, which allows obtaining colorimetric transducing signals of biorecognition events. From the analysis of many biosensing reports in which the detection of targets or biological processes are transduced via optoelectronic-based colorimetric changes of AuNPs, one may withdraw two important conclusions: (1) the particular properties of the colloidal solutions of gold nanoparticles allow them to be used in a wide range of biosensing applications, and (2) for each particular application, sets of parameters (that may include the nanoparticles size, the nanoparticles coatings, the buffer conditions, etc.) need to be finely

adjusted to meet the biochemical characteristics of the biological system under study.

Target-analytes possessing multiple binding sites for a specific probe offer a great advantage on the design of biosensing assays because, upon biorecognition, they act as crosslinkers between probe-modified nanoparticles inducing aggregation and, thus, the observation of a measurable colorimetric signal. Additionally, biosensing strategies through crosslinking-induced aggregation may also be designed towards the detection of targets possessing only one binding site for the probe. However, in this case, the biosensing design involves always the modification of at least two different complementary-modified AuNP batches which aggregate upon mixing, resulting in a red-to-blue color change signal that transduces biorecognition.

Alternatively, biosensing strategies may be designed that do not rely in crosslinking mechanisms. Instead, these approaches depend on the ability to control the mechanisms that rule the equilibrium between the repulsive and the attractive forces governing the AuNPs colloidal stability. Particularly, strategies have been developed where the analyte (or biological process) of interest allow to controllably decrease or eliminate the repulsive forces (electrostatic, steric or electrosteric) that attribute AuNPs their colloidal stability, leading to aggregation by means of the attractive van der Walls forces.

Comparing the two main routes by which colloidal solutions of AuNPs have been induced to aggregate in biosensing, the later route (non-crosslinking-based) presents a couple of advantages over the former (crosslinking-based), namely: (1) neither interparticle biorecognition nor a target analyte/receptor bearing multiple binding sites are required, and (2) the aggregation process is much more rapid, typically taking up to a few minutes (Zhao *et al.*, 2008).

## 1.4. Semiconductor Quantum Dots

Quantum dots (also known as nanocrystals, or nanocrystallites) are viewed as promising candidates in several research fields from optoelectronics (Zrenner *et al.*, 2008; Bhattacharya *et al.*, 2007) to energy (Robel *et al.*, 2006; Liu *et al.*, 2004), to environment (Wang, *et al.*, 2002) and healthcare (diagnostics, therapeutics, drug discovery). Quantum dots are nearly spherical, luminescent nanosized crystals made of semiconductor materials from the periodic groups of II-VI, III-V, or IV-VI, with size ranging from 1 to 12 nm and comprising up to 10000 atoms (Costa-Fernández *et al.*, 2006; Smith *et al.*, 2006). Research using this materials effectively took-off with the realization that the optical and electronic properties of quantum dots may be finely tuned by the adjustment of their physical size.

### 1.4.1. Fundamental Principles and Definitions

In a bulk semiconductor material, electrons may be found having a range of energies. Electrons with different energies are said to be in different energy levels and, it has been established that, each energy level can "accommodate" only up to two electrons (the Pauli Exclusion Principle). In bulk materials, the separation between the energy levels available to the electrons is so small that the levels are described as continuous (Figure 1.18a). Bulk semiconductors are distinguished from other types of bulk materials because, in their continuous structure of energy levels, there is an interval that is quantum mechanically forbidden to the electrons. This forbidden region is known as the band-gap and its wideness depends on the chemical composition of the semiconductor. Electrons occupying energy levels above or below that band-gap are described as being negative charge-carriers in the conduction or valence band, respectively.

In bulk semiconductor materials, only an extremely small percentage of electrons occupy energy levels in the conduction band; the overwhelming majority of electrons are found in the valence band, occupying almost all of its available energy levels. An electron belonging to the valence band may receive an amount of energy (in the form of either heat, voltage or electromagnetic) such that its new energy level falls within the conduction band. For this to occur (a process commonly known as the *electron excitation across the energy band-gap*), an energy minimum is required that corresponds to the energy of the band-gap (Figure 1.18b). The energy level left unoccupied on the valence band, as a consequence of the excitation of the electron across the band-gap, is commonly referred to as a hole or positive charge-carrier (Figure 1.18c).

However, the ***exciton***, defined as the pair formed by the electron excited to the conduction band and the corresponding hole on the valence band, does not exist for long. In a first stage, the exciton quickly minimizes its energy by reducing the energy of the excited electron to the lowest available energy level on the conduction band (Figure 1.18d). Then, the electron loses the rest of its excitation energy all at once and returns to its previous energy level within the valence band, emitting electromagnetic radiation (a photon) with a wavelength that corresponds to the energy of the band-gap (Figure 1.18e) (Costa-Fernández *et al.* 2006). This process is often referred to as *electron-hole recombination*, *exciton decay* or *exciton relaxation*. Also, the emitted radiation is called *band-edge emission* when recombination occurs from the lowest possible energy level in the conduction band.

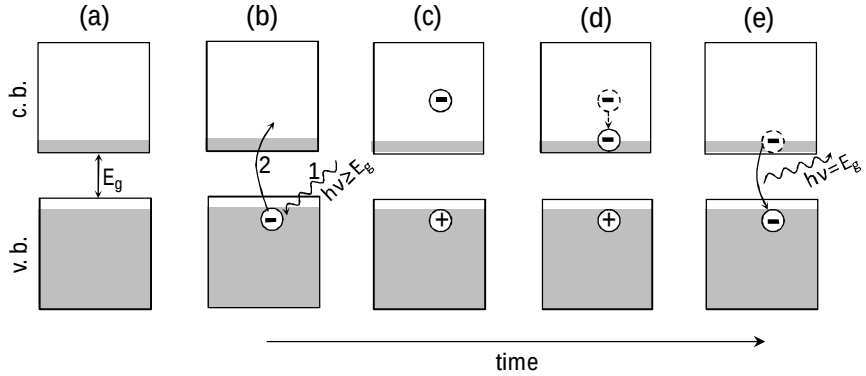


**Figure 1.18** – Schematics of the continuous energy levels structure in bulk semiconductor materials. Shaded areas represent the energy levels occupied by electrons and the white areas represent the energy levels available to the electrons in the semiconductor material. c.b. = conduction band; v.b. = valence band. Refer to the text for the detailed description.

Quantum dots are also made out of semiconductor materials and, the concepts of energy

levels, band-gap, conduction band and valence band described above still apply. However, their reduced size results in one major difference that has great impact on the absorptive and emissive profile of the semiconductor. The explanation follows.

In an exciton, the electron and hole are separated by an average distance called the ***Exciton Bohr Radius*** (EBR), which is different for each type of semiconductor material. In bulk materials, the dimensions of the semiconductor crystal are much larger than the EBR, allowing the exciton to extend to its natural limit (which is on the order of a few nanometers). However, when the size of a semiconductor crystal becomes small enough that it approaches the size of the material's EBR, the continuity of the energy levels is broken in to discrete energy levels (Figure 1.19). Hence, the discretization of the energy levels (arising from the "shrinkage" of the semiconductor material) is said to result from *Quantum Confinement*, and the particles with sizes small enough to produce it are called ***Quantum Dots***.

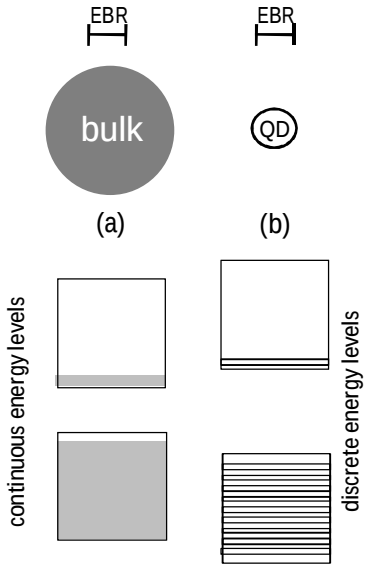


**Figure 1.19** – Schematics comparing the structure of the energy levels in (a) bulk semiconductor materials and (b) in quantum dots. EBR = Exciton Bohr Radius.

Since the quantum confinement arises as a *size-dependent* effect that results in the discretization of the energy levels of the semiconductor material, the addition or subtraction of even just a few atoms to a semiconductor nanocrystal, may produce profound effects on the structure of that energy levels. As the size of quantum dots is decreased, the quantum confinement is increased, resulting in the increase of the spacing between energy levels and in the enlargement of the band-gap wideness. Hence, since (a) the exciton recombination in quantum dots is observed to occur mostly through band-edge emission and (b) the wideness of

the energy band-gap depends on the quantum dot size, then, it is possible to tune with extreme precision the wavelength of the band-edge emission of quantum dots by fine control of their size.

The size-dependence of the band-edge emission wavelength has been extensively studied but, in practice, the overall fluorescence process in quantum dots is quite complex. In many cases, the photoluminescence spectra of quantum dots exhibit a broad and low intensity luminescence band at wavelengths above the band-edge emission, which arise due to the emission from *deep-traps* (Chen *et al.*, 2004). Deep-traps are electronic energy levels that exist within the band-gap of the quantum dot (Figure 1.20). They are originated either by defects in the crystalline lattice of the semiconductor material or by a poorly passivated surface that alters the structure of the energy levels of the atoms closest to the quantum dot surface. The so called *deep-trap emission* occurs when excited electrons "fall" in to one of such deep-traps and, from there, recombine with the hole, resulting in the emission of a higher wavelength (lower energy) photon.

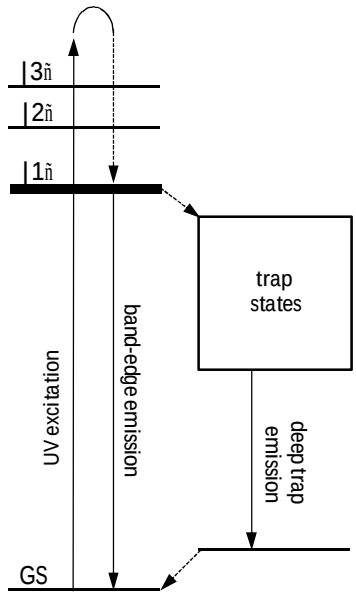


**Figure 1.20** - Representation of theoretically predicted electronic structure of CdSe/ZnS core/shell quantum dots, and proposed exciton recombination routes. (Adapted from: Jones *et al.*, 2003).

Deep-traps contribute to the decrease of the quantum dots photoluminescence efficiency, not only through deep-trap emission, but also because they open way to non-radiative recombination mechanisms. Most of the times, researchers are interested in obtaining from quantum dots the highest possible photoluminescence efficiency at the wavelength corresponding to band-edge emission. Naturally, to achieve this, all the other possible

recombination pathways must be reduced to a minimum. In that context, efforts have been made to understand and overcome the causes of the deep-trap emission. Those efforts converge from two main branches: on one hand, by improving the methods of synthesis, researchers are being able to reduce to a minimum the number of lattice defects in semiconductor nanocrystals; on the other hand, better passivation strategies are being developed that allow reducing to a minimum the energetic levels originating by interfacial phenomena (for instance, capping the nanocrystal with a shell of a wider-band semiconductor) (Chen *et al.*, 2004; Driggers, 2003; Dabbousi *et al.*, 1997).

### 1.4.2. Properties of Quantum Dots

Perhaps the most distinguished property of quantum dots is the ability to finely tune their photoluminescence profile by a "simple" adjustment of the nanoparticles size. Nevertheless, the range of wavelengths in which a certain type of quantum dots can be tuned to emit, just by varying their size, depends on the type of semiconductor material(s) of which they are made. In fact, by tuning the size and chemical composition, quantum dots can be tuned to emit in the range between 400 and 4000 nm (Figure 1.21, Bailey *et al.*, 2004; Smith *et al.*, 2006). Thus, a researcher can choose the emission wavelength that is adequate to a particular experiment and, then, synthesize the quantum dot based probe by using the appropriate semiconductor material(s) and nanocrystal size.

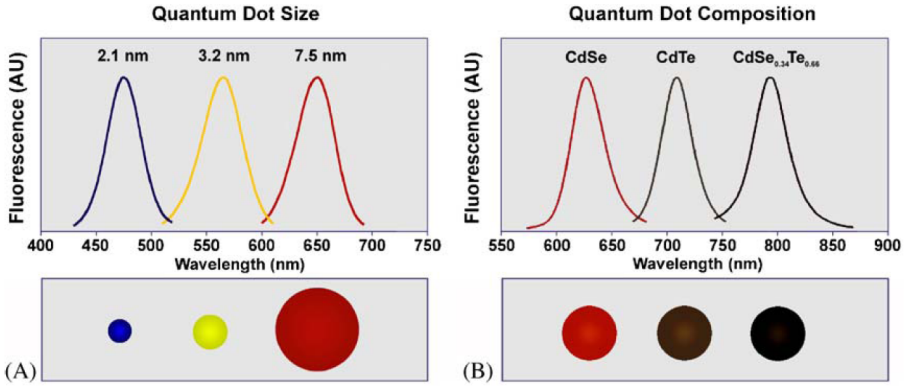


**Figure 1.21** – The emission wavelength of quantum dots is tuned by changing the nanoparticle size and/or its composition. (A) The emission wavelength of CdSe quantum dots may be adjusted within the range from 450 to 650 nm by selecting the nanoparticle diameters between 2 and 7.5 nm. (B) While keeping the nanoparticle size constant (5 nm in diameter) and varying the composition of the ternary alloy CdSexTe1-x, the emission maximum may be tuned to any wavelength between 610 and 800 nm. (Image originally published in: Bailey *et al.*, 2004).

Control over the mean nanocrystal size and nanocrystal size distribution, allows obtaining

quantum dots solutions with narrow and symmetric emission peaks, and full-widths-at-half-maximum (FWHM) typically on the order of 25 to 35 nm [although bandwidths as narrow as 12.7 nm have also been reported (Reiss *et al.*, 2004)]. This is much better than the emission characteristics of typical organic dyes, which often have much broader and asymmetric emission profiles (Figure 1.22). This property is particularly useful when simultaneous labeling and detection of multiple analytes is desired.

The absorption spectrum of quantum dots is a series of overlapping peaks that get larger at shorter wavelengths, each peak corresponding to an energy transition between discrete energy levels (Figure 1.22). Quantum dots do not absorb light with energy below that of the first exciton peak, whose wavelength is a function of the composition and size of the quantum dots (just like all the other optical and electronic properties). Typical organic dyes, on the other hand, present large absorption intensities but only in narrow bands of the optical absorption spectrum. Thus, quantum dots show advantageous absorption properties in comparison with typical organic dyes allowing, for instance, efficient simultaneous excitation of quantum dots emitting at different wavelengths with a single wavelength light source.

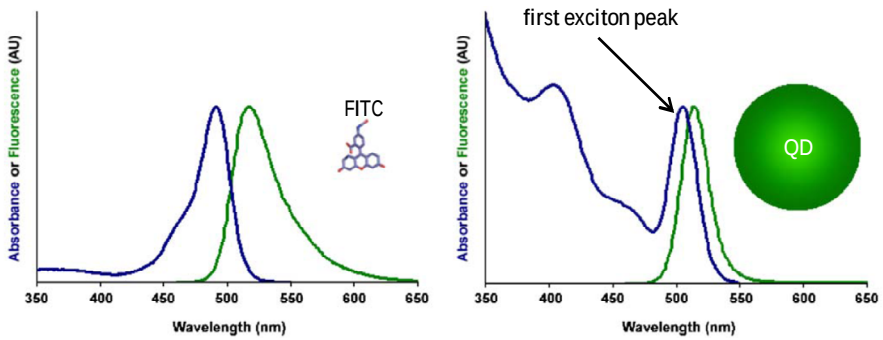


**Figure 1.22** – Comparison between the absorbance and emission profiles of a quantum dot and FITC (an organic dye). (Adapted from: Bailey *et al.*, 2004).

By comparing the absorption and emission profiles of quantum dots and typical organic fluorophores, another advantage arises favoring the quantum dots. Since: (a) a single wavelength light-source can be used to excite simultaneously different quantum dots emitting at different wavelengths, (b) the wavelength of that excitation light can be chosen "far away" from the emission peaks of the different quantum dots (i.e, with a large Stokes-shift) and (c) the emission profile of the quantum dots is typically narrow, then, multiplexing applications can be performed with a larger number of colors because the crosstalking between the detected signals can be greatly reduced (Han *et al.*, 2001).

The quantum yield of a fluorescent material is defined, basically, as the ratio between the number of photons absorbed by that material and the number of photons emitted at a certain wavelength (typically at the emission peak). In this context, quantum dots are known for exhibiting quantum yields that are typically much higher than that of conventional organic dyes, allowing for greater analytical sensitivity studies.

Resistance to photodegradation may be a critical issue in biological applications, especially when long term continuous monitoring of some process is desired. Typical fluorophores tend to degrade in a matter of seconds, therefore ceasing fluorescent emission. Quantum dots, on the other hand, present very high resistance against photodegradation which allows them remaining luminescent for hours or even days under continuous photoexcitation (Wu *et al.*, 2002).

Nevertheless, despite the great advantages "promised" by semiconductor quantum dots on the development of applications in the fields of biomedicine and biology, they are not likely to replace organic dyes as fluorescent labels just as yet. The challenges to overcome before quantum dots can find a wider acceptance in biological research include: lowering considerably their cost, control (limit) their inherent biological toxicity, and reduce the size-increase that aqueous-solubilization and bioconjugation imparts on the nanocrystals. The later issue is of great importance regarding, particularly, *in vivo* applications where the size reached by quantum dots may compromise the biological function under study.

## 1.4.3. Synthesis and Functionalization

### 1.4.3.1. Synthesis

The fact that the size-dependent properties of quantum dots, in colloidal solutions, are more obviated when their size distribution is narrow motivated the development of synthesis strategies that allow finely controlling the distribution of the nanocrystals size. Particularly, methods for synthesizing CdSe-based quantum dots have progressed rapidly and, now, colloidal solutions may be produced with (narrow) emission peaks that span entire visible spectrum. Subsequently, CdSe has became one of the most common chemical compositions of quantum dots in biological applications (Smith *et al.*, 2006).

The overall process of preparation of quantum dots for biological applications involves, typically, four main steps (Smith *et al.*, 2006):

(1) synthesis of the quantum dot core (typically CdSe) in a high-temperature organic solvent;
(2) epitaxial growth of an inorganic shell (typically ZnS) on the (CdSe-)core;
(3) phase transfer from organic to aqueous solution; and
(4) linkage of biologically active molecules to the quantum dots surface to render functionality, or linkage of biologically inert polymers to minimize biological activity.

Based on the work developed by Murray and coworkers (Murray *et al.*, 1993), the most common and reproducible methods for the synthesis of nearly monodisperse quantum dots (cores) involve the addition of semiconductor precursors to a liquid coordinating solvent at high temperature. That coordinating solvent, typically consisting of trioctylphosphine oxide (TOPO) and trioctylphosphine (TOP), contains basic functional groups that can bind to the quantum dots surfaces during growth and prevent the formation of bulk semiconductors (Figure 1.23A). Additionally, the alkyl chains composing those coordinating ligands render quantum dots that are sterically stable in many nonpolar solvents. Since, the quantum dots growth dynamics is dependent on parameters such as the temperature, the initial precursors concentration and the solvent composition, it is possible to synthesize (for instance CdSe) quantum dots with sizes ranging from 2 to 8 nm corresponding to narrow emission peaks between 450 and 650 nm, just by fine adjustment of those parameters.

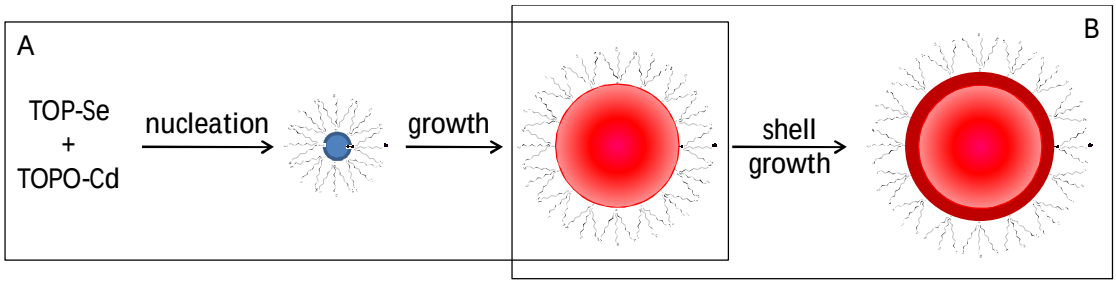


**Figure 1.23** – (A) Growth of the quantum dots cores (e.g. CdSe) in coordinating solvents. (B) Growth of a higher band gap semiconductor shell (e.g., ZnS) over the (CdSe) cores. (Adapted from: Bailey *et al.* 2004).

Quantum dots have high surface area to volume ratios and, thus, a large fraction of the constituent atoms are at the nanoparticles surfaces. This means that, at the quantum dots surfaces, there are many atomic or molecular orbitals that are not completely bonded. These so

called “dangling” orbitals may form bonds with organic ligands such as TOPO, leading to the formation of electrically insulating monolayers that serve to passivate the quantum dots surfaces by maintaining the internal lattice structure and protecting the inorganic surface from external effects. However, the strength of those bonds is not very high and the core becomes physically accessible upon desorption of ligands. For this reason, usually, it is considered advantageous to promote the formation of a shell of another semiconductor material over the quantum dots cores (Figure 1.23B). Using materials (such as ZnS) possessing bandgaps wider than that of the underlying core (such as CdSe) results in strong electronic insulation and consequently in enhanced photoluminescence efficiency (which presently can reach close to the unity; McBride *et al.*, 2006). Furthermore, that higher band-gap semiconductor protective shell is found to provide also a physical barrier to degradation or oxidation of the core surface.

However, due to the coordinating agents that remain on their surfaces, quantum dots synthesized by the methods described above are hydrophobic in nature and, thus, incompatible with biological systems. Consequently, several phase transfer strategies have been proposed to make hydrophobic quantum dots water-soluble and usable as biological reporters. From the general point of view, there are two main routes by which hydrophobic quantum dots are rendered water-soluble (Bailey *et al.*, 2004; Smith *et al.*, 2006; Klostranec and Chan, 2006) (Figure 1.24):

(1) chemically exchanging the ligands, or
(2) coating with amphiphilic polymers by hydrophobic-hydrophobic interactions with the TOPO molecules that remain on the nanocrystals surfaces after synthesis.

In the chemical-exchange method, TOPO-coated quantum dots are mixed in a solution containing a large excess of bifunctional molecules [such as mercaptoacetic acid or (3-mercaptopropyl) trimethoxysilane] which possess a thiol functional group at one of its tips and a polar functional group at the opposite tip (Figure 1.24A). The thiol groups compete with the phosphonic oxides (from TOPO) for the metal atoms on the quantum dots surfaces, leading to the displacement of the later by the former, which renders the quantum dots soluble in aqueous solvents. However, this technique is known to result in rapid flocculation and decrease in fluorescence quantum yield of the quantum dots.

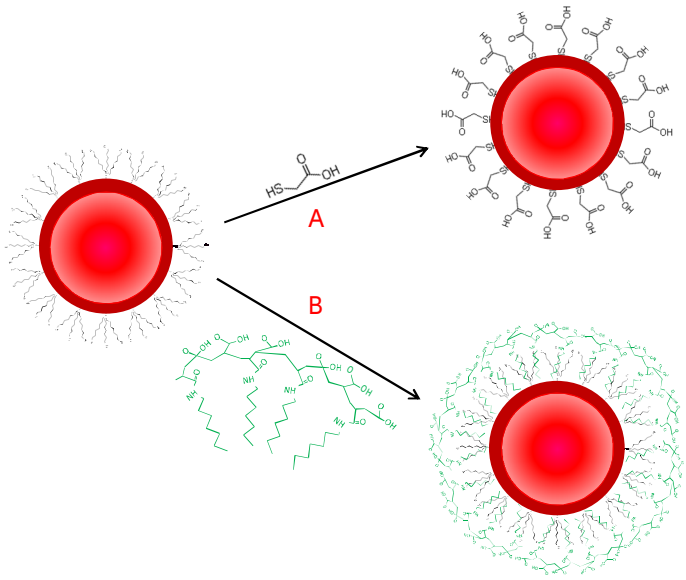


**Figure 1.24** – Illustration of the two general strategies to disperse hydrophobic quantum dots in aqueous solutions. (A) Ligands exchange reaction: TOPO is replace by bifunctional ligands such as mercaptoaceptic acid. (B) Native TOPO is maintained on the quantum dots surfaces and are covered with an amphiphilic polymer. (Adapted from: Bailey *et al.* 2004)

To overcome the downsides of the ligand exchange methods, an alternative was developed in which the native TOPO molecules are retained on the quantum dots surfaces and covered with amphiphilic polymers [such octylamine-modified polyacrylic acid] which interact with the TOPO molecules through hydrophobic-hydrophobic interactions (Figure 1.24B). This method renders water-soluble quantum dots that remain stable for long periods of time due to the the protective hydrophobic bilayer encapsulating each quantum dot. The disadvantages of this technique regard its complexity, the high cost of the coating reagents and also the non-trivial increase of the overall size the quantum dots after coating.

### 1.4.3.2. Functionalization

In practice, most water solubilization methods result in quantum dots covered with carboxylic acid groups (Smith *et al.*, 2006). Subsequently, in the context of biosensing applications, the conjugation schemes most commonly used for the attachment of biomolecules to carboxylated quantum dots are those depicted in Figure 1.25 (description on the text below). The choice of a bioconjugation route always depends critically on the particular biochemical characteristics of the system under investigation.

Covalent coupling of biomolecules to carboxylated quantum dots surfaces is performed, typically, via EDC/NHS (1-Ethyl-3-[3-dimethylaminopropyl]carbodiimide hydrochloride / N-

hydroxysulfosuccinimide ) coupling chemistry. In that reaction, EDC converts the carboxylic acids into amine-reactive *O*-acylisourea intermediates which, on their turn, are converted into more stable amine-reactive sulfo-NHS esters by the NHS reagent. The modified quantum dots can thus be covalently coupled to biomolecules of interest possessing primary amino functional groups (innately or modified) by the formation of amide bonds (Figure 1.25A). Proteins, DNA and peptides are among the biomolecules types that have been covalently conjugated to carboxylated quantum dots following this strategy (Cui *et al*,. 2007; Slocik *et al.*, 2007; Algar and Krull, 2006).

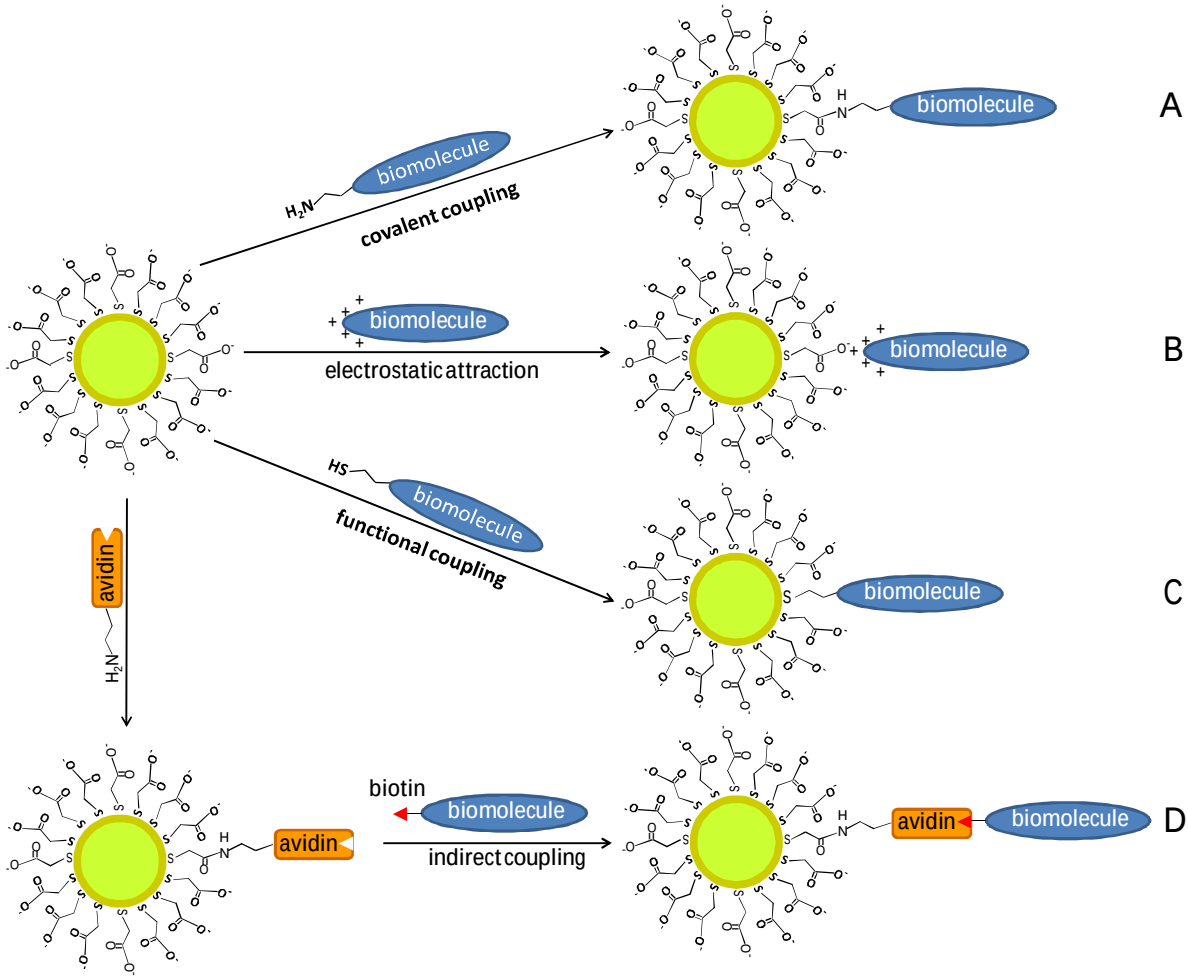


**Figure 1.25** – Schematics of the most common methods to conjugate carboxylic acid covered quantum dots to biological molecules such as proteins, peptides, nucleic acids, or small organic molecules. For the sake of clarity, the elements of this scheme are not proportional in size. . (Adapted from: Smith *et al.*, 2006).

Since the carboxylated surfaces are negatively charged in neutral and basic buffers, electrostatic attraction can be used to bind positively charged molecules to the quantum dots surfaces (Figure 1.25B). This technique has been used, for instance, to coat quantum dots with

positively charged avidin which can be used as bridge to attach biotinylated biomolecules (Goldman *et al.*, 2006).

Alternatively, biomolecules containing basic thiol functional groups may interact directly with the quantum dots surfaces as ligands, replacing the carboxyl-terminated ligand molecules used in the aqueous solubilization procedure (Figure 1.25C). Gao and coworkers (Gao *et al.*, 2002), for instance, were able to replace the mercaptoacetic acid on the quantum dots surfaces by denatured BSA whose disulfide bonds had been previously converted into sulfhydryl groups (-SH). The quantum dots functionalized using this strategy shown a few advantages: (1) high stability, (2) recovering of the quantum yields to values close to those measured in the organic synthesis-solvent and (3) the layer of denatured BSA on the surfaces of the quantum dots contained several functional groups (such as amine and thiols) allowing covalent conjugation to other biomolecular probes using standard crosslinking procedures

Quantum dots modification with probe biomolecules has been made also through high-affinity avidin–biotin binding (Figure 1.25D). Generally, in this method, avidin (or streptavidin) molecules are first immobilized on the quantum dots carboxylated surfaces, using the same EDC/NHS chemistry describe above. Second, the biomolecules intended to be used as probes are modified with a biotin extension. Third, the biotin-modified biomolecule-probes are linked to the quantum dots surfaces via avidin-biotin interaction. Kampani and coworkers, for instance, used commercially-available streptavidin-coated quantum dots to track and characterize the attachment of biotin-modified human cell leukemia virus type 1 (HTLV-1) on the cell receptors (Figure 1.26, Kampani *et al.*, 2007).

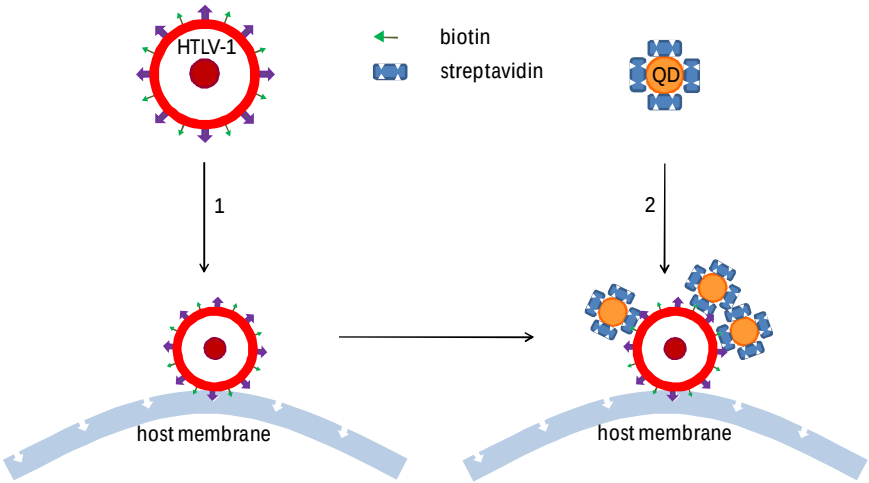


**Figure 1.26** – Representation of the quantum dot-based binding assay to quantitate HTLV-1 binding to target cells. (Adapted from: Kampani *et al*, 2007)

Quantum dots may also be coated with inert hydrophilic polymers (such as polyethylene glycol) and used as nonfunctional probes, which reduces nonspecific adsorption and increases the colloidal stability. As an example, quantum dots covered with cationic polyethylene glycol were used as efficient intracellular labeling agent (Lee *et al.*, 2008).

### 1.4.4. Biosensing

The advantages that may be achieved by replacing traditional organic dyes with inorganic semiconductor quantum dots (in biosensing assays) are translated by the increasing number of reports (in an increasing variety of application types) published in the last few years. Here, examples are given of the application of quantum dots in some of the most prominently growing biosensing research areas, namely: immunosensing, DNA sensing and resonance energy transfer assays.

#### 1.4.4.1. Immunosensing

The advantages offered over conventional dyes (subsection 1.4.2) are leading quantum dots to be increasingly used in immunosensing (Goldman *et* al, 2006). Particularly, the high photostability of quantum dots has been used for improved sensing sensitivity (relative to traditional dyes), while the size tunable photoluminescence together with the broad absorption spectra allowed for multiplexing.

Kerman and coworkers, for instance, used commercially available streptavidin-coated quantum dots to detect an important cancer marker with a level of sensitivity that allows diagnosing prostate cancer in undiluted human serum samples (Figure 1.27, Kerman *et al.*, 2007). Using a somewhat similar strategy, Goldman and coworkers, attached four different toxin-antibodies to four differently colored quantum dots, and developed a multiplexed assay to simultaneously detect cholera-toxin, ricin, shiga-like toxin 1 and staphylococcal enterotoxin B (Figure 1.28, Goldman *et al.*, 2004).

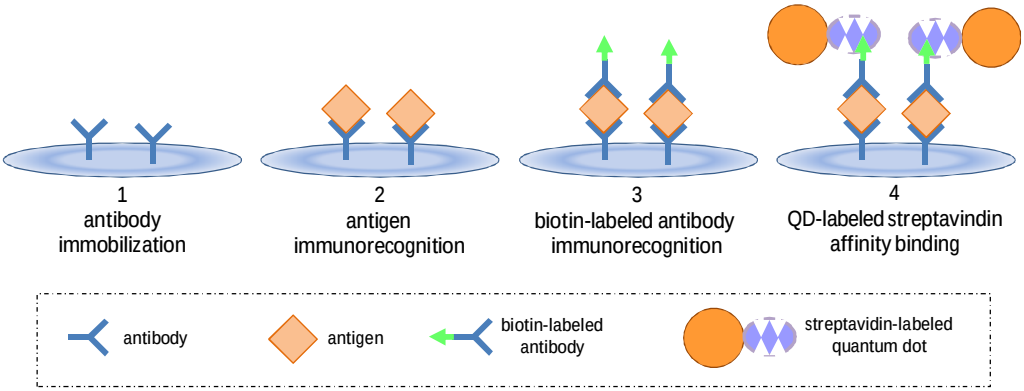


**Figure 1.27** – QD-based immunoassay for cancer-marker detection. (1) The antibody of the target-protein is immobilized on a solid substrate; (2) the target-protein is recognized by the immobilized antibodies; (3) secondary antibodies are allowed to bind to the target-proteins on the substrate; (4) Streptavidin-conjugated quantum dots are captured on the substrate through biotin-streptavidin affinity. (Adapted from: Kerman *et al.*, 2007)

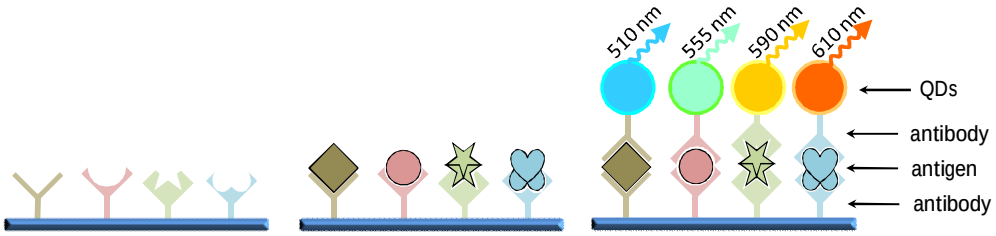


**Figure 1.28** – Schematics of the strategy for the simultaneous detection of four different toxins. First, antibodies against all four toxins were adsorbed on a solid surface. Second, the immobilized antibodies were exposed to a mix of all four toxins. Third, toxins were detected by anti-toxin antibodies conjugated to the various QDs. (Adapted from: Goldman *et al.*, 2006)

Immunolabeled quantum dots have also been used, for instance, on the identification of bacterial and protozoan cells. A multiplexed assay has been developed through which *Cryptosporidium parvum* and *Giardia lamblia* cells immobilized on a solid substrate were simultaneously detected (Zhu *et al.*, 2004). The biotinylated antibodies were attached to two differently colored streptavidin-coated quantum dots, and allowed to bind to the cells via immunorecognition.

### 1.4.4.2. DNA assays

Quantum dots are being introduced as fluorescent probes on the development of a range of nucleic acid sensing modalities. The DNA-microarrays technology is, perhaps, the one with the highest potential for application of quantum dots, given the possibility of tuning their emission wavelength in narrow symmetric bands which allows for efficient multiplexing. In this context, Gerion and coworkers adapted traditional cDNA microarray technology for the simultaneous specific detection of hepatitis B and C genotypes using DNA-conjugated quantum

dots (Gerion *et al.*, 2003). This study shown that using quantum dots as signal reporters in cDNA microarrays allow to suppress signal leakage between neighbor detection channels, which was a marked improvement compared to certain sets of organic dyes. In the same report, researchers demonstrated also the efficiency of DNA-conjugated quantum dots as probes in SNP (single-nucleotide-polymorphisms) human genotyping.

Another promising detection scheme is based on multicolor-colocalization of quantum dot probes for genetic analysis. The three genes required to positively identify the *Bacillus Anthracis* strain were successfully detected using one such assay scheme (Ho *et al.*, 2005). The strategy went by labeling target and probe sequences with a set of three differently colored quantum dots (Figure 1.29). Upon mixing QD-labeled target and probes sequences a three color code is generated as a result of complementary DNA hybridization. Noteworthy, is the advantage of this detection scheme in avoiding the need of a solid substrate for separation of unbound probes.

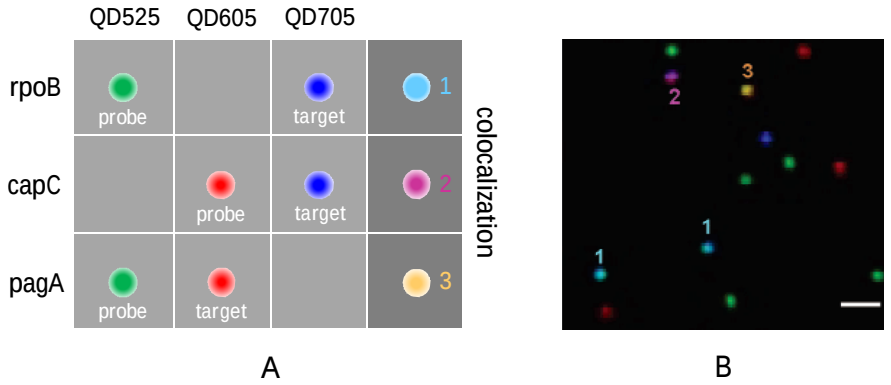


**Figure 1.29** – Multiplexed analysis of anthrax-related genetic targets for pathogenicity. (A) color pallet for the three QD-labeled target-probe pairs and their resulting colocalized fluorescent images upon hybridization. (B) Fluorescent image showing detection of the three genetic targets. (Adapted from: Ho *et al.*, 2005)

Additionally, quantum dots have also been used to encode latex beads (Qbeads), allowing the generation of unique spectral signatures by mixing nanocrystals with different emission wavelengths at different concentrations. Xu and coworkers, for instance, have proposed a biosensing method for SNP genotyping using 10 differently coded Qbeads which were generated by the combination of quantum dots with two different sizes at different concentrations (Xu *et al.*, 2003).

### 1.4.4.3. RET-based assays

Resonance energy transfer (RET) is defined as the non-radiative energy transfer between the excited states of donor and acceptor chromophores. The RET phenomenon has been described mostly between pairs of fluorescent organic dyes, where the energy transfer is detected by an increase of the acceptors fluorescent emission with a concomitant reduction of the donors fluorescent emission. Nevertheless, when the acceptor chromophore is a quencher that releases non-radiatively the energy it receives from the donor, RET may also be detected just by the observation of a reduction of the donors emission. Generally, two essential conditions must be complied for the occurrence of RET: (1) the emission spectrum of the fluorescent donor overlapping the absorption spectrum of the acceptor and (2) the physical distance between donor and acceptor should be in the range between 1 and 10 nm (Blagoi *et al.*, 2006). Since the RET process depends directly on the donor-acceptor separation distance, this phenomenon has been commonly used in biosensing assays aiming the colorimetric detection of target-probe binding events as well as of molecular structural changes.

RET-based studies involving pairs of organic dye molecules as the donor-acceptor complexes are often limited by cross-talk caused by spectral overlap of the donor and acceptor emission (Willard *et al.*, 2001). Also, the need for significant overlap between the emission and absorption spectra of the donor and acceptor, coupled with the narrow absorption spectrum of conventional organic dye molecules, makes it difficult to avoid direct excitation of the acceptor molecules at the excitation wavelength of the donor. On the other hand, promising advantages are being found in substituting traditional organic dyes by quantum dots as RET donors. Particularly, given that (1) the fluorescence emission of quantum dots is narrower than that of the organic dyes and (2) the peak position of the quantum dots emission can be continuously tuned in the visible optical band, the quantum dot emission can be perfectly matched to the absorption band of any acceptor (thus increasing energy transfer efficiency) and spectral leakages into the acceptor channel may be considerably reduced (refer to Figure 1.22, in pag 52). Additionally, the quantum dots broad absorption spectrum at wavelengths lower than that of the emission peak allows choosing an excitation wavelength that corresponds to the minimum of the acceptor absorption, contributing to substantially reducing direct excitation of the acceptor.

Currently, quantum dots are being used as RET donors in a variety of biosensing assays, pairing with acceptors such as organic fluorophores, non-emissive dyes or gold nanoparticles, to

detect a diversity of targets including proteins, antibody fragments, DNA sequences and DNA aptamers. (Wang *et al.*, 2002; Medintz *et al.*, 2003; Clapp *et al.*, 2004; Wargnier *et al.*, 2004; Goldman *et al.*, 2005; Levy *et al.*, 2005).

For instance, luminescent CdSe-based quantum dots have been used as energy donors in the development of a prototype sensor for sugar detection, based on a competitive RET assay for maltose (Medintz *et al.*, 2003). Semiconductor nanoparticles conjugated to maltose-binding proteins were used as the RET donors, while quencher dyes coupled to cyclodextrin served as the RET acceptors. In the absence of target (maltose), cyclodextrin-dye complexes occupy the protein binding sites at the surfaces of the quantum dots, resulting in the decrease of the quantum dots fluorescence via RET to the quencher dyes now at close proximity. When maltose is mixed in solution, it replaces the cyclodextrin-dye complexes at the quantum dots surfaces leading to the recovery of the quantum dots fluorescence (Figure 1.30).

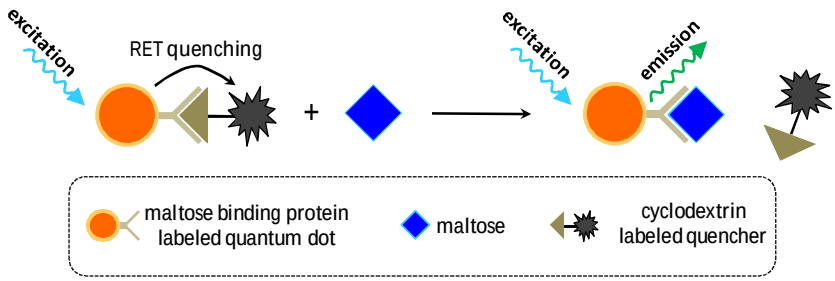


**Figure 1.30** – Schematics of the RET-based maltose-sensor with quantum dots as energy donors. (Adapted from: Costa-Fernandez, 2006)

Quantum dots have also been used as RET donors in the detection of DNA hybridization by, for example, forming molecular beacons with organic dye acceptors (Kim *et al.*, 2004). Molecular beacons are composed by single-stranded oligonucleotide hybridization probes that form a stem-and-loop structure and by a chromophore/quencher pair (Figure 1.31). The loop section contains an ssDNA probe sequence that is complementary to the target sequence, while the stem section is formed by complementary sequences located on either side of the probe sequence. A fluorescent chromophore is attached to one end of the DNA-probe sequence and chromophore-quencher is attached to the other end of that sequence. In the absence of targets, the molecular beacon is in its dark state because the "looped" conformation brings the chromophore and the quencher into close proximity, allowing RET to occur. When the target DNA is mixed in solution, it forms probe-target hybrids that are longer, more stable, and more rigid than the stem hybrid. Consequently, the molecular beacon undergoes a spontaneous conformational reorganization that forces the stem hybrid to dissociate, resulting in the splitting

apart of chromophore and quencher, thus restoring fluorescence. Given their very high extinction coefficients, quantum dots offer increased signal-to-background ratios as donors in molecular beacons, compared to traditional organic dyes (Kim *et al.*, 2008).

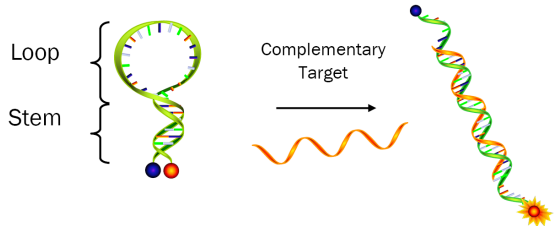


**Figure 1.31** – Conformational diagram of a molecular beacon in the presence and in the absence of the complementary target. (Adapted from: Kim *et al.*, 2008)

Given that RET efficiency depends on the center-to-center separation distance between donor and acceptor, the size of bioactive quantum dots is the main factor that limiting their wider use as RET donors in biosensing applications. In practice, bioconjugated quantum dots are about one order of magnitude larger than traditional organic dyes, reaching sizes as large as 50 nm. Although the fluorescence originates in their relatively small core-shell nucleus (with sizes typically below 8 nm), two factors contribute to significantly increase the overall size of water-soluble bioconjugated quantum dots: (1) the hydrophilic coating layer(s) that render(s) quantum dots water soluble and (2) the biomolecular entities immobilized on the quantum dots surfaces. Thus, in most of the resonance energy transfer biosensing designs where quantum dots act as donors, their water-solubilization layers are made as thin as possible and the bioreceptors are attached as close as possible to the quantum dots surfaces.

Alternatively, RET efficiency at higher distances as been improved by quenching the quantum dots photoluminescence with gold nanoparticles (Gueroui and Libchaber, 2004). Even though the nature of this quenching mechanism is not clearly understood yet, demonstrations of its utilization as sensing strategy have been reported. For instance, an imaging agent that utilizes quantum dots quenched by gold nanoparticles was developed to detect proteolytic activity (Chang *et al.*, 2005). The detection system consists of quantum dots linked to AuNPs through "user-defined" peptide sequences specific for a protease of interest (Figure 1.32). These QD–peptide–AuNPs imaging probes are activated upon peptide cleavage by a specific target protease, which splits apart quantum dots and AuNPs. Consequently quenching is ceased because energy transfer no longer occurs between AuNPs and QD, allowing strong radiative emission by the QDs.

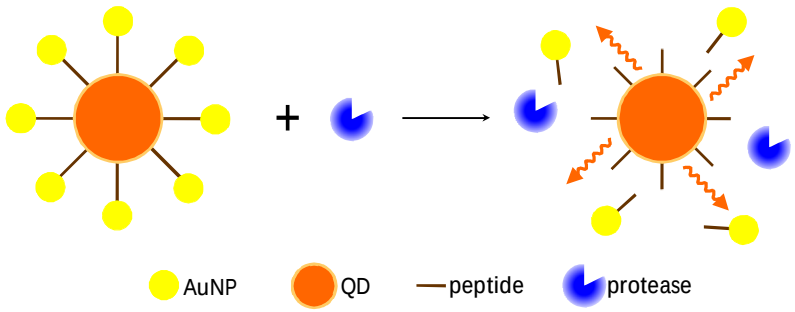


**Figure 1.32** – Illustration of the activation of the QD-AuNPs based probe. Protease cleavage of the peptide linker releases the AuNPs that were suppressing QDs fluorescence. (Adapted from: Chang *et al.*. 2005)

# 2. Summary

The primary aim of this research thesis was the development of nanoparticle-based colorimetric biosensing strategies. With that objective in mind, two different types of water-soluble colloidal nanoparticles were selected: gold nanoparticles and semiconductor nanoparticles (commonly known as Quantum Dots).

This dissertation is composed of 5 main chapters besides the current one. The first chapter introduces to some of the theoretical and experimental knowledge on the unique size-dependent properties and applications published to the date concerning the two types of nanoparticles systems under investigation here. Particular focus was put on the description of those properties that confer nanoparticles their biosensing capabilities.

Third chapter reports a non-crosslinking based biosensing method that relies on the different electrostatic properties of single-stranded-DNA, double-stranded-DNA and colloidal gold nanoparticles to detect hybridizated complementary DNA single-strands.

In the fourth chapter**,** the accumulated knowledge from the previous chapter is used on the development of a biosensing strategy to detect the presence of *Influenza Virus* antigens in solution using, to that end, especially specifically-engineered ssDNA sequences (also known as aptamers) and solutions of non-functionalized gold nanoparticles.

In fifth chapter, key conceptual steps were investigated in the development of colorimetric immunosensors with gold nanoparticles. Here, the streptavidin–biotin pair was used as “ideal” target-probe pair to demonstrate the usefulness of gold nanoparticles colloids as colorimetric signal transducing agents to detect proteinaceous analytes in solution.

Chapter six addresses the preliminary studies performed to evaluate the

photoluminescence behavior of water-soluble CdSe/ZnS core/shell quantum dots under two different conditions: (1) long-term photo-excitation with laser light and (2) when exposed to different temperatures. The responses obtained under those conditions are considered important factors in the context of the design and preparation of biosensing applications with quantum dots.

Finally, chapter 7 presents the concluding remarks of the current work and discusses future pathways.

# 3. DNA sensing

The uncovered gold nanoparticles colloidal stability may be greatly influenced by environmental factors of the medium in which they are embedded, namely the buffer's ionic strength, pH and presence of (bio)chemical species (Myers, 2005; Kelly *et al.*, 2003; Link, 1999; Miller and Lazarides, 2005). When conditions are such that the colloidal stability disappears, flocculation or aggregation of the gold nanoparticles may occur. As a result, spectral alterations are observed due to the shifting to higher wavelengths of the SPR peak and due to the spectrum broadening, which come both as a consequence of the coupling of SPRs of the individual nanoparticles now in close proximity (Lakowicz, 2005; Rechberger *et al.*, 2003; Su *et al.*, 2003).

One of the many applications in which colloidal gold nanoparticles have found application, namely by observing the alterations of their colloidal character, is on the detection of hybridization of single strands of DNA (Chen *et al.*, 2008; Storhoff *et al.*, 2000; Thaxton *et al.*, 2006). However, the published literature regarding this subject relays typically on *SH* terminated DNA target and/or probe strands to functionalize the gold nanoparticles surfaces, using sometimes complex labeling or surface functionalization chemistry.

In this chapter, an alternative and simple non-crosslinking biosensing colorimetric method is presented to perform the detection of oligonucleotides hybridization, relying "simply" on the different electrostatic properties of single-stranded-DNA, double-stranded-DNA and colloidal gold nanoparticles. Furthermore, it is determined a mathematical expression that predicts the degree of aggregation of gold nanoparticles as a function ssDNA and salt concentration in the colloidal solution.

## 3.1. Introduction

Until recently, it has been assumed that DNA should "fill" electrostatic repulsion towards gold nanoparticles (AuNPs) given the fact that, in its native configuration, DNA is coiled in such a way that the negatively charged phosphate backbone is exposed to the aqueous solution, facing the negatively charged AuNPs surfaces (Graham *et al.*, 2000; Li and Rothberg, 2004). However, recent reports from Huixiang Li (Li *et al.*, 2007) shown that increased stability of colloidal solutions results when single-stranded oligonucleotide sequences (ssDNA) are mixed into colloidal solutions of bare AuNPs. Under these circumstances the colloid spectrum remained practically unchanged even when challenged with higher ionic strength buffers that otherwise would induce the aggregation of unprotected gold. This protection against aggregation effect was attributed to the adsorption of the ssDNA molecules on the AuNPs through the electrostatic interaction of the ssDNA positively charged hydrogen bases and the negatively charged AuNPs surfaces (Figure 3.1). The AuNPs with ssDNA adsorbed on their surfaces have an increased number of superficial negative charges due to the ssDNA exposed phosphate backbone enhancing the inter-repulsion between AuNPs and consequently their stability against salt-induced aggregation (Li and Rothberg, 2004).

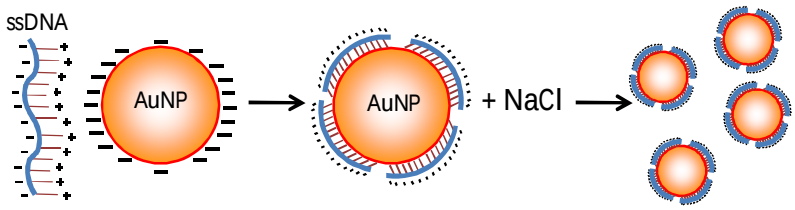


**Figure 3.1 –** Representation of the electrostatic (attractive) interaction between bare AuNPs and single-stranded DNA, and the protection-against-salt-induced-aggregation effect of the later over the former.

The same authors have also shown that if double-stranded oligonucleotide sequences are mixed into the AuNPs colloidal solution instead of ssDNA then, when the colloids are challenged with identical salt concentrations, a SPR peak shift to higher wavelengths is observed and attributed to the AuNPs aggregation (Figure 3.2). This was considered to be an indication that, contrary to what happens with the ssDNA, the dsDNA does not enhance the colloid stability against salt-induced aggregation, revealing a new strategy that allows determining if there is complementarity between DNA strands (Li *et al.*, 2007).

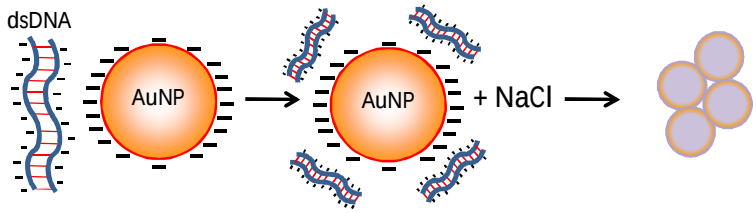


**Figure 3.2** - Representation of the electrostatic (repulsive) interaction between bare AuNPs and double-stranded DNA, with no protection-against-salt-induced-aggregation.

Here, the work developed by Huixiang Li and co-workers concerning detection of DNA complementarity using non-functionalized AuNPs, was successfully reproduced. Furthermore, a strategy was developed to quantify the joint effects that several factors may have on the colloidal stability of AuNPs, namely regarding their use in thiol-free-DNA biosensing. Specifically, the joint effects that different amounts of a salt (NaCl) and DNA have over the colloidal stability of 9.6 nm AuNPs were studied. The results obtained were analyzed considering a full-factorial-design, and a mathematical expression was determined that predicts the influence of both factors on the AuNPs degree of aggregation, as measured through the flocculation parameter.

## 3.2. Materials

Colloidal AuNPs with 9.6 nm average diameter were obtained from British Biocell International, at concentration of approximately 9.5 nM. 20-base lyophilized oligonucleotide single stranded sequences (CCGACCTCGAGCTGAGCTCC) (ssDNA) and their complements (csDNA) were purchased from Thermo-Scientific, and solubilized in milli-Q water to concentrations of 100 µM. Aliquots of 1 µM ssDNA and csDNA were also prepared in milli-Q water. Sodium chloride and magnesium chloride were obtained from Merk.

## 3.3. Experimental Methods

### 3.3.1. dsDNA hybridization and purification

20 µM aliquots of both ssDNA and csDNA were prepared in 10 mM a phosphate buffer solution containing 300 mM of NaCl and 25 mM of $MgCl_2$. Equal volumes of these ssDNA and csDNA solutions were mixed on the same vial, vortexed and heated to 65 ºC for 5 minutes. This solution was left to cool to room temperature and then left to rest overnight. The resulting solution was then purified by electrophoresis on a 1.5% agarose gel (Figure 3.3), from which the

dsDNA fraction was extracted to milli-Q water using a gel extraction kit (Agarose Gel DNA Extraction Kit, from Roche). The extracted dsDNA solution was then set to a concentration of 1 µM in milli-Q water (as measured by the optical absorption at 260 nm).

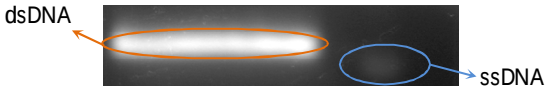


**Figure 3.3** – Image of an agarose gel (under UV illumination) used to purify double-stranded DNA from non-hybridized single-strands.

### 3.3.2. Sample preparation

Chosen volumes of 1 µM ssDNA (or dsDNA) were diluted in different volumes of milli-Q water on different vials, resulting in 50 µL solutions with ssDNA (or dsDNA) concentrations ranging from 39.8 to 159.5 nM. Then, 25 µL of unmodified stock AuNPs were mixed into each vial (final concentration of approximately 3.2 nM), rendering final ssDNA (or dsDNA) to AuNP ratios of 0.5, 1.0, 1.5 and 2.0 times that of the maximum-estimated-coverage (m.e.c.) considering a 20-base ssDNA.

[This m.e.c. was calculated taking into consideration the following geometries (Sandström *et al.*, 2003): (1) cylindrical shapes for both the single- and double-stranded DNA; (2) a length of 0.34 nm per base pair and a helix diameter of 4 nm, for the double-stranded DNA; (3) a length of 0.43 nm per base pair and a diameter of 2 nm, for the single-stranded DNA; and (4) that all the adsorbed (single-strands) are lying down on the AuNPs surfaces in a compact form. Thus, it was estimated a maximum coverage with close to 17 single-strands or 11 double-strands of DNA per AuNP.]

One minute upon introducing the gold nanoparticles into the ssDNA (or dsDNA) solutions, equal volumes of NaCl solutions set at 3 different stock concentrations were mixed into each vial and shaken, resulting in equal volume samples with final NaCl concentrations of 50, 100 and 150 mM. Table 3.1 summarizes the characteristics of the samples prepared (in triplicates).

The degree of aggregation of the AuNPs was then assessed at room temperature, one hour after introducing the salt, using optical absorption spectroscopy from a microplate reader (Tecan Infinite M200) and a 96 borosilicate well microplate (from Wheaton Science).

**Table 3.1** – List of the samples prepared, detailing the respective concentrations of NaCl and of DNA (either single- or double-stranded). Here: 26.5, 53.0, 79.5 and 106.3 nM of DNA correspond, respectively, to 0.5, 1.0, 1.5 and 2.0 times the maximum-estimated-coverage (m.e.c.) with 20-base ssDNA. Notice that dsDNA was mixed at the same concentrations as the ssDNA, although the estimated "hypothetical" coverages are naturally different (lower).

| Sample # | [ssDNA] (and [dsDNA]) (nM) | [NaCl] (mM) |
|---|---|---|
| **1** (and 13) | 26.5 | 50 |
| 2 (and14) | 26.5 | 100 |
| **3** (and 15) | 26.5 | 150 |
| 4 (and 16) | 53.0 | 50 |
| 5 (and 17) | 53.0 | 100 |
| 6 (and 18) | 53.0 | 150 |
| 7 (and 19) | 79.5 | 50 |
| 8 (and 20) | 79.5 | 100 |
| 9 (and 21) | 79.5 | 150 |
| **10** (and 22) | 106.3 | 50 |
| 11 (and 23) | 106.3 | 100 |
| **12** (and 24) | 106.3 | 150 |

## 3.4. Results and Discussion

### 3.4.1. Experimental

The results obtained are summarized in Figure 3.4, in terms of the flocculation parameter variation. The plotted values were calculated relative to the flocculation parameter value of bare AuNPs colloidal solutions diluted to the same final concentration in milli-Q water. One can see that, in all cases, the samples containing dsDNA (red bars) present flocculation parameter values that are very approximated to that of the respective control samples (blue bars), which were prepared following the exactly same procedure except that milli-Q water was introduced in solution instead of DNA. These results seem to confirm the hypothesis that dsDNA does not contribute in any way to the AuNPs stability against salt induced aggregation. The ssDNA containing solutions (green bars), on the other hand, have flocculation parameter values that are clearly below that of the dsDNA containing samples and that of the control samples. These results are also in agreement with previous reports, supporting the hypothesis that ssDNA enhances the stability of colloidal AuNPs against salt-induced aggregation (Li *et al.*, 2007; Li and Rothberg, 2004).

Furthermore, within each set of samples with the same salt concentrations, the flocculation parameter values decrease with the increasing ssDNA concentration, following an apparently linear behavior (Figure 3.5). It could be argued that these results, regarding an increasing protection against aggregation effect with increasing ssDNA concentration, should be expected and could be intuitively predicted. However, it should be noticed that, although the

estimated full coverage of 9.6 nm AuNPs with 20-base ssDNA is reached at a concentration of 53.0 nM approximately, the flocculation parameter values continue decreasing with even higher concentrations of single-strands, where a saturation signal would be expected.

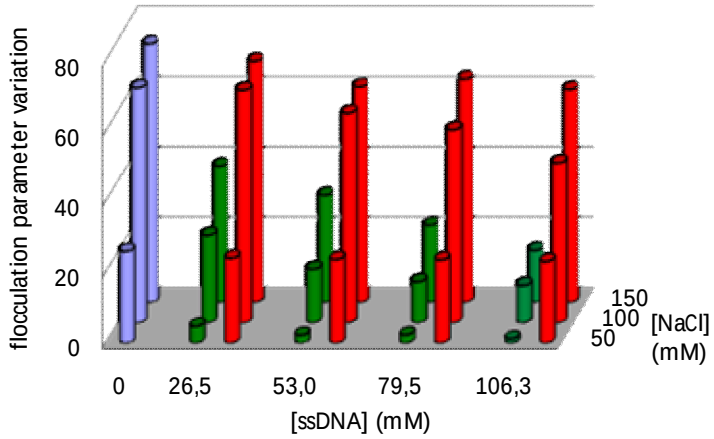


**Figure 3.4** - Flocculation parameter variation values (averaged over the triplicates), as a function of the salt and ssDNA (or dsDNA) concentrations. The values presented are relative to the flocculation parameter of AuNPs diluted to the same final concentration with milli-Q water. The standard deviation (not shown) was measured below 20%. *Purple bars*: control samples (to which no DNA was mixed); *Green bars*: ssDNA containing samples; *Red bars*: dsDNA containing samples.

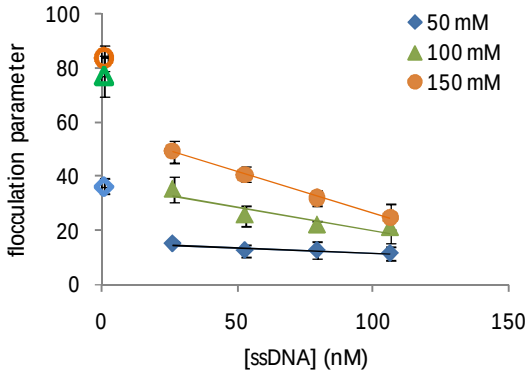


**Figure 3.5** – Variation of the flocculation parameter values as a function of the ssDNA concentration, for each set of samples with different salt concentrations. The marks at the *xx* axis origin correspond to the respective control samples (to which no DNA was mixed). The presented flocculation values are absolute and the lines were introduced to help guiding the eye.

These unexpected results may be justified if one considers that the value of m.e.c. for ssDNA was calculated using ideal geometric considerations of a "well ordered" adsorption of ssDNA on the nanoparticles surfaces (Figure 3.6), which probably is not be the case. Considering that the protection-against-aggregation effect is noticed already 1 minute upon inserting the AuNPs in the ssDNA solutions, it is proposed that the ssDNA strands adsorb, in fact, very quickly and "non-orderly" on the AuNPs surfaces, in a manner perhaps similar to that

represented in Figure 3.7. This hypothesis allows a larger number of strands to be "accommodated" on the AuNPs surfaces, justifying the increasing protection against aggregation effect at ssDNA concentrations above that of the m.e.c. due to the presence of higher numbers of negatively charged phosphate backbones. In fact, if one considers the limit case where the single-strands attach to the gold surface "standing up" (Figure 3.8), each AuNP of 9.6 nm would be able to accommodate around 92 single-strands of DNA.

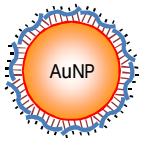


**Figure 3.6** – Representation of ideal "well ordered" adsorption of single-strands on the AuNP surface. Maximum estimated coverage ≈ 17 ssDNA per AuNP.

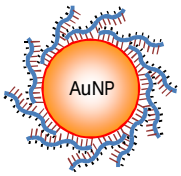


**Figure 3.7** – Representation of a non-ideal (perhaps more close to reality) adsorption of single strands of DNA on the AuNP surface.

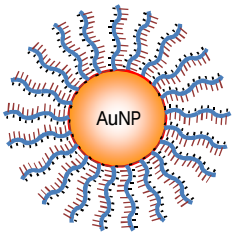


**Figure 3.8** – Representation of the extreme case of ssDNA adsorption where each strand adsorbs "standing up" to the AuNP surface. Maximum estimated coverage ≈ 92 ssDNA per AuNP.

An apparent linear dependency of the salt concentration was also found within each set of experiments with the same ssDNA ratio (Figure 3.9). It was observed that introducing salt to a final concentration of 50 mM produced very little aggregation within the range of ssDNA concentrations studied (as compared to the flocculation parameter values of ssDNA-containing samples to which no salt was mixed). For higher NaCl concentrations, however, the aggregation was quite noticeable especially with decreasing concentrations of ssDNA.

Figure 3.5 and Figure 3.9 allow withdrawing an important conclusion: the lack of parallelism of the lines in each plot is a clear indication that there is an interaction between the salt and the ssDNA concentrations contributing to the final degree of aggregation of the AuNPs.

In what follows, a method will be presented to determine a mathematical expression

aiming the quantification of the influence of both factors on the degree of aggregation.

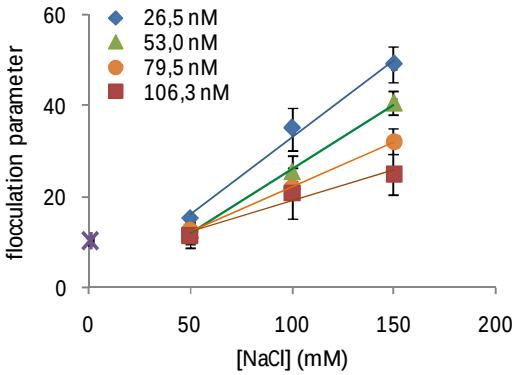


**Figure 3.9** – Variation of the flocculation parameter values as a function of the NaCl concentration, for each set of samples with different ssDNA concentrations. The mark at the *xx* axis origin corresponds to the (equal) flocculation parameter values of the samples to which no salt was mixed. The flocculation values shown are absolute and the lines were introduced to help guiding the eye.

### 3.4.2. Mathematical Design

Factorial designs are considered to be very efficient in the analysis of experiments that require the study of the joint effects of two or more factors simultaneously, allowing the effects of a factor to be estimated at several levels of the other factor, and yielding conclusions that are valid over a range of experimental conditions. In full-factorial-designs, particularly, all possible combinations of levels of the factors are investigated in each complete trial or replication. The effect of a factor, defined to be the change in response produced by a change in the level of that factor, is frequently called the main effect because it refers to the primary factors of interest in the experiment. In some experiments, the difference in response between levels of one factor is not the same at all levels of the other factors, indicating that there is an interaction term between the main factors (Montgomery, 2001).

Full-factorial designs are typically organized in four main steps: (1) defining the factors and the levels over which they are to be studied; (2) choosing the type of design; (3) choosing the type of response; and (4) performing the mathematical modeling.

In the current study, two factors were investigated in what concerns their influence over the AuNPs degree of aggregation: NaCl concentration (in the range of 50 to 150 mM) and DNA concentration (in the range of 26.5 to 106.3 nM). The choice of full-factorial-design type depends not only on the number of factors involved in the design but also on the number of

levels to be studied within each factor. In general, if **f** is the number of factors being investigated, and **L** is the number of levels for each factor, then an $\mathbf{L^f}$ full-factorial-design will generate $\mathbf{L^f}$ combinations of factors. Regarding the ssDNA containing samples, it was observed that the flocculation parameter (the chosen response for measuring the AuNPs degree of aggregation) varies approximately linearly over the range of the factor levels studied (Figure 3.5 and Figure 3.9). Subsequently, only the two extreme levels of each factor (samples # 1, 3, 10 and 12 in Table 3.1) and their respective responses were used in the design (Figure 3.10), and thus a ***$2^2$ full-factorial-design*** was used for the analysis and mathematical modeling.

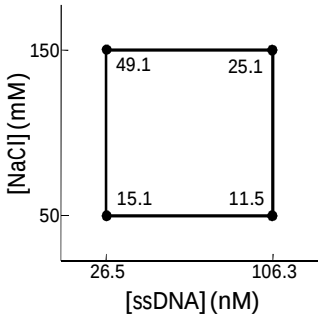


**Figure 3.10** – Factors levels and respective responses chosen for the full-factorial-design. Note that the values at the corners of the square are the averaged responses at the respective factors levels.

Data in Figure 3.10 was, thus, "inputed" in to computer analysis software (*Statistica*, from StatSoft Inc.), which outputted a mathematical expression (Equation 3.1) that may, in principle, be used for prediction of the system response at factor levels within the ranges used in the design.

$$\boldsymbol{Flocc.} = -4.104 + 0.408[\boldsymbol{NaCl}] + 0.0832[\boldsymbol{ssDNA}] - 0.0256[\boldsymbol{NaCl}][\boldsymbol{ssDNA}] \qquad \text{Equation 3.1}$$

Figure 3.11, shows a 3-dimensional plot of Equation 3.1, with the values used in the analysis represented by the blue marks at the corners.

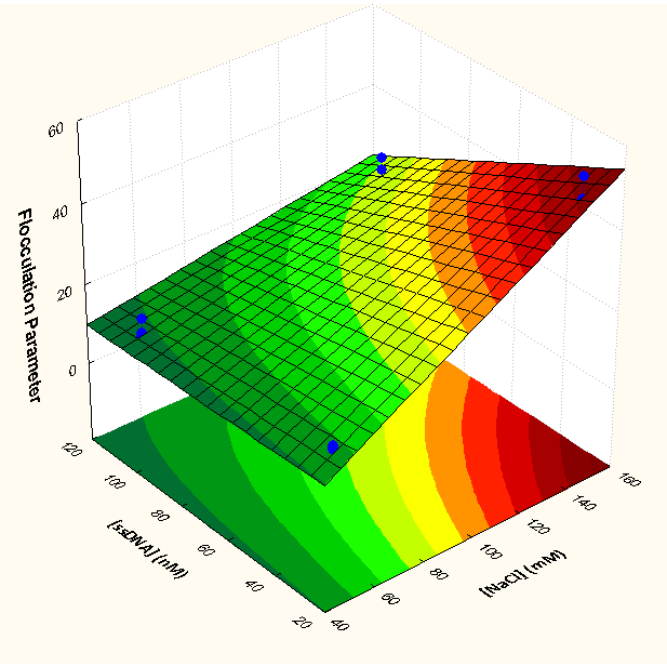


**Figure 3.11** - Three-dimensional plot of Equation 3.1, within the investigated levels range. The blue marks at the corners of the response surface represent the experimentally obtained flocculation parameter values used on the design.

Equation 3.1 shows that, in fact, the system investigated here has linear dependency of the two main effects (salt concentration and ssDNA concentration) and of an interaction term. However, the stronger response dependency comes from the salt concentration factor. The analysis of variance (Table 3.2) performed by the same computer program further confirms that the AuNPs degree of aggregation should be, in fact, significantly affected by both the main factors under study, as well as by the interaction term since their p-values are bellow 0.05.

**Table 3.2** - Analysis of Variance (ANOVA), from Statistica©. ***df***: degrees of freedom; ***F***: Fisher test, ***p-value***: probability distribution value. The correlation coefficient ($R^2$) was 0.97.

| Factor | Coeficient | Sum of Squares | df. | Mean square | F-ratio | p-value |
|---|---|---|---|---|---|---|
| constant | 4.112 | | | | | |
| [NaCl] | 0.408 | 1694,110 | 1 | 1694,110 | 200,2131 | 0,000001 |
| ssDNA : GNP | 4.429 | 570,636 | 1 | 570,637 | 67,4389 | 0,000036 |
| Interaction term | 0.136 | 313,190 | 1 | 313,190 | 37,0134 | 0,000295 |
| Error | | 67,692 | 8 | 8,462 | | |
| Total sum of squares | | 2645,629 | 1 | | | |

Furthermore, the normal probability plot of the residuals (Figure 3.12) appears to be satisfactory since all the points lie reasonably close to a straight line, lending support to the conclusions (Montgomery, 2001).

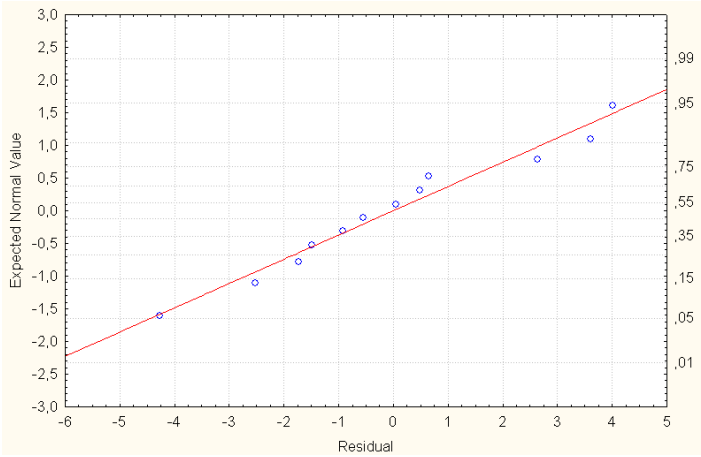


**Figure 3.12** – Normal probability plot of the residuals, from Statistica©.

Finally, considering that Statistica© outputted Equation 3.1 with a correlation factor $R^2$ = 0.97, it was expected that it should fairly well predict experimental responses within the investigated factor ranges. To determine if this was the case, all sets of factors levels (Table 3.1) were inserted in Equation 3.1 and the calculated results were compared with the experimentally measured flocculation parameter values shown in Figure 3.4. Figure 3.13 shows that, in fact, the modeled equation seems to predict well the experimental response within the experimental error, with the predicted flocculation parameter values (black open marks) superimposing, in most of the cases, the experimental flocculation parameter values (colored marks).

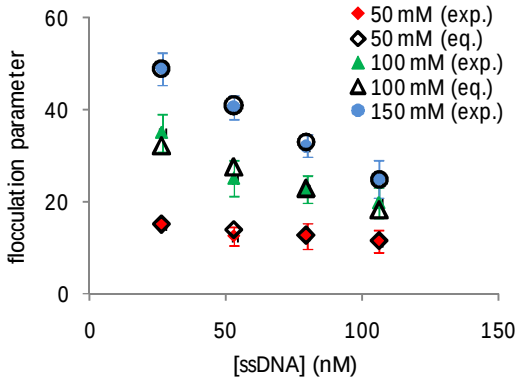


**Figure 3.13** - Comparative results between the experimentally obtained flocculation parameter values and the predicted by Equation 1.

In what concerns the samples to which dsDNA was mixed instead of ssDNA, no mathematical expression could be found that predicted the flocculation parameter values obtained (Figure 3.4) as a function of dsDNA concentration or NaCl concentration. This is probably due to the fact that, in fact, double-stranded DNA does not bind to the AuNPs surfaces

and thus the dsDNA concentration is uncorrelated with the degree of aggregation. Furthermore, within the investigated levels of salt concentration, no relation was found with the resulting flocculation parameter.

## 3.5. Conclusions

The color of colloidal solutions of AuNPs is determined mostly by their SPRs, being strongly affected if aggregation occurs. The difference in the electrostatic properties of ssDNA and dsDNA allows the design of colorimetric assays with gold colloids, capable of detecting sequence-specific untagged oligonucleotides by using only unmodified commercially available materials.

In this chapter it was demonstrated a method to detect complementarity between two strands of DNA using “only” the different electrostatic characteristics of single-stranded DNA, double-stranded DNA and colloidal AuNPs. Because in aqueous solutions ssDNA is flexible enough to uncoil sufficiently to expose it’s positively charged bases and dsDNA is “allowed” only to expose it’s negatively charged phosphate backbone, they have opposite interactions with AuNPs stabilized by adsorbed negative ions. In fact, there is a tendency for electrostatic repulsion between dsDNA and AuNPs which prevents the former from adsorbing in the gold’s surfaces, while between ssDNA and the AuNPs it is electrostatic attraction that occurs when ssDNA exposes its bases, “sticking” to the gold surfaces. Furthermore, it is proposed that ssDNA adsorbs very fast and “non-orderly” on the AuNPs surfaces, probably with only part of the bases of each strand bound (electrostatically) to the gold surfaces.

The combined influences of salt concentration and ssDNA concentration over the degree of aggregation of colloidal solutions of AuNPs were investigated. Linear relationships were found between the measured system response and both of the factors. Furthermore, the existence of interaction between both factors on the final response was also found. Thus, the experimental data was computed using a full-factorial-design and a simple mathematical expression was found, which is capable of predicting the AuNPs degree of aggregation, within the investigated range of ssDNA and salt concentrations.

# 4. Biosensing with aptamers

This chapter reports the efforts developed aiming the exploitation of the interactions between unmodified gold nanoparticles (AuNPs) and aptamers to colorimetrically detect the presence of the *Influenza Virus* in solution. Results from the previous chapter, namely the single-stranded DNA protection against salt induced aggregation were taken into consideration on the conception of the biosensing strategies developed here.

## 4.1. Introduction

### 4.1.1. Aptamers

Aptamers are single-stranded nucleic acid species engineered by chemical synthesis with lengths between 30 and 70 nucleotides approximately. Being predominantly unstructured in solution, aptamers often undergo significant conformational changes upon association with their targets (Figure 4.1), folding into specific "biorecognizable" complexes that possess highly ordered tertiary structures (Hermann and Patel, 2000; Spiridonova and Kopylov, 2002). This specific-shape folding ability attributes aptamers their high specificity and binding affinities (with dissociation constants that go down to picomolar values) towards a wide variety of target molecules (Rimmele, 2003), including: small molecules, proteins, nucleic acids, cells, tissues and organisms (Hamula *et al.*, 2006; Song *et al.*, 2008). Thus, at the present time, the range of research fields where aptamers are being used goes from biotechnological, diagnostic and therapeutic (Famulok *et al.*, 2007) applications, to anti-bioterrorism, environmental and food analysis (Tombelli *et* al, 2007).

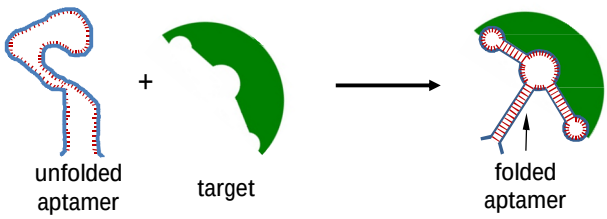


**Figure 4.1** – A successfully engineered aptamers folds to a highly specific architecture upon biorecognition/binding to its target.

Additionally, aptamers are finding applications also in the development of biosensing applications where, on one hand, the high binding affinity towards very specific targets allows predicting good detection sensitivity and, on the other hand, the significant structural changes occurring upon binding with the target elicits the use of aptamers in structural-changes related sensors (Bagalkot *et al.*, 2007; Balamurugan *et al.*, 2008). Regarding immunosensing, particularly, it is recognized that aptamers offer molecular recognition properties that rival that of the antibody-receptor based biosensors, namely (Jayasena, 1999; Klussmann, 2006; Song *et al.*, 2008):

(a) unlike the preparation of antibodies, which relies on the induction of an animal immune system, aptamers are chemically synthesized (typically by SELEX – *Systematic Evolution of Ligands by EXponential enrichment*) and can be selected in vitro (potentially) for any given target (including those non-immunogenic and toxic);
(b) aptamers produce little or no immunogenicity in therapeutic applications;
(c) once selected, aptamers can be synthesized with high reproducibility and purity from commercial sources;
(d) in contrast to antibodies or enzymes, DNA aptamers are usually highly chemically stable under a range of environments, possessing also good storage properties;
(e) the small size and versatility of aptamers allows efficient surface immobilization at high densities;
(f) association with the targets may occur either incorporating small molecules into their nucleic acid structure or being integrated into the structure of macromolecules, offering enhanced flexibility on design of novel biosensors.

### 4.1.2. Targets

Aptamers used on the work described in the current chapter were engineered by ApatRes-Gmb, targeting four different *Influenza Virus* vaccines: *Infuvac*, *Mutagrip*, *Begivac* and *Inflexal*

*V*. However, according to the supplier, aptamers have shown particular binding effectiveness against *Inflexal V*, an "*Immunopotentiating Reconstituted Influenza Virosome*" based vaccine (IRIV) that is produced in line with the annual *World Health Organization* recommendations. Thus, the vaccine *Inflexal V* was used as target on the biosensing strategies described further ahead.

The main immuno-active "ingredient" composing IRIV-based vaccines – the virosomes – are virus-like phospholipid spherical structures with a mean diameters of approximately 150 nm, that provide repetitive presentation of antigens (biologically-active viral glycoproteins: haemagglutinins and neuraminidases) to immunocompetent cells, mimicking the natural presentation of the *Influenza Virus* to the immune system (Figure 4.2).

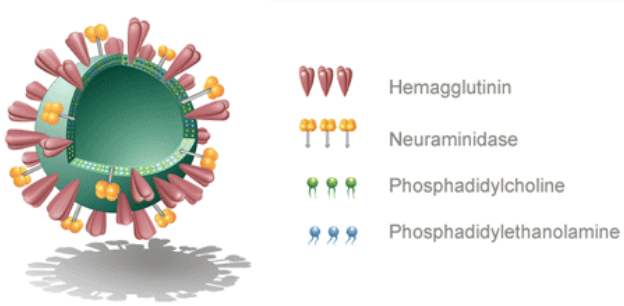


**Figure 4.2** – Schematics of an influenza virosome (from www.pevion.com).

Considering the announced similarities (Mischler and Metcalfe, 2002) between the biological/structural superficial characteristics of the influenza virus and the engineered virosomes on the vaccines, it is hypothesized that the development of a detection strategy producing positive biorecognition signals of the aptamers towards the vaccine may be extrapolated to be used also in the detection of the "real" viruses

Furthermore, in the work that follows, it is assumed that the aptamers provided by AptaRes recognize haemagglutinins as their biological targets. Thus, in order to test this assumption, purified haemagglutinins solutions were also presented to the aptamers as alternative targets.

## 4.2. Materials and Methods

### 4.2.1. Reagents

Colloidal AuNPs with 9.6 nm average diameter were obtained from British Biocell International, at concentration of approximately 9.5 nM.

Sodium chloride, potassium chloride, magnesium chloride and Tris HCl were obtained from Merk. Calcium chloride was acquired from Sigma.

20 kDa, 63-base biotinylated aptamers (of unknown sequences), targeting the vaccine of the influenza virus, were kindly donated by AptaRes Gmb. The lyophilized aptamers were first solubilized in mili-Q water and frozen at -20°C in 10 µM aliquots. Aptamers, working solutions were then prepared, at a concentration of 250 nM, in a 20 mM Tris HCl buffer at pH 7.3 (with 150 mM of NaCl, 4 mM of KCl, 1 mM $MgCl_2$ and 1 mM of $CaCl_2$).

Inflexal V® (season 2006/2007) vaccine was acquired on a pharmacy. Each 0.5 mL vaccine vial contains 45 µg of haemagglutinin activity from different viral strains [A/New Caledonia/20/99/H1N1 (IVR-116); A/California/7/2004/H3N4 (NYNCX-157); B/Shanghai/361/2002 (B/Jangsu/10/2003)]. The vaccine was diluted to halve of its initial concentration in milli-Q water and used without further purification (final concentration of haemagglutinins estimated in 592.1 nM, considering a molecular weight of 76 kDa per haemagglutinin).

Lyophilized haemagglutinins (antigen reagent 03/258) were acquired from the National Institute for Biological Standards and Control. This reagent was prepared from formalin-inactivated, partially purified A/New Caledonia/20/99 virus (IVR-116), which is one of the three strains present in the Inflexal V vaccine (season 2006/2007). The lyophilized material was ressuspended in 1 mL of milli-Q water.

### 4.2.2. Instrumentation

Optical absorption spectroscopy readings were performed on a microplate reader (Tecan Infinite M200) using a 96 borosilicate well microplate (from Wheaton Science).

### 4.2.3. Experimental Methods

Given that, in the absence of their targets, aptamers are mostly unfolded in solution, they may be regarded simply as DNA single-strands. Thus, considering the results from chapter 3, it is expected that unfolded aptamers should interact with colloidal solutions of AuNPs in much the same way as "common ssDNA", conferring to them increased protection against salt induced aggregation.

Taking advantage of that ssDNA-AuNP interaction, the immunosensing strategy designed was to challenge aptamer-protected AuNPs with a salt both in the presence and in the absence of the aptamers' target (Figure 4.3). The hypothesis raised is that, in the presence of the target, the energy of the system (aptamer + AuNP + target + salt) is minimized with aptamers folding into their three dimensional structure and binding to the targets, leaving the AuNPs unprotected against salt induced aggregation (Figure 4.3C); on the other hand, in the absence of the target, aptamer protected AuNPs solutions should hold up their colloidal stability when challenged with the same amount of salt (Figure 4.3B).

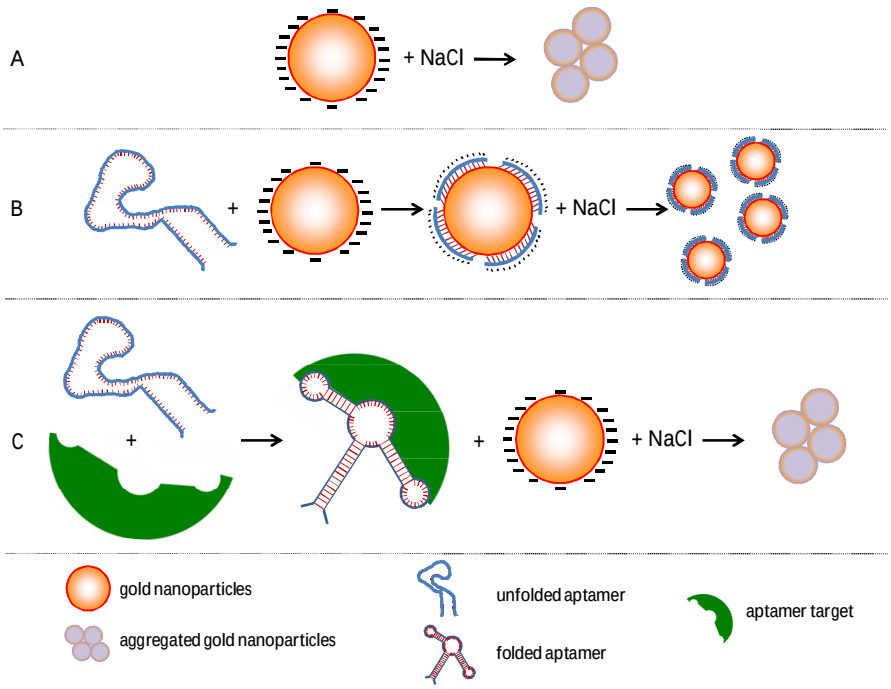


**Figure 4.3** – ***A:*** bare AuNPs aggregate when challenged with certain amounts of salt. ***B:*** in the absence of the target, aptamers present themselves sufficiently unfolded, exposing the positively charged bases to the electrostatic attraction towards the negatively charge AuNPs surfaces. Upon binding, nanoparticles acquire extra "resistance" against salt induced aggregation. ***C:*** when put into contact with its specific target, the aptamers fold, acquiring a highly ordered structure while binding to it, leaving the AuNPs unprotected against salt-induced aggregation.

Thus, the following general experimental strategy was performed to test the referred biosensing hypothesis:

(1) mix, inside a microplate well: 45 µL of milli-Q water, 5 µL of the aptamer working solution ($[aptamer]_f$ = 16.7 nM) and 25 µL of stock AuNPs ($[AuNP]_f$ = 83.3 nM), corresponding to approximately 5 aptamers per AuNP, which is roughly the maximum estimated coverage (refer to section 3.3.2);
(2) incubate the mixture for one hour, in dark, at room temperature;
(3) add to the mixture 11.6 µL of NaCl at 750mM ($[NaCl]_f$ = 100 mM);
(4) incubate the mixture for one hour, in dark, at room temperature;
(5) add 6 µL (or 12 µL) of the vaccine in to the reaction well ($[vaccine]_f$ = 38.4 nM (or 72.0 nM)), corresponding to approximately 2 (or 4) haemagglutinins per aptamer;
(6) incubate the sample for one hour, in dark, at room temperature;
(7) acquire the optical absorption spectrum of the sample and compute the flocculation parameter values.

As before, the flocculation parameter values were computed from the optical absorption spectra and used to infer on the degree of aggregation of AuNPs and hence evaluate the degree of biorecognition of the aptamers towards their targets.

## 4.3. Results and Discussion

The experimental assays were developed based on a number of assumptions taken over a set of biophysical/biochemical unknowns:

(a) the oligonucleotide sequences of the aptamers were unknown, as well as their folding and unfolding characteristics. It was assumed that:
    (i) in the absence of their specific target, aptamers present themselves sufficiently unfold to allow electrostatic attraction of their oligonucleotide bases towards the AuNPs surfaces, subsequently binding and protecting them against salt induced aggregation;
    (ii) with the specific biological target present in solution, aptamers “convert” into the folded structure and bind to them, leaving the colloidal nanoparticles

"unprotected" against salt induced aggregation;

(b) the specific target(s) within the vaccine were unknown (haemagglutinins and/or neuraminidases and/or other). It was assumed that the aptamers were targeting the haemagglutinins solely;

(c) there is no significant interaction between the targets and the AuNPs;

(d) the number and distribution of haemagglutinins on the virosomes surfaces is unknown. Thus, the calculation of the haemagglutinin ratios was based on the concentration of haemagglutinin activity as indicated by the vaccine documentation.

As referred in the introduction of this chapter, two types of substances were tested as targets for the aptamers: the *Inflexal V* vaccine and purified haemagglutinins of one of the influenza virus strains contained in that vaccine. The results obtained with each of the targets are presented below.

### 4.3.1. Target: Inflexal V

The first biosensing approach tested was to use colloidal solutions of AuNPs to detect the biorecognition of aptamers towards the vaccine *Inflexal V*. Three variations of the designed experimental strategy were tested. Their description and expected reactions are as follows (Figure 4.4).

(1) (i) the aptamer is mixed with the AuNPs and allowed to bind to their surfaces, protecting the nanoparticles against salt-induced-aggregation;

(ii) the targets are introduced in solution leading aptamers, binding into them and leaving the nanoparticles surfaces "unprotected";

(iii) the AuNPs colloidal stability is challenged with a salt, leading to aggregation if biorecognition occurred in the previous step;

(2) (i) the aptamer is mixed with the AuNPs and allowed to bind to their surfaces, protecting the nanoparticles against salt-induced-aggregation;

(ii) a salt is introduced in solution;

(iii) the targets are introduced in solution leading aptamers binding into them and leaving the nanoparticles surfaces "unprotected". Thus, aggregation should occur due to the salt

already in solution;

(3) (i) the aptamer is presented to the target and binds to it;

(ii) the AuNPs are introduced in the aptamer-target solution;

(iii) the AuNPs stability is challenged with salt, leading to aggregation because the aptamers are bound to the targets and are unable to protect the nanoparticles against the salt induced aggregation

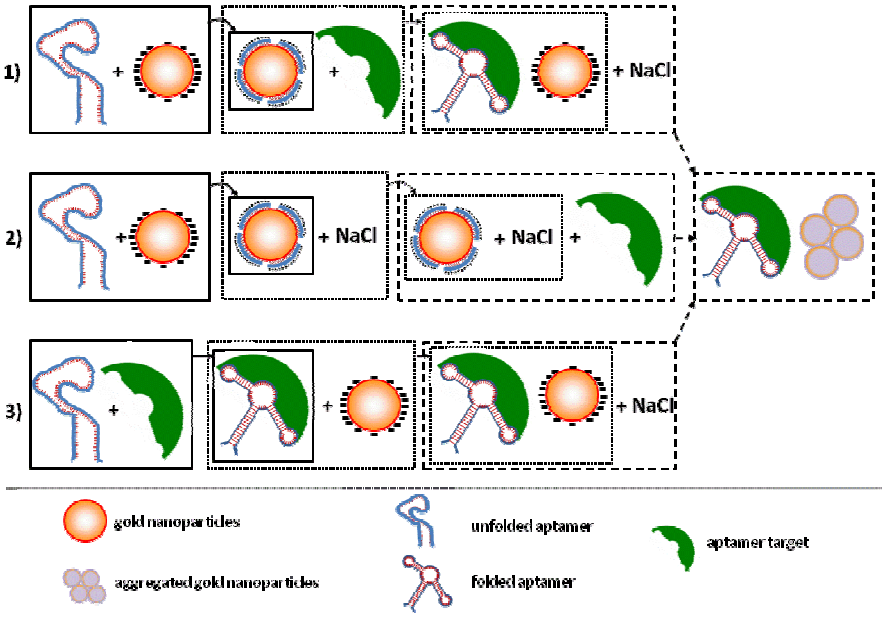


**Figure 4.4** – Schemes of the three variations of the designed experimental strategy for the detection of the vaccine *Inflexal V*, using unmodified AuNPs solutions and specific aptamers.

Considering those three variations of the experimental strategy design, 8 different samples (including 3 controls) were produced in triplicates as shown in Table 4.1 (pag. 90). Figure 4.5 summarizes the results obtained, in terms of the flocculation parameter variation.

As expected, challenging a solution of bare AuNPs with 100 mM of NaCl (***sample-1***) results in an increase of the flocculation parameter. Furthermore, this colorimetric signal is taken as the reference that indicates biorecognition and binding of the probes to targets in non-control samples.

Results from ***sample-2*** support to the assumption that, in the absence of the target,

aptamers unfold sufficiently to expose their positively charged hydrogen bases, which are then electrostatically attracted towards the negatively charged nanoparticles surfaces. Aptamers thus adsorb on to the nanoparticles, increasing the density of negative charges at their surfaces, consequently leading to an increased protection against salt-induced-aggregation and hence the lower variation of the flocculation parameter values.

In ***sample-3***, the vaccine was mixed with the AuNPs instead of the aptamers. The results obtained show that the assumption regarding the non-interaction of the vaccine with the colloidal nanoparticles has no experimental support: the vaccine seems to confer a protection against salt-induced-aggregation to the nanoparticles almost as high as that conferred by the aptamers (sample 2). One possible justification for this result is related to the presence of lecithin, in unknown quantities, on the excipients of the vaccine. Lecithin is a phospholipid known to have surfactant properties when in aqueous solution and, thus, when mixed with the aqueous solutions of colloidal AuNPs, may "surfactate" them increasing their resistance against salt-induced-aggregation.

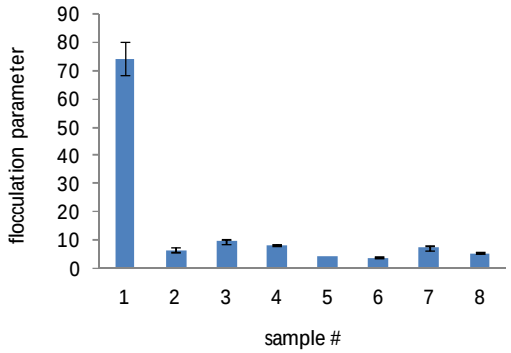


**Figure 4.5** – Results, in terms of flocculation parameter variation, of the assays performed for the detection of the vaccine *Inflexal V* with unmodified AuNPs and specific aptamers. The results are average over triplicates, and the error bars represent the calculated standard-deviation. All measurements were performed one hour upon introducing the last reagent. **Sample-1** (control-sample): unmodified bare AuNPs solution challenged with 100 mM of NaCl. **Sample-2** (control-sample): aptamer-to-nanoparticle ratio = 5 : 1. **Sample-3** (control-sample): haemagglutinin-to-nanoparticle ratio = 5 : 1. **Sample-4**: aptamer-to-haemagglutinin-to-nanoparticle ratio = 5 : 5 : 1. **Sample-5**: aptamer-to-haemagglutinin-to-nanoparticle ratio = 5 : 10 : 1. **Sample-6**: aptamer-to-haemagglutinin-to-nanoparticle ratio = 5 : 5 : 1. **Sample-7**: aptamer-to-haemagglutinin-to-nanoparticle ratio = 5 : 5 : 1. **Sample-8**: aptamer-to-haemagglutinin-to-nanoparticle ratio = 5 : 10 : 1.

It was expected that the flocculation parameter of ***samples-4*** and/or ***-5*** would reach values close to that of sample-1. Such result would have meant that, upon biorecognition towards the vaccine, aptamers would have "preferred" their folded structure, releasing from the nanoparticles surfaces and binding to their target (Wei et al, 2007). The unprotected AuNPs would then have aggregate due to the salt already in solution (Figure 4.4(1)), leading to the flocculation parameter

increase.

**Table 4.1** – Sequential steps for the preparation of each of the 8 samples, aiming the detection of the vaccine *Inflexal V*. In each sample, the reagents were introduced sequentially (top-to-bottom) in the borosilicate vials of a microplate.

| | | | |
|---|---|---|---|
| sample 1 | 45.0 µL of milli-Q water<br>5.0 µL of Tris HCl buffer<br>25.0 µL of stock AuNP<br>1 hour incubation<br>11.6 µL NaCl at 750 mM | sample 5 | 45.0 µL of milli-Q water<br>5.0 µL of aptamer<br>25.0 µL of stock AuNP<br>1 hour incubation<br>11.6 µL NaCl at 750 mM<br>1 hour incubation<br>12.0 µL of vaccine |
| sample 2 | 45.0 µL of milli-Q water<br>5.0 µL of aptamer<br>25.0 µL of stock AuNP<br>1 hour incubation<br>11.6 µL NaCl at 750 mM | sample 6 | 45.0 µL of milli-Q water<br>5.0 µL of aptamer<br>25.0 µL of stock AuNP<br>1 hour incubation<br>6.0 µL of vaccine<br>1 hour incubation<br>11.6 µL NaCl at 750 mM |
| sample 3 | 44.0 µL of milli-Q water<br>6.0 µL of vaccine<br>25.0 µL of stock AuNP<br>1 hour incubation<br>11.6 µL NaCl at 750 mM | sample 7 | 5.0 µL of aptamer<br>6.0 µL of vaccine<br>2 hours incubation<br>45.0 µL of milli-Q water<br>25.0 µL of stock AuNP<br>1 hour incubation<br>11.6 µL NaCl at 750 mM |
| sample 4 | 45.0 µL of milli-Q water<br>5.0 µL of aptamer<br>25.0 µL of stock AuNP<br>1 hour incubation<br>11.6 µL NaCl at 750 mM<br>1 hour incubation<br>6.0 µL of vaccine | sample 8 | 5.0 µL of aptamer<br>12.0 µL of vaccine<br>2 hours incubation<br>45.0 µL of milli-Q water<br>25.0 µL of stock AuNP<br>1 hour incubation<br>11.6 µL NaCl at 750 mM |

However, Figure 4.5 shows otherwise: both samples failed to show a biorecognition signal. Furthermore, in sample-5 the target concentration was 2-fold that of the aptamers, allowing to expect flocculation parameter values higher (or at least equal) than that of sample-4 where aptamer-to-target ratio is 1 : 1. A few reasons may be proposed for the obtained results: (a) the presence of the target is not “strong enough” to lead aptamers into releasing from the nanoparticles surfaces; (b) the aptamers actually released from the nanoparticles surfaces and bound on the target, but the lecithin from the vaccine excipients prevented AuNPs from

aggregating, as proposed above. Comparison between samples -4 and -5, shows a slightly smaller variation of the flocculation parameter of the later, suggesting towards the later hypothesis, since in sample-5 the quantity of target was increased (relative to that of sample-4) by increasing the volume of vaccine mixed in solution, thus increasing the quantity of lecithin and its surfactant effect.

Contrary to the procedure with samples -4 and -5, in ***sample-6***, the salt was mixed with the solution of aptamer-protected nanoparticles one hour upon incubating them with the vaccine. This allows discarding any negative effects that the salt may have over vaccine before being put in the presence of the aptamers. However, the results obtained are very similar to that of sample-5, i.e.: negligible aggregation. The proposed reasoning for these results is necessarily the same as that of samples -4 and -5. Furthermore, it is worth noting that the flocculation parameter values of sample-6 are closer to that of sample-5 (than that of sample-4), which can be related to the fact that when salt is mixed in solution the lecithin had already "more than enough time" to surround the nanoparticles, conferring them increased resistance against salt-induced-aggregation.

In ***sample-7*** and ***-8***, the aptamers were presented to the vaccine prior to mixing with the colloidal solution of AuNPs and then with the salt. Once again, the outcome result was the lack of aggregation signaling biorecognition. What's more, observing closely Figure 4.5, one can notice that sample-8 produces slightly lower variation of the flocculation parameter values than sample-7. Likewise to the discussion of the results of sample -4 and -5, this can be attributed to a higher volume of vaccine (and consequently lecithin) in the former than in the later.

The combination of results presented in Figure 4.5, suggest that the biomolecular recognition signal between aptamer and target might have been hindered by some of the vaccine excipients. Lecithin, particularly, seems be a good "interfering candidate", acting as surfactant and protecting the nanoparticles against salt-induced-aggregation when aptamers leave their surfaces to bind to the target.

Considering that possibility, a new set of experiments were designed and performed using purified haemagglutinins instead of the vaccine, this way avoiding the possibility of interference from the vaccine excipients.

### 4.3.2. Target: Haemagglutinins

A somewhat different biosensing strategy was developed, while using the same aptamers as before as well as the same stock of AuNPs, to detected purified haemagglutinins [from the virus strain: A/New Caledonia/20/99 virus (IVR-116)] instead of the *Inflexal V* vaccine. The results from the previous subsection suggested the possibility that targets could be unable to induce releasing of the aptamers from the AuNPs surfaces. To avoid that possibility, here, aptamers were always incubated with target prior to mixing with the solutions of AuNPs.

Thus, for the second sensing approach, two aptamer-haemagglutinin solutions were prepared: in ***Solution-1*** aptamers were incubated (2 hours, in dark, at room temperature) with haemagglutinins at a 1 : 1 ratio, and in ***Solution-2*** the ratio was 1 : 2. Experimental samples were then prepared mixing AuNPs with both of the aptamer-haemagglutinin solutions, at four different aptamer-to-nanoparticle ratios: 2.5:1, 3.75:1, 5:1 and 10:1 (corresponding to 0.5, 0.75, 1 and 2 times the estimated coverage of the nanoparticles with aptamers) and incubated for 1 hour. The samples were then challenged with 100 mM of NaCl and the optical absorption spectra were acquired 1 hour after.

The results obtained are summarized in Figure 4.6. There, the first column shows a high variation of the flocculation parameter as a result of introducing salt in a solution of bare AuNPs. Then, there are four sets of four columns where within each set:

(1) first columns refer to samples containing aptamers, AuNPs and salt;
(2) second columns refer to samples containing haemagglutinins, AuNPs and salt;
(3) third columns refer to samples containing solution-1, AuNPs and salt;
(4) fourth columns refer to samples containing the solution-2, AuNPs and salt;.

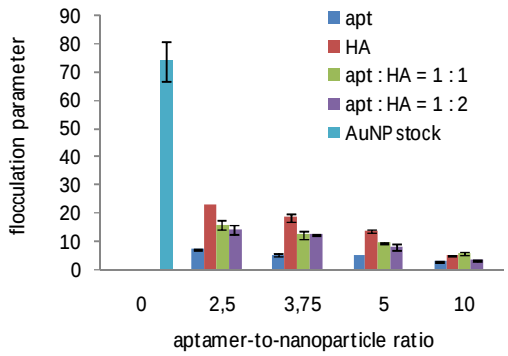


**Figure 4.6** - Results, in terms of flocculation parameter variation, of the assays performed for the detection of the purified haemagglutinins with unmodified AuNPs and specific aptamers. The results are average over triplicates, and the error bars represent the calculated standard-deviation. All measurements were performed one hour upon introducing the last reagent (HA = haemagglutinin).

As expected in light of the results the previous chapter, the results show that aptamers protect colloidal nanoparticles against salt induced aggregation (dark blue columns), with an increasing degree of protection accompanying the increasing of the aptamers-to-nanoparticle ratio.

Surprisingly, however, the AuNPs samples containing haemagglutinins reveal also a protection against salt induced aggregation effect (although not as high as that produced by the aptamers). Additionally, that protection effect also increases with increasing concentration of haemagglutinin. The reasoning for this is unclear. It is hypothesized, without proofing, that the existence of thiol residues exposed on the haemagglutinin structure could lead this glycoprotein into binding non-specifically on the nanoparticles surfaces preventing aggregation.

Thus, samples containing purified haemagglutinins instead of the vaccine also failed in producing biorecognition signals. In fact, **Figure 4.6** shows that the degree of aggregation, induced by the salt in samples containing solutions -1 and -2, is lower than that in solutions containing haemagglutinins only. These results suggest that either: (1) the target of the aptamers within the *Inflexal V* vaccine are not the haemagglutinins (or at least the strain tested) and thus the unbound aptamers exert their protection effect on the AuNPs; or (2) biorecognition occurs but there is still some unaccounted factor preventing aggregation from occurring upon introduction of the salt.

## 4.4. Conclusions

This chapter reports the assays performed with the aim of establishing a method to colorimetrically detect the presence of the influenza virus in solution, using specific aptamers and colloids of non-functionalized AuNPs. However, due to non-fully-determined reasons, all of the detection routes proposed failed to produce a biorecognition signal.

The company that supplied the aptamers had previously proven their biorecognition capabilities towards the *Inflexal V* vaccine. Thus, specificity of probe towards target should be excluded as an issue to the lack of biorecognition signal. The negative results may be attributed to non-specific interactions between the excipients of the vaccine (or the virosomes themselves) towards the AuNPs, with the former preventing the aggregation of the later (thus hindering the appearance of the biorecognition signal).

Subsequently, it was hypothesized that using a purified of haemagglutinins as targets instead of the vaccine might enable obtaining the biorecognition signal. However, this strategy also failed to produce a biorecognition signal. In fact, it was observed that the solution of purified haemagglutinins itself may hinder the appearance of biorecognition signal given its observed non-specific interaction with the colloidal AuNPs, which prevents them from aggregating when challenged with the salt.

# 5. Development of Gold Nanoparticles Based Colorimetric Immunosensing

The surface plasmon resonance (SPR) coupling of gold nanoparticles (AuNPs) has been explored as a generated signal in many biosensing applications. Particularly, the controlled aggregation of functionalized AuNPs, by means of specific biomolecular recognition, may be used in sensing applications such as the development of colorimetric assays.

In this chapter, the key conceptual steps and sensing performance involved in development of colorimetric immunosensors with AuNPs were addressed by evaluating absorption spectroscopy data, in light of theoretical and experimental background. The streptavidin–biotin pair was used as "ideal" target-probe pair to demonstrate the usefulness of AuNPs colloids as colorimetric signal transducing agents to detect proteinaceous analytes in solution.

## 5.1. Introduction

Given its very well known specificity and affinity (Encarnação, 2007), the streptavidin-biotin pair may be used as model for setting up grounds for new biosensing applications, particularly on the development of novel immunosensing assays.

Here, a method for functionalization of AuNPs with biotin molecules (probes) in a one-pot procedure is described. The controlled aggregation of these biotin-functionalized AuNPs is then promoted by means of biomolecular recognition upon interaction with streptavidin molecules (targets) at different concentrations.

The AuNPs degree of aggregation is evaluated at all stages through optical absorption spectroscopy data, and particularly by monitoring the flocculation parameter values. Flocculation parameter data is further used to evaluate the mechanisms of aggregation in light of Smoluchowski aggregation kinetics based-equations.

## 5.2. Materials and Methods

### 5.2.1. Reagents

Colloidal AuNPs with 9.6 nm average diameter were obtained from British Biocell International, at concentration of approximately 9.5 nM.

Lyophilized streptavidin was purchased from Roche and diluted to final concentrations of 0.577 to 5.77 µM in milli-Q water containing 0.1% of sodium azide. (+)-Biotinyl-3,6-dioxaoctanediamine was acquired lyophilized from Pierce and diluted to a concentration of 800 µM in milli-Q water. Bovine Serum Albumin was acquired from Sigma, and prepared to a final concentration of 7.46 µM in milli-Q water.

Di-sodium hydrogen phosphate, Sodium dihydrogen phosphate monohydrate, Polyoxyethylene (20) sorbitan monolaurate (Tween-20), Magnesium chloride hexahydrate were acquired from Merck. Sodium phosphate buffer was prepared in milli-Q water to a concentration of 100 mM, at pH 8.2, and Tween-20 was mixed to a final concentration of 1.5 mM. A solution of magnesium chloride was prepared at 2.5 M in milli-Q water.

Dithiobis-succinimydil undecanoate (DSU) was acquired from Dojindo and solubilized in dimethylformamide (DMF) to obtain a 10 mM DSU solution. Then, 100 µM aliquots were prepared in absolute ethanol (from Panreac) and used without further purification.

### 5.2.2. Instrumentation

Optical absorption spectroscopy measurements were performed in a Shimadzu UV-1700 spectrophotomer.

## 5.2.3. Experimental Methods

### 5.2.3.1. Functionalization of Gold Nanoparticles

Several strategies have been reported to functionalize colloidal AuNPs surfaces, most of them relying on the formation of self-assembled-monolayers of ligands that allow the attachment of bio-molecules (Aili *et al.*, 2006; Lévy *et al.*, 2004; Nuopponen and Tenhu, 2007). The self-assembled-monolayers based on thiol chemistry are considered of particular interest for this purpose, given their high affinity towards gold surfaces and the diversity of functional groups that can be attached through them (Love *et al.*, 2005). Nevertheless, the modification of bare AuNPs surfaces through the chemisorption of alkanethiol molecules may lead to irreversible aggregation of the nanoparticles if the proper steps are not taken to avoid it (Figure 5.1, bottom route) (Love *et al.*, 2005; Weisbecker *et al.*, 1996; Aslan *et al.*, 2002).

Here, the chemisorption of alkanethiol based self-assembled-monolayers was promoted on the AuNPs surfaces while simultaneously, in a one-pot procedure, bio-activating the functional groups of the alkanethiol linkers with biotin molecules. Furthermore, the "aggregation-during-functionalization issue" was avoided by previously stabilizing sterically the AuNPs with a non-ionic surfactant (Figure 5.1, top route), as previously reported (Aslan and Pérez-Luna, 2002).

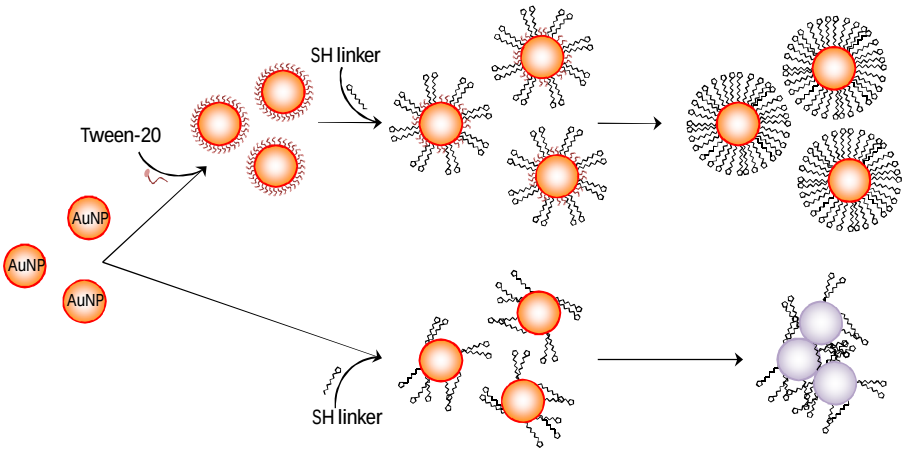


**Figure 5.1** – In the absence of a stabilizing agent (bottom route), colloidal AuNPs undergo aggregation during the chemisorption of the alkanethiol linkers. This has been attributed to the hydrophobic character acquired by the gold surfaces during self-assembled-monolayer formation due to the exposed methylene chains of the linkers (Aslan and Pérez-Luna, 2002). On the other hand, if a surfactant monolayer is physisorbed on the nanoparticles surfaces prior to the introduction of the alkanethiols in solution (upper route), steric repulsion keeps the nanoparticles from aggregating during the chemisorption of the alkanethiols. When the full linker monolayer is formed, aggregation no longer occurs and the surfactant is no longer needed. (Adapted from: Aslan and Pérez-Luna, 2002).

Specifically, modification of the bare AuNPs surfaces with biotin was performed as follows (Figure 5.2):

Step 1: 163 µL of biotin and 1 mL of bare AuNPs were diluted in 4 mL of a phosphate buffer (containing 1.5 mM of Tween-20). This solution, containing approximately $1.4x10^4$ biotin molecules per AuNP, was briefly vortexed and then incubated for one hour (resting in dark, at room temperature).

Step 2: 65 µL of DSU were introduced in the nanoparticles-biotin solution ($[AuNP]_f \approx$ 1.8 nM, $[biotin]_f \approx$ 24.9 µM, $[DSU]_f \approx$ 1.2 µM). This reactional mixture, containing approximately $1.4x10^3$ amine-reactive alkanethiol molecules per AuNP [(corresponding to the estimated maximum alkanethiol coverage (Tominaga *et al.*, 2004)] and approximately 10 biotin molecules per amine-reactive site, was then incubated overnight under moderate agitation (at room temperature and in dark)

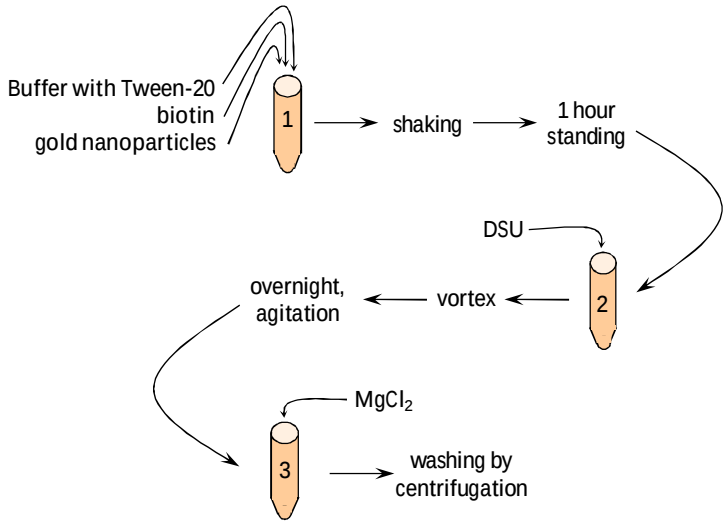


**Figure 5.2** – Scheme of the procedure utilized to functionalize 9.6 nm AuNPs with biotin molecules. Step 1: physisorption of a surfactant monolayer at the nanoparticles surfaces; Step 2: chemisorption of the self-assembled-monolayer of linkers with the probe molecules; Step 3: washing by centrifugation to remove unbound linkers and biotin molecules.

Step 3: $MgCl_2$ was introduced in solution to a final concentration of 30 mM. Samples were then centrifuged at least 3 times at 1000 to 3000 g during 1 to 3 minutes each time. After each centrifugation the clear supernatant was discarded and the pellet ressuspended in 4 mL of phosphate buffer (without Tween-20) and vigorously vortexed.

### 5.2.3.2. Streptavidin Induced Aggregation

Streptavidin is a homotetrameric molecule folded in such a way that the four biotin binding sites are grouped in pairs at opposite faces of the protein. This molecular geometry enables streptavidin induce the inter-connection of biotin-functionalized AuNPs, leading to aggregation (Figure 5.3).

Here, a study was developed to investigate the rate and degree of aggregation of biotinylated AuNPs solutions induced by different quantities of streptavidin. Aggregating samples were prepared (in triplicates) by introducing different amounts of streptavidin on biotinylated AuNPs solutions (prepared as described in the previous subsection and set to a concentration of 1.8 nM), rendering samples with streptavidin-to-nanoparticle ratios between 1:4 and 32:1 ($0.5 < [\text{streptavidin}]_f < 57.6$ nM, approximately). After introducing the streptavidin molecules, samples were slightly shaken and then left resting in dark at all times except before spectra acquisition. Before the absorption readings, samples were slightly shaken and then pipetted from the reaction vial to the quartz cell.

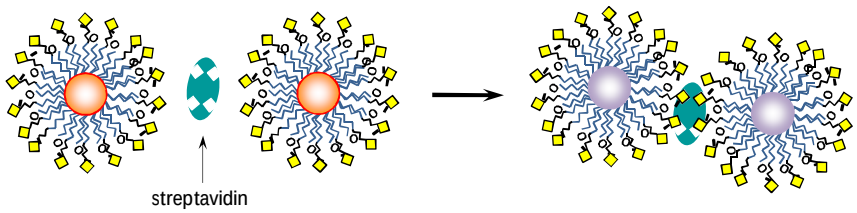


**Figure 5.3** – Scheme representing the aggregation of two biotinylated nanoparticles by means of biomolecular recognition of a streptavidin molecule.

As before, the flocculation parameter was used to infer on the AuNPs degree of aggregation.

## 5.3. Results and Discussion

### 5.3.1. Gold Nanoparticles Biotinylation

Figure 5.4 presents the typical optical absorption spectra at each step of the AuNPs biotin-functionalization procedure.

The SPR of stock AuNPs appears in the expected wavelength region, with a peak at 519

nm (red-dashed spectrum). One hour upon diluting the AuNPs in the phosphate buffer containing Tween-20 and biotin molecules [during which the surfactant molecules physisorb on the nanoparticles surfaces (Aslan *et al.*, 2004)] a shift of the resonance peak to 527 nm was observed (purple spectrum), as well as a slight increase of the absorbance intensity and broadness of the spectrum (Figure 5.5).

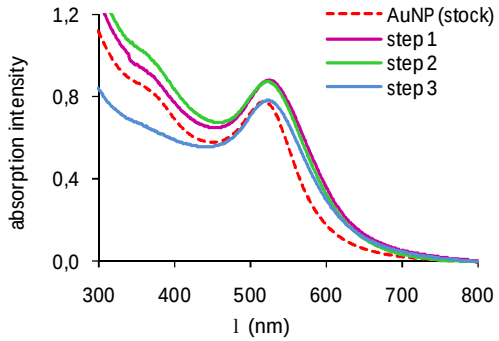


**Figure 5.4** – Typical optical absorption spectra at each step of the AuNPs biotinylation procedure. Refer to subsection 5.2.3.1 for detail description of the procedures at each step.

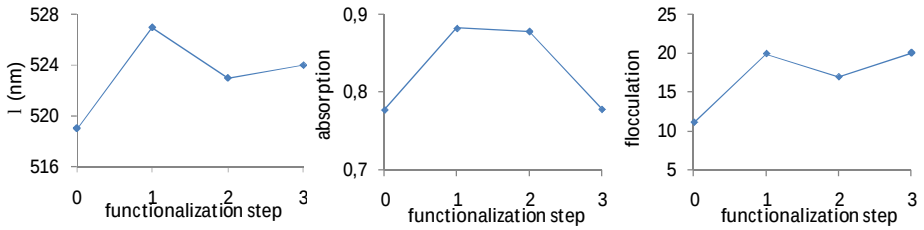


**Figure 5.5** – Variation of the optical parameters during the AuNPs functionalization procedure. *Left-hand side plot*: variation of the SPR peak position; *Middle plot*: absorption intensity variation at the SPR peak (the dilution factors were accounted for); *Right-hand side plot*: flocculation parameter variation. The lines that connect the marks are an aid to help guiding the eye

These combined effects have been correlated to alterations of the medium surrounding the nanoparticles and, particularly, to changes on its dielectric characteristics. On the present case, these changes can be related both to the adsorption of the surfactant molecules on the nanoparticles surfaces and to the salts from phosphate buffer (Nath *et al.*, 2002; Schmitt *et al.*, 1999; Mulvaney, 2001; Eck and Helm, 2001; Lakowicz, 2005).

DSU, an alkanethiol ligand molecule commonly used to activate flat gold surfaces with amine-reactive sites (Encarnação *et al.*, 2007), was mixed into the reaction mixture aiming obtaining full nanoparticle coverage with alkanethiol molecules (Tominaga *et al*, 2004). Then, three simultaneous processes begin (Figure 5.6):

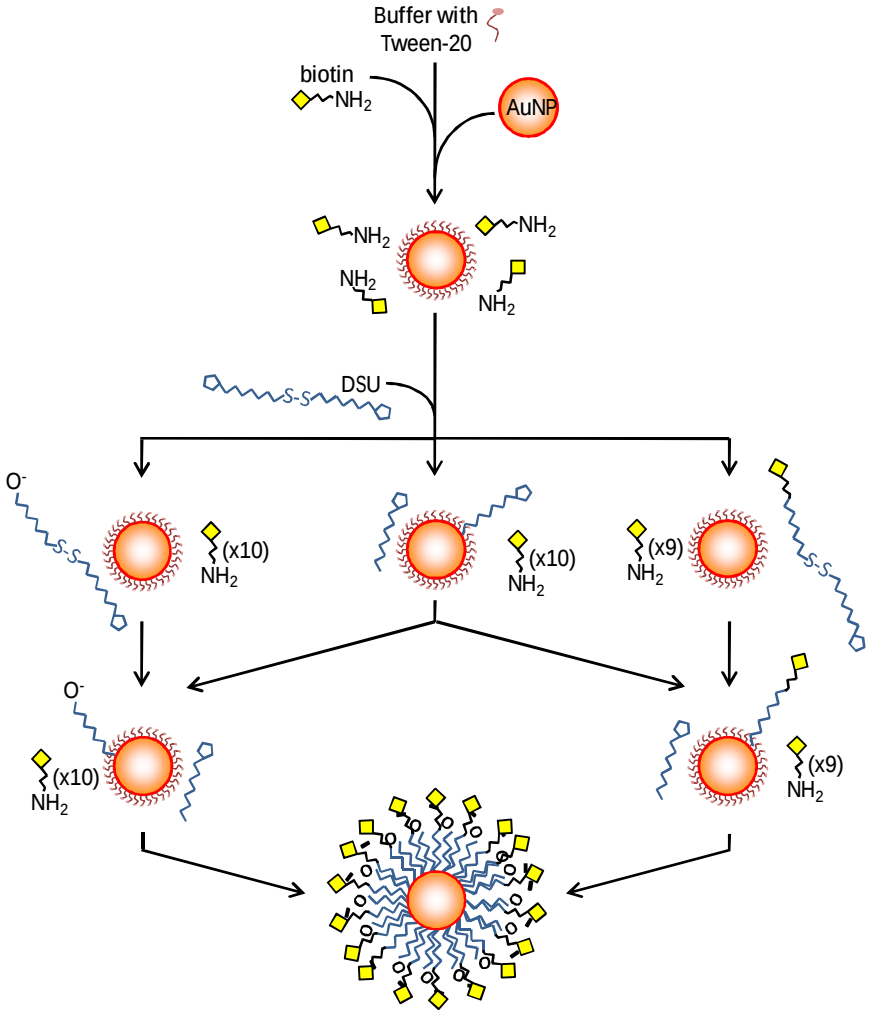


**Figure 5.6** – Possible (simultaneous) routes of reaction during the biotin functionalization procedure. Upon introduction of the DSU in solution, it may: undergo hydrolyzation of the succinimidyl endgroups (left-hand route), covalently bind to the biotin molecules (through their amine termini) at the succinimidyl endgroups (right-hand route) and/or "just" dissociate the disulfide bonds (middle route). In the cases of initial hydrolysis or initial covalent binding to biotin, the disulfide bond will then dissociate and contribute to the formation of the self-assembled-monolayer. In the case of initial disulfide bond dissociation, the succinimidyl ester groups will then undergo hydrolysis and/or covalently bind to the biotin. In all cases, it is expected that each nanoparticle end up covered with a mixed monolayer of biotin-terminated and hydroxyl-terminated methylene chains.

(1) dissociation of the disulfide bonds of the DSU molecules and chemisorption of the thiolates onto the gold surfaces, forming the self-assembled-monolayers (Grönbeck *et al.*, 2000) (middle-route in Figure 5.6);

(2) crosslinking of DSU with biotin upon reaction of the ester-terminal groups of DSU with the terminal amine groups of the (+)-biotinyl-3,6-dioxaoctanediamine (right-hand side route in Figure 5.7 and Figure 5.6); and

(3) hydrolyzation of the excess DSU ester-terminal groups which didn't crosslink with biotin (Grubor *et al.*, 2004; Vaidya *et al.*, 2001) (left-hand side route in Figure 5.7 and Figure 5.6).

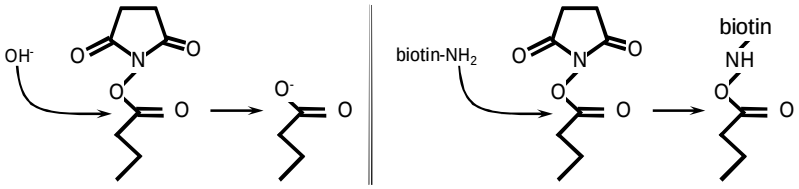


**Figure 5.7** – Alternative (competitive) routes of reaction of the linker terminal succinimidyl ester groups in a basic buffer. *Left-hand side*: hydrolysis; *Right-hand side*: covalent binding to primary amines. Adapted from Grubor *et al.*, 2004.

It is noteworthy that the presence of Tween-20 molecules physisorbed on the nanoparticles surfaces is expected not to hinder the chemisorption of the alkanethiol chains, since the interaction of the former with the gold surfaces is much weaker than the interaction of the later. Consequently the surfactant molecules should be easily displaced by the chemisorbing alkanethiol molecules.

Furthermore, there is no reason for processes (2) and (3) not occurring (simultaneously) both on unbound DSU molecules and on those already forming the self-assembled-monolayer on the AuNPs surfaces [despite the different rates at which each reaction takes place (Grubor *et al.*, 2004)]. However, given that the binding of proteins through their amine tails is a more efficient process than the hydrolysis of succinimidyl endgroups [in basic buffers (Grubor *et al.*, 2004)] and that the ratio of biotin to amine-reactive-sites was intentionally set to an excess of 10 : 1, it is expected that a greater number of alkanethiol chains end up with a biotin bound to their termini instead of hydroxyl groups. This functionalization process results on the formation of a mixed self-assembled-monolayer on the surface of each AuNP containing biotin- and hydroxyl-terminated alkanethiols, which is experimentally demonstrated by the "shifting back" of the SPR peak to 523 nm (green spectrum in Figure 5.4). This shifting to lower wavelengths suggests hindrance of the optical resonance coupling, mostly due to the increased interparticle repulsion provided by the presence of negatively charged hydroxyl groups at the gold surfaces, as well as to the self-assembled-monolayer packing density limiting the disturbing influence of the buffer's ionic strength over the colloidal stability. The slight spectral differences detected between the unmodified- and biotinylated- AuNPs may be attributed to this self-assembled-monolayer changing the refractive index at the nanoparticles surfaces (Weisbecker *et al.*, 1996; Maya *et al.*, 1997; Lakowicz, 2005).

Washing of the unbound molecules (biotin and DSU) from the biotinylated-nanoparticles solutions was greatly facilitated by the introduction of $MgCl_2$ (to final concentration of 30 mM). This salt induced the rapid precipitation of the nanoparticles to the bottom of the vial because it greatly reduced (or eliminated) the charges at the surfaces of the functionalized nanoparticles.

However, adding $MgCl_2$ did not produced aggregation, as observed by the reddish color of the precipitates. Samples were then centrifuged at least 3 times at 1000 to 3000 g during 1 to 3 minutes each time. After each centrifugation the clear supernatant was discarded and the pellet was ressuspended in 4 mL of phosphate buffer (without Tween-20). Each time, the ressuspended solution was vigorously vortexed and then left resting for at least one hour to evaluate its colloidal stability. After 3 or 4 centrifugation/washing steps, during which $MgCl_2$ and unbound biotin and DSU molecules were discarded on the supernatant, the AuNPs no longer precipitate, meaning that the concentration of $MgCl_2$ in the solution became insignificant. The blue spectrum in Figure 5.4, acquired upon completion of the washing procedure, shows that the absorption profile of the sample was kept unaltered, with the slight reduction of the absorption intensity being attributed to the loss of some amount of nanoparticles on the discarding of the supernatants.

Noteworthy, is the key part played by $MgCl_2$ in the centrifugation process. In fact, it was observed that, when this salt was not mixed in the solutions of the functionalized nanoparticles prior to washing, much higher speeds and centrifugation times were needed to induce precipitation (higher than, for instance, with bare nanoparticles), which typically leads to irreversible aggregation (Figure 5.8). It was, thus, hypothesized that the functionalization procedure developed here places a high-enough number of hydroxyl groups on the AuNPs surfaces, producing an electrostatic repulsion effect such that it prevents their precipitation to the bottom of the vial using lower speeds and centrifugation times (Figure 5.9). Hence, introducing the high ionic strength salt shields those extra negative charges at the nanoparticles surfaces, reducing their inter-repulsion effect, consequently, allowing to greatly reduce the centrifugation speeds and times while keeping the effectiveness of the washing procedure.

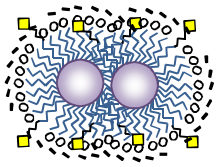

**Figure 5.8** – Irreversible fusion of the gold cores and/or merging of the methylene chains caused by high centrifugation speeds and times.

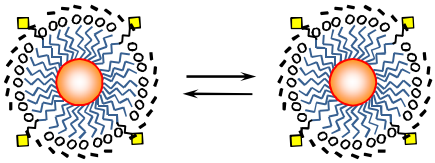

**Figure 5.9** – High-enough number of hydroxyl groups, at the AuNPs surfaces, produces an electrostatic repulsion effect strong enough to prevent the nanoparticles from precipitating out of solution with lower speeds and centrifugation times

Colloidal solutions of AuNPs modified by the procedure described above were able to remain stable for several weeks.

### 5.3.2. Streptavidin Induced Aggregation

Figure 5.10 shows the flocculation parameter variation after incubating biotinylated nanoparticles with different relative amounts of streptavidin. As shown, the signal of maximum aggregation was obtained when streptavidin was mixed with biotinylated-nanoparticles at 5:1 ratios. Furthermore, these samples lead to the highest wavelength shifts (the SPR peak reaching 549 nm → $\Delta\lambda$ = 24 nm) and absorption intensity decreases at the resonance peak (Figure 5.11). These are clear evidences of significant aggregation through crosslinking of the AuNPs by means of streptavidin-biotin recognition.

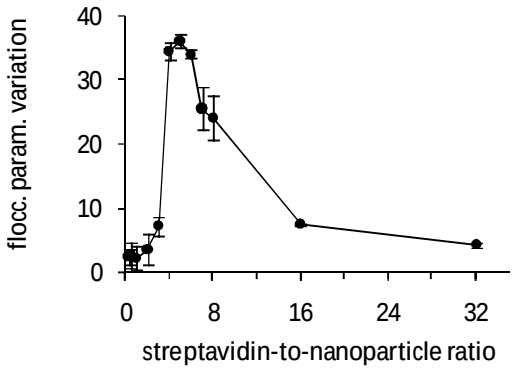


**Figure 5.10 –** Flocculation parameter upon incubating biotinylated nanoparticles with different relative amounts of streptavidin for approximately 400 minutes (close to 7 hours). The plotted values were averaged over triplicates, and are relative to the flocculation parameter values of the "just" biotinylated AuNPs. The line that connects the marks is an aid to help guiding the eye.

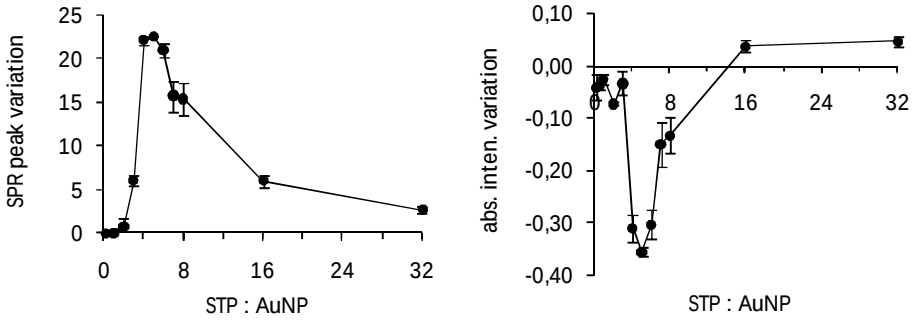


**Figure 5.11** – *Left-hand side*: SPR peak position variation upon incubating biotinylated nanoparticles with different relative amounts of streptavidin for approximately 400 minutes; *Right-hand side*: corresponding variation of the absorption intensity at the resonance peak. The lines that connect the marks are an aid to help guiding the eye.

Additionally, preparations containing streptavidin-to-nanoparticle mixtures at ratios between 4:1 and 6:1 incubated overnight at room temperature, invariably lost all color (becoming transparent) with black aggregates sedimented at the bottom of the test tubes. Absorption spectra taken at this stage show a complete absence of the characteristic SPR peak (refer to Figure 5.12), and neither vortexing nor ultrasonicating produced any detectable spectral changes on these samples, meaning that nanoparticles were irreversibly aggregated.

Figure 5.10 shows also that for streptavidin-to-nanoparticle ratios lower then 4:1, the changes associated with aggregation were considerably less pronounced, as streptavidin shortage limits the degree of aggregation (Aslan *et al.*, 2004).

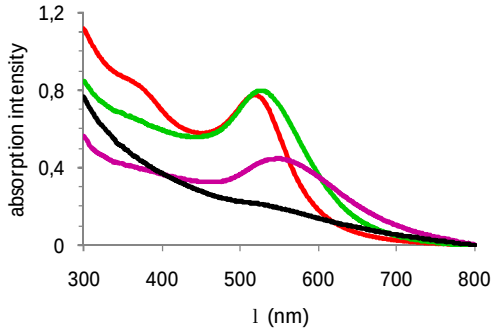


**Figure 5.12** – *Red spectrum*: stock colloidal AuNPs, as supplied. *Green spectrum*: biotin-functionalized AuNPs. *Purple spectrum*: acquired 7 hours upon mixing streptavidin to the biotinylated nanoparticles, at a streptavidin-to-nanoparticle ratio of 5:1. *Black spectrum*: acquired approximately 24 hours upon mixing the streptavidin and left resting overnight.

Similarly, smaller variations of SPR peak position, adsorption intensity and flocculation parameter were also observed for streptavidin-to-nanoparticle ratios higher than 6:1. This result can be explained considering both the excess of streptavidin molecules, as compared to the

amount of nanoparticles, and the differences in the diffusion coefficients of free streptavidin molecules and biotinylated-nanoparticles. In fact, the Stokes-Einstein equation estimates the diffusion coefficient of streptavidin and biotinylated-nanoparticles as $D_{STP} = 9.815\times10^{-7}$ $cm^2s^{-1}$ and $D_{AuNP} = 2.788\times10^{-7}$ $cm^2s^{-1}$, respectively, assuming spherical conformation of the streptavidin ($r_{STP}$ = 2.5 nm) and that the radius of biotinylated-nanoparticles ($r_{AuNP}$= 8.8 nm) equals the radii of the nanoparticles summed to the length of DSU and of the (+)-biotinyl-3,6-dioxaoctanediamine (Porter *et al.*, 1987). When streptavidin binds to the modified nanoparticles, the theoretical diffusivity of the nanoparticle is further reduced to $D_{STP\text{-}AuNP} = 1.778\times10\text{-}7$ $cm^2s^{-1}$. These diffusivities indicate that streptavidin diffuses at least 3.52 times faster than the modified nanoparticles and therefore, under experimental conditions where streptavidin is largely in excess, it is more likely that binding events to modified nanoparticles will occur with free streptavidin rather than with streptavidin molecules already bound to the immobilized biotin molecules (resulting in nanoparticles crosslinking through streptavidin). Consequently, when in large excess, free streptavidin will quickly block available biotin sites at the nanoparticles surfaces (Figure 5.13), thus limiting the possibility of nanoparticle aggregation through streptavidin inter-connection and crosslinking (Connolly *et al.*, 2001).

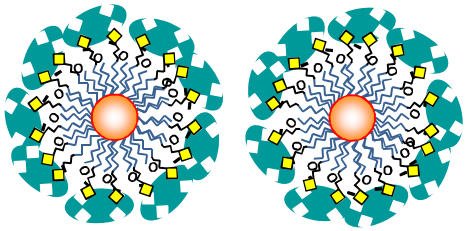

**Figure 5.13** – Introducing large amounts of streptavidin quickly blocks most or all the available biotin sites on the AuNPs surfaces at initial stages, preventing aggregation.

According to Aslan, “in order for the cross-linking to occur, the ratio of available biotin groups to binding sites must not be significantly different from 1, as the resultant shortage/excess will cause the aggregation to stop” (Aslan *et al.*, 2004). Based on that assumption and on the results presented in Figure 5.10 showing maximum aggregation signal for samples with streptavidin-to-nanoparticle ratios between 4:1 and 6:1, it can be inferred that the nanoparticles functionalization procedure performed here resulted in a biotin coverage between 16 and 24 molecules per nanoparticle. This estimation is consistent with the following observations:

(a) for streptavidin-to-nanoparticle ratios equal or above 16:1 the measured flocculation parameter variation is either very small or negligible (and may be related only the

different dielectric medium at the nanoparticles surfaces imparted by the presence of streptavidin molecules); and

(b) the extra stability against precipitation by centrifugation demonstrated by the functionalized nanoparticles, was most likely due to a very high ratio of hydrolyzed- to biotin-terminated linkers at the gold surfaces, producing an elevated inter-repulsion effect (contrary to what would happen if the surfaces were covered mostly with biotin molecules).

After a period of approximately 7 hours, during which several spectra were acquired, the aggregating samples were left resting undisturbed overnight (in dark, at room temperature). Then, approximately 24 hours upon introducing the streptavidin molecules and after vigorous vortexing, a spectrum was acquired from each sample to evaluate the degree of aggregation upon prolonged resting. Table 5.1 shows that, sometimes, the flocculation parameter increased considerably overnight, particularly in samples with streptavidin-to-nanoparticle ratios between 4:1 and 8:1.

**Table 5.1** – Comparison of the averaged flocculation parameter measured 7 and 24 hours upon introducing the streptavidin (during the last 17 hours the samples were left standing in dark, at room temperature).

| Sample ratio | Flocculation parameter variation | | | | | |
|---|---|---|---|---|---|---|
| | 7 hours | | | 24 hours | | |
| 1 : 4 | 2.5 | ± | 1.1 | 2.2 | ± | 0.4 |
| 1 : 2 | 2.7 | ± | 1.9 | 2.3 | ± | 0.5 |
| 1 : 1 | 2.3 | ± | 1.9 | 2.5 | ± | 1.2 |
| 2 : 1 | 3.7 | ± | 2.5 | 8.7 | ± | 1.1 |
| 3 : 1 | 7.4 | ± | 2.5 | 11.6 | ± | 1.5 |
| 4 : 1 | 34.6 | ± | 1.4 | 43.9 | ± | 3.6 |
| 5 : 1 | 36.2 | ± | 1.0 | 44.9 | ± | 5.0 |
| 6 : 1 | 34.2 | ± | 0.6 | 43.5 | ± | 0.3 |
| 7 : 1 | 25.7 | ± | 3.4 | 33.3 | ± | 3.0 |
| 8 : 1 | 24.2 | ± | 3.6 | 39.0 | ± | 7.8 |
| 16 : 1 | 7.6 | ± | 0.1 | 11.6 | ± | 1.0 |
| 32 : 1 | 4.4 | ± | 0.4 | 4.2 | ± | 0.2 |

Nevertheless, these results are considered only from the qualitative point of view and not quantitatively, because it is not possible to quantify the weight of each of the following effects affecting the flocculation parameter values: (1) in the two periods of time, samples underwent different treatments (first being periodically shaken, and then left resting for a long period) and; (2) at the time of the final reading, all of those samples presented large quantities of aggregates

at the bottom of the reaction vial, that rapidly precipitated to the bottom of the quartz cell before measurements could take place, even after the vigorous vortexing. The precipitation out of suspension of the larger aggregates leads to an increase of the flocculation parameter due to the subsequent absorption intensity decrease, but may also lead to a decrease the flocculation parameter because there are lesser aggregates absorbing at the higher wavelengths.

### 5.3.3. Kinetics of Streptavidin Induced Aggregation

#### 5.3.3.1. Aggregation Kinetics Theory

Considering that aggregation of AuNPs leads to the appearance of resonances at higher wavelengths and that the flocculation parameter results from the integration of the absorption spectrum on that optical band region, it is reasonable to assume that the magnitude of the flocculation parameter closely reflects the degree of aggregation (Aslan et al., 2004), at least at the initial aggregations stages when the aggregates are still in suspension. The mechanisms of streptavidin induced aggregation were thus investigated considering that the flocculation parameter is somehow proportional to the degree of aggregation.

In what follows, it is further assumed that most or all of the streptavidin molecules bind very quickly to the biotins on the nanoparticles surfaces, before any meaningful crosslinking between different nanoparticles through streptavidin comes into play (leading to aggregation). Subsequently, the aggregating system should be considered as being constituted by: (1) the aqueous medium (phosphate buffer) and (2) the aggregant particles, which are composed by biotinylated nanoparticles partially covered by streptavidin molecules (with un-reacted biotins attached to the nanoparticles surfaces yet available for crosslinking with streptavidin molecules attached to the surface of other nanoparticles). This allows applying the general ideas from non-specific aggregation research in which, when an aggregant is added to a stable colloidal dispersion it causes the monomer to diffuse, collide and bind irreversibly forming clusters (Lynch *et al.*, 1996).

A large number of studies have been directed towards the understanding of the mechanisms behind the aggregation of colloidal nanoparticles (Lattuada *et al.*, 2006; Ghosh and Pal, 2007). According to the theory (Lynch *et al.*, 1996), two relationships are necessary to describe the aggregation process quantitatively: (1) a correlation between the number of monomers in the aggregate, **n**, and its size; and (2) a kinetic model describing the distribution of

the aggregates as a function of time. From the study proposed by Lynch and coworkers, small aggregates with diameters less than 12 times the nanoparticle diameter may be treated as globular structures, whose aggregated radius ($\mathbf{a_n}$) is related to the monomer radius ($\mathbf{a_1}$) by:

$$a_n = \left(\frac{n}{1-\varepsilon_g}\right)^{1/3} \quad \text{Equation 5.1}$$

where $\boldsymbol{\varepsilon_g}$ is the volume fraction of the solvent in the aggregate and remains constant as the aggregate grows.

On the other hand, larger aggregates exhibit self-similarity across many scales (they are of fractal nature) with the radius obeying to the relation:

$$a_n \propto n^{1/d_f} \quad \text{Equation 5.2}$$

where the fractal dimension ($\mathbf{d_f}$) is usually a non-integer between 1 and 3, that relates the mass of a fractal object to its characteristic length ($Mass \propto Lenght^{d_f}$).

In studies of non-specific aggregation, two distinct kinetic regimes have been observed: diffusion-limited aggregation and reaction-limited aggregation (Lynch *et al.*, 1996). At high aggregant concentrations, every collision results in immediate bond formation (i.e., the sticking probability ≈ 1), leading to diffusion-limited aggregation. The large aggregates formed under this aggregation regime have fractal dimensions between 1.7 and 1.9 and a mean hydrodynamic radius, $\langle \boldsymbol{a_n} \rangle$, that increases with time according to:

$$\langle a_n \rangle \propto t^{1/d_f} \quad \text{Equation 5.3}$$

As for low aggregant concentrations, the sticking probability is near zero, requiring large number of collisions for each bond formation, which leads to a reaction-limited aggregation. Here, large aggregates result more compact with a fractal dimension of 2.1 and, $\langle \boldsymbol{a_n} \rangle$ increases with time according to:

$$\langle a_n \rangle \propto e^{\alpha t}$$ Equation 5.4

These relations follow from Smoluchowsky kinetics in which the rate of **n-*mer*** formation and consumption, assuming only irreversible reactions, is given by:

$$\frac{dX_n}{dt} = \frac{1}{2}\sum_{n'=1}^{n-1} a_{(n-n')n'} X_{n-n'} X_{n'} - \sum_{n'=1}^{\infty} a_{nn'} X_n X_{n'}$$ Equation 5.5

where $\mathbf{X_n}$ is the mole fraction of clusters containing **n** monomers, and $\mathbf{a_{nn'}}$ is the reaction kernel. If $\mathbf{a_{nn'} = A}$, known as the *constant kernel*, effective collisions are equally likely between two aggregates regardless of their size, corresponding to the diffusion-limited aggregation model. The **n-*mer*** distribution is given by:

$$X_n^{const} = (1-b)^2_{const} b_{const}^{n-1}$$ Equation 5.6

where $\mathbf{b_{const}}$ is the extent of aggregation ranging from 0 to 1 with time. Physically, **b** represents the average number of bonds per nanoparticle if only one bond between two particles is counted and cyclic structures are not allowed. $\mathbf{b_{const}}$ varies with **t** as:

$$b_{const} = \frac{t/\tau_{const}}{1 + t/\tau_{const}}$$ Equation 5.7

where $\boldsymbol{\tau_{const} = 2/AN_0}$ gives the relation between the aggregation time constant, $\boldsymbol{\tau_{const}}$, the concentration of particles per volume unit, $\mathbf{N_0}$, and the constant reaction kernel, **A**.

If $\mathbf{a_{nn'} = B(n\text{-}n')}$, known as the *sum kernel*, effective collisions are more likely between two large aggregates that between two small aggregates, corresponding to reaction-limited aggregation. In this case, the **n-*mer*** distribution is given by:

$$X_n^{sum} = \frac{(1 - b_{sum})e^{-nb_{sum}}(nb_{sum})^{n-1}}{n!}$$ Equation 5.8

where

$$b_{sum} = b_f\left(1 - e^{-t/\tau_{sum}}\right)$$ Equation 5.9

$\mathbf{b_{sum}}$ representing the extent of aggregation, $\mathbf{b_f}$ is a parameter indicating the final extent of measured aggregation and $\boldsymbol{\tau_{sum} = 1/BN_0}$ gives the relation between the aggregation time constant ($\boldsymbol{\tau_{sum}}$), the concentration of particles per volume unit ($\mathbf{N_0}$), and the parameter **B** (the sum kernel).

### 5.3.3.2. Results and Discussion

Figure 5.14 shows that the introduction of different amounts of streptavidin in biotinylated-nanoparticles solutions affects differently the rates at which the nanoparticles aggregate. It is clear that, at streptavidin-to-nanoparticle ratios outside the range from 4:1 to 6:1, not only the final degrees of aggregation are considerably smaller but also are reached at lower rates.

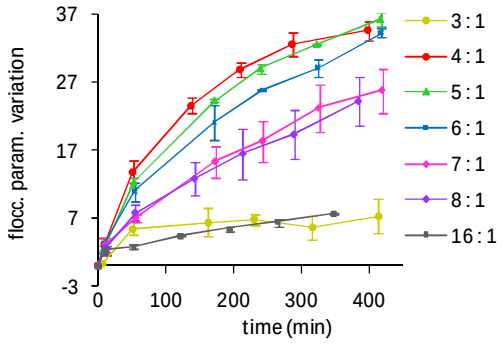


**Figure 5.14** – Flocculation parameter variation of samples with streptavidin-to-nanoparticle ratios between 3:1 and 16:1. (The lines that connect the marks are just an aid to guide the eye.)

In fact, it was observed that for samples with streptavidin ratios above 16:1 and below 3:1 the flocculation parameter variation was quite small and not much different from the response of the control samples. Figure 5.15 shows that the signals of the flocculation parameter variation are negligible in control samples, indicating that the functionalization procedure employed here results in colloidal solutions of functionalized AuNPs that are specific for the detection of streptavidin.

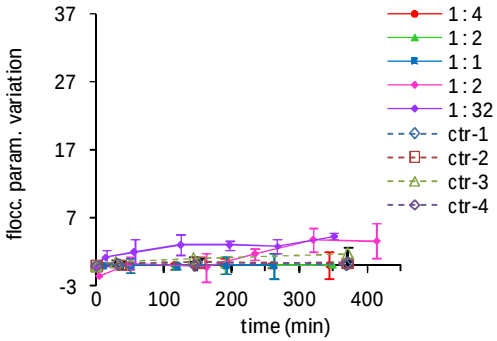


**Figure 5.15** - *Continuous lines*: flocculation parameter variation of samples with streptavidin-to-nanoparticle ratios above 16:1 and below 3:1. *Dashed lines*: flocculation parameter variation along time of control samples. Four types of specificity control experiments were performed: BSA (Bovine Serum Albumin) was mixed in a solution of biotinylated AuNPs, at a BSA-to-nanoparticle ratio of 5 :1; Milli-Q water containing 0.1% of $NaN_3$ was mixed in a solution of biotinylated AuNPs, in a volume equal to that of the streptavidin introduced at a ratio of 5 :1; Streptavidin was introduced at ratio of 5:1, in a solution of nanoparticles to which milli-Q water was mixed instead of biotin during the functionalization procedure; Streptavidin was introduced at ratio of 5:1, in a solution of nanoparticles to which BSA was mixed instead of biotin during the functionalization procedure. (The lines that connect the marks are just an aid to guide the eye.)

Equation 5.7 and Equation 5.9 representing the extent of aggregation in diffusion-limited and reaction-limited models, respectively, were used to analyze the experimental data shown in Figure 5.14. As a result, Figure 5.16 shows that Equation 5.9 was successful in fitting the flocculation data from samples with streptavidin-to-nanoparticle ratios in the range between 4:1 and 8:1, as indicated by correlation factors above 0.98. Outside this ratio range, however, the fittings produced were very poor, probably due to the very low variation of the flocculation parameter values.

The fittings performed using Equation 5.7, on the other hand, resulted in very low correlation factors, indicating that this model is not adequate to describe the experimental data. As an example, Figure 5.17 shows comparison between the curves resulting from fitting both equations to data from samples with a streptavidin-to-nanoparticle ratio of 4:1.

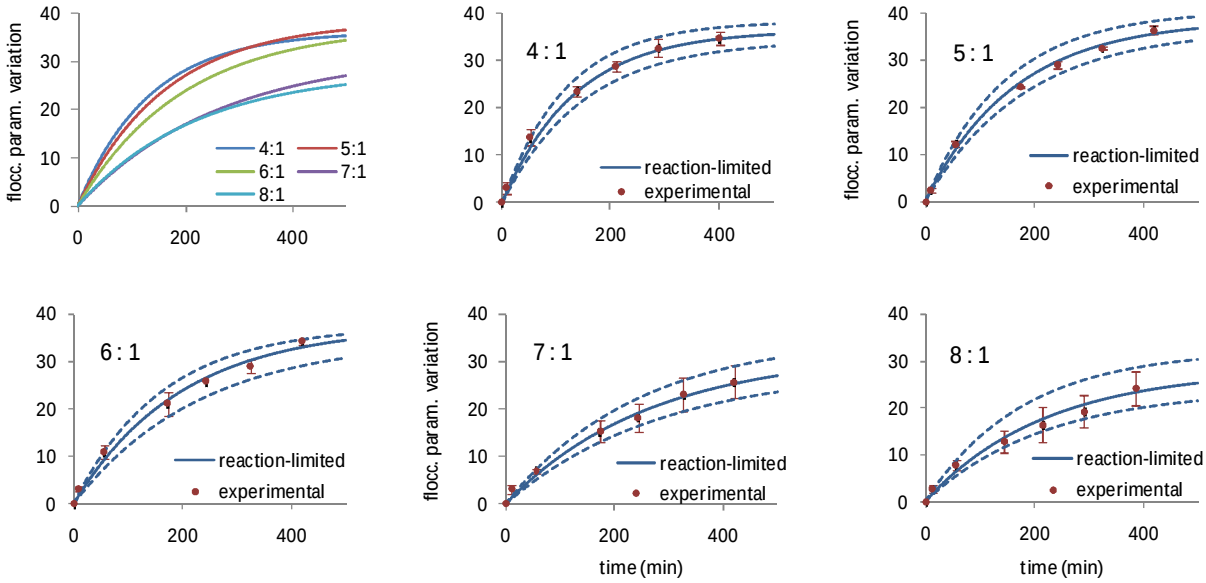


**Figure 5.16** – *Top left-hand plot*: comparison of the curves resulting from the fitting Equation 5.9 to the flocculation parameter data from samples with streptavidin-to-nanoparticle ratios between 4:1 and 8:1 presented in Figure 5.14. In the remaining plots: the *red-dots* are the experimental values averaged over triplicates samples, with the respective standard deviation error bars; *continuous lines* are plots resulting from the averaged fitting parameters of each triplicate set of samples for each streptavidin-to-nanoparticle ratio; *dashed lines* are curves of the maximum and minimum fits considering the error resulting from the calculation of the fitting parameters. All fits, produced in OriginLab© 7.5, presented $R^2$ values above 0.98.

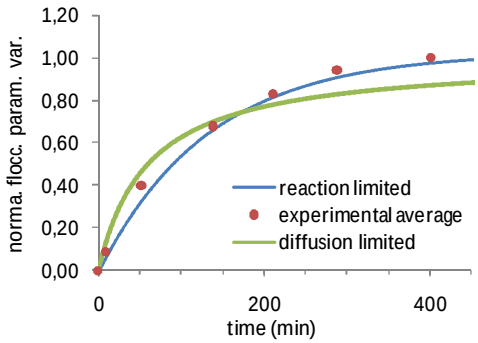


**Figure 5.17** – Comparison between the fitting results of both models, with the average of experimental flocculation data from the set of samples with streptavidin-to-nanoparticle ratio of 4:1. Note that the flocculation data was normalized to the maximum value before both fittings, because the diffusion-limited equation may only vary between 0 a 1.

Within the 4:1 to 7:1 streptavidin-to-nanoparticle ratios, the aggregation time-constant (quantifying the rate at which aggregation progresses) shows an increasing tendency when the relative quantities of streptavidin are increased (Figure 5.18). That is: the higher the streptavidin-to-nanoparticle ratio, the slower the aggregation progresses. This may be justified considering that increasing the amounts of streptavidin leads to the blocking of a greater number of biotins on the nanoparticles surfaces. A lower number of available biotin molecules for crosslinking with streptavidin attached to other nanoparticles will necessarily lead to a decrease on the number of collisions that result in crosslinking between two nanoparticles (or nanoparticle

aggregates), which slows down the aggregation rate.

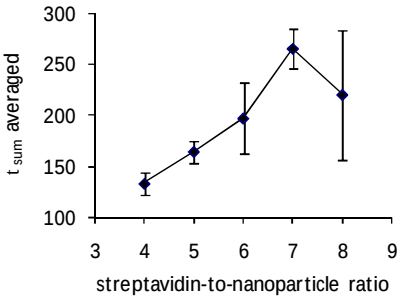


**Figure 5.18** – Variation of the average time constant, $\tau_{sum}$, relative to the streptavidin-to-nanoparticles ratio (in the interval between 4:1 and 8:1. (The line that connect the marks are just an aid to guide the eye.)

The fits performed with samples where streptavidin was introduced at an 8:1 ratio seem to contradict the referred tendency. However, it should be noticed that in this case, the resulting error bar is quite large, although the cause for this is still unexplained.

### 5.3.4. Real-time Monitoring of Streptavidin Induced Aggregation

A sample, with a streptavidin-to-nanoparticle ratio of 4:1, was prepared and used to observe the "non-disturbed" aggregation kinetics of biotinylated AuNPs. That is, contrary to the procedure explained before (of shaking and transferring each sample from reaction vial to the quartz cell before each measurement), this sample was left standing undisturbed on the spectrophotometer during the time for acquisition of all the spectra (Figure 5.19), starting immediately before introducing streptavidin and ending close to 16 hours after.

In Figure 5.20, where the optical parameters evolution along time are explicitly shown, one can see that the SPR peak shifts to higher wavelengths immediately after introducing the streptavidin molecules in the colloidal solution of biotinylated-nanoparticles – 6 nm in 20 minutes (blue to green spectra in Figure 5.19). This initial "red-shifting" is accompanied by a slight increase of the absorption intensity values at the resonance peak, indicating changes on the dielectric conditions at the nanoparticles surfaces (Storhoff et al, 2000; Guarise *et al.*, 2005). This result supports the hypothesis of the fast binding of streptavidin to the biotin molecules immobilized at the nanoparticles surfaces at initial stages. This does not mean, however, that no aggregation occurred to this stage – there is also a slight increase of the flocculation parameter values which can be related to either or both of the effects (aggregation and/or changing of the

dielectric conditions).

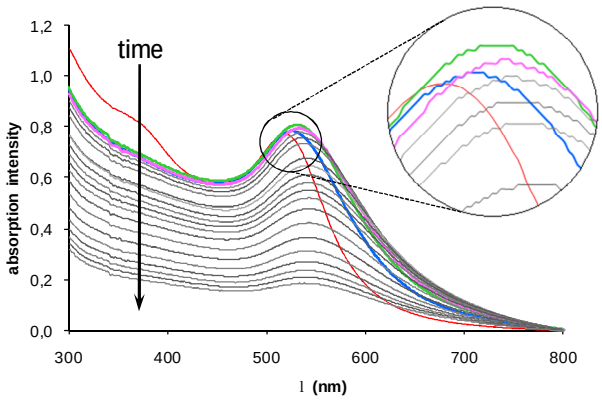


**Figure 5.19** – Spectral evolution of a sample of biotinylated AuNPs to which streptavidin was mixed at a streptavidin-to-nanoparticle ratio of 4:1. Spectra were acquired continuously for approximately 16 hours (one spectrum every 20 minutes), without disturbing the sample. Only about 1/3 of the acquired spectra is shown for the sake of clarity. *Red spectrum*: stock bare AuNPs. *Blue spectrum*: biotinylated AuNPs before the introduction of streptavidin. *Green spectrum*: acquired 20 minutes after the introduction of streptavidin. *Purple spectrum*: acquired 40 minutes after the introduction of streptavidin.

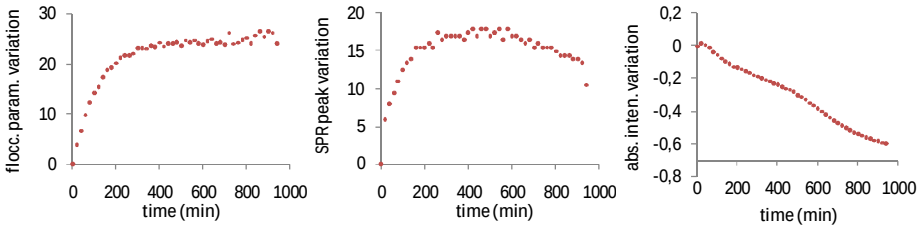


**Figure 5.20** – Variation of optical parameters corresponding spectra in Figure 5.19. *Left-hand side*: flocculation parameter variation. *Middle*: resonance peak position variation. *Right-hand side*: absorption intensity variation at the resonance peak.

The next measured spectrum (purple spectrum in Figure 5.19) shows that the shifting of the SPR peak to higher wavelengths continues, as well as the spectrum broadening. On the other hand, the absorption intensity at the peak starts to decrease, indicating that now the dominating reaction is the aggregation (Storhoff *et al.*, 2000). From this point forward, the tendency for spectrum broadening, absorption intensity decreasing and peak shifting to higher wavelengths continues, translating on the increase of the flocculation parameter values, as aggregation progresses.

Furthermore, Figure 5.20 also shows that the flocculation parameter diminishes clearly its increasing rate approximately 300 minutes after introducing the streptavidin and reaches a plateau at approximately 400 minutes, indicating that most of the aggregation has occurred. The wavelength variation of the SPR peak follows closely the shape of the flocculation parameter

variation plot, until approximately 10 hours after the introduction of streptavidin. At this stage, however, the situation is reversed as the SPR peak starts "shifting back" towards lower wavelengths. This effect was attributed to the precipitation of the larger aggregates to the bottom of the quartz cell, reducing the number of AuNP aggregates in suspension that absorb at the higher wavelengths.

Figure 5.21 shows that Equation 5.9, representing the reaction-limited model of aggregation, fits very well to the experimental data obtained from this sample, with fitting parameters values within the range discussed above for samples with identical streptavidin concentrations.

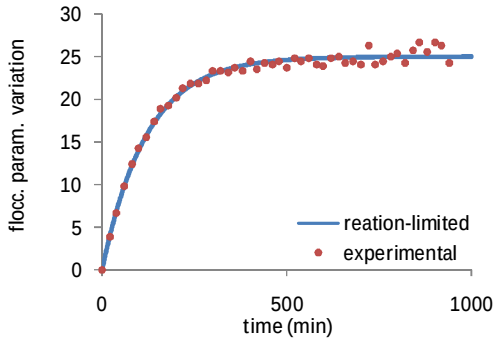


**Figure 5.21** – Fitting of the reaction-limited model (Equation 5.9) to the flocculation parameter data retrieved from spectra in Figure 5.19. Fit parameters: $\mathbf{b_f}$ = 24.9; $\tau_{sum}$ = 120.4 s; $R^2$ = 0.99.

## 5.4. Conclusions

A successful one-pot functionalization procedure was established for biomolecular activation of bare AuNPs surfaces, resulting in colloidal solutions that remained stable for several weeks. The minimal spectral differences detected between the stock AuNPs and those biologically activated, were attributed to the different dielectric characteristics conferred to the metal surfaces by both the self-assembled-monolayer and the salts in the buffer.

Furthermore, those biotin-functionalized AuNPs proved capable of specific detection of streptavidin molecules in solution, at concentrations as low as 7.2 nM, with the optimal detection signal found when streptavidin was mixed into solution at streptavidin-to-nanoparticle ratios of 5:1 (corresponding to 9 nM of streptavidin concentration).

It was also found that, even though the functionalization procedure resulted in stable colloidal solutions, the density of probe molecules (biotin) at the nanoparticles surfaces seems to

be very low (16 to 24 probes per nanoparticle) when considering the estimated maximum coverage (close to 1400 probes per nanoparticle). Consequently, the maximum signal of aggregation was limited not by the surface coverage with target molecules (streptavidin) but by the limited number of probe molecules at the nanoparticles surfaces.

Then, could the detection efficiency be enhanced with higher density of probe molecules (biotin) at the nanoparticles surfaces? Probably yes. On the studied conditions the aggregation regime is reaction-limited, meaning that there is a low concentration of aggregating particles and thus a large number of collisions are needed before two nanoparticles (or nanoparticles aggregates) aggregate by biomolecular recognition. A higher superficial density of biotin would probably allow increasing the number of streptavidin molecules per AuNP without significantly decreasing the number of available biotin molecules left for crosslinking (with other streptavidin coated AuNPs). Increasing the superficial density of streptavidin molecules (to a certain point) could then increase the "sticking probabilities" on each collision, which would increase the rate of aggregation (lowering the $\tau_{sum}$ values). Further investigations could probably significantly increase the superficial density of probe molecules by increasing, for instance, 10 or 100 fold its quantities during the functionalization procedure.

In summary, the work presented in this chapter sets grounds for the design of immunosensing assays, using the AuNPs colloidal characteristics as colorimetric transducers of biomolecular recognition.

# 6. Quantum Dots photoluminescence under long term-photoexcitation and temperature dependence

This chapter reports on the preliminary studies performed to evaluate the photoluminescence behavior of water-soluble CdSe/ZnS core/shell quantum dots under two different conditions: (1) long-term photo-excitation with laser light and (2) when exposed to different temperatures.

The responses obtained under those conditions are considered important factors in the context of the design and preparation of biosensing applications with quantum dots.

## 6.1. Introduction

In the context of application of quantum dots in life science research, the temperature and photo-induced luminescence-dynamics to which they are subjected in aqueous solutions are important parameters that should be verified and controlled to avoid degradation and/or compromise the interpretation of results.

Several groups have reported photo-induced effects affecting the stability and efficiency of quantum dots under continuous photo-excitation (Jones *et al.*, 2003; Maenosono *et al.*, 2003; Rodríguez-Viejo *et al.*, 2000; Zhelev *et al.*, 2004; Korsunska *et al.*, 2005; van Sark *et al.*, 2002; Neuhauser *et al.*, 2000). However, most of the times, the published results are divergent and difficult to compare given the multitude of factors affecting those results. These factors include: the different methods of synthesis resulting in different chemical and/or structural compositions of the quantum dots; the presence/absence of higher band-gap shell layers, their type and their

thickness; the presence/absence of capping agents and their type; the type of solvent (organic, inorganic or aqueous); the photo-excitation wavelength, power and duration; if the analysis is performed over single quantum dots, quantum dots solutions or quantum dots aggregates.

There are also many reports on the photoluminescence properties of quantum dots under a wide range of temperatures. However, many of those reports come mainly from research in group III-V quantum dots on the context of optoelectronic applications (particularly, InGaAs-based quantum dots). On the other hand, lesser reports on the temperature profiling of group II-VI quantum dots have been published, and comparison between them is affected by difficulty factors similar to those referred above (Liu *et al.*, 2006; Dai *et al.*, 2007; Chin *et al.*, 2007; Korsunska *et al.*, 2005; Salman *et al.*, 2007; Walker *et al.*, 2003).

In this chapter, quantum dot responses to long-term photo-excitation and exposed to different temperatures were investigated using commercially-available carboxylated-covered water-soluble core/shell quantum dots. The advantage of investigating this type of quantum dots is that the results may be readily applied and/or reproduced by anyone else working on the subject, since the differences from batch to batch solutions of quantum dots should be negligible when produced by the same methods and by the same supplier company. However, there is also a potential disadvantage: since the detailed processes of synthesis and physicochemical characteristics are usually inaccessible to the common user (under the label of: *proprietary information*), there is an increased difficulty in elaborating over the results obtained.

"Bottom line": if one is not interested in the particular details of the phenomena behind the effects, the investigation performed over commercially available quantum dots may be readily applied, allowing also the establishment of standards.

## 6.2. Materials and Methods

### 6.2.1. Reagents

Water-soluble carboxylated quantum dots solutions were acquired from Evident Technologies, with nominal emitting wavelength peaks at 520 and 540 nm (labeled Evitags-520 and Evitags-540, respectively) and used without further purification.

Di-sodium hydrogen phosphate, sodium dihydrogen phosphate monohydrate and sodium chloride, were acquired from Merck.

Sodium phosphate buffer was prepared in distilled water to a concentration of 10 mM, at pH 7.0, with three different salt concentrations: 0 mM, 100 mM and 200mM.

### 6.2.2. Experimental Setup

Figure 6.1 depicts the home-built experimental set-up used to conduct the photoluminescence experiments described further ahead in this chapter.

Quantum dot samples were excited by light from a continuous tunable air-cooled argon laser (Melles Griot, 43 series ion laser), set to emit at 488 nm at an output power of 104 mW. The laser beam is coupled to a 600 μm core optical fiber (BFH48-600, NA 0.48, Thorlabs) using a microscope objective (10x amplification, Melles Griot). The opposite fiber tip is attached to the temperature-controlled sample-chamber (TLC 50F, Quantum NorthWest), where light exiting from the fiber is collimated (by optics incorporated on the sample-chamber itself), to a beam with approximately 1 cm in diameter.

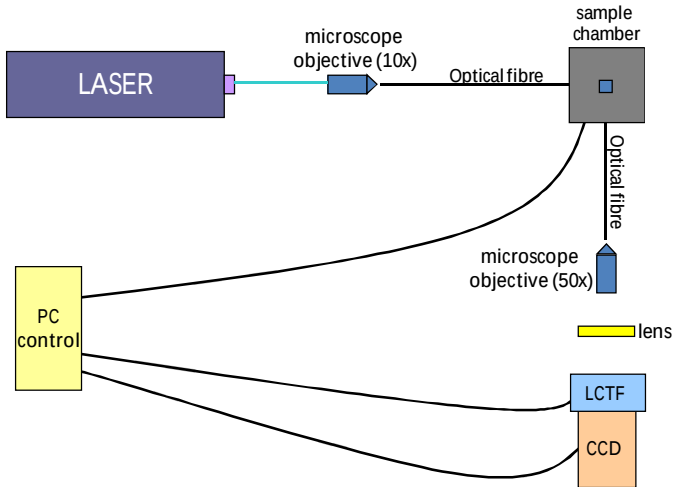


**Figure 6.1** – Experimental optical setup. LCTF = liquid crystal tunable filter; CCD = charge-coupled-device camera.

Inside the "TLC 50F" sample-chamber, the light beam excites the luminescent sample inserted in a 500 μL quartz cuvette (1 cm light path). The fluorescence light is then collected perpendicularly to the exciting beam and coupled to another 600 μm core optical fiber. The image at the opposite end of this fiber is then magnified by a 50x microscope objective (NA 0.75, from Leica) and focused on the sensor of a charge-coupled-device camera (CCD camera, Leica DC500) by an adjusting lens. Additionally, before entering the CCD-camera, the fluorescence light is wavelength filtered by a liquid-crystal-tuneable-filter (Varispec, CRI).

The intensity of each of the 2D images acquired by the CCD-camera is then extracted using the *ImageWarp* software, through a home-designed automatic script.

Particular care was taken to avoid overexposed images, as they would result in erroneous signals. Correct exposures were set by manual adjustment of the exposure times (ranging from 3.4 seconds down to 311.1 ms). Subsequently, the image intensity results were normalized relative to the exposure-times, for comparison.

## 6.2.3. Experimental Methods

### 6.2.3.1. Quantum Dots: temperature profiling

The sample used in this assay was prepared by diluting 50 µL quantum dots (Evitags-520) in 100 µL of distilled water ($[\text{Evitag-520}]_f$ = 3.33 µM). The photoluminescence properties were then studied as a function of the temperature between 0 and 45 ºC, using the heating and cooling profile shown in Figure 6.2. All spectra were acquired at least 15 minutes after temperature stabilization at each 5 ºC step.

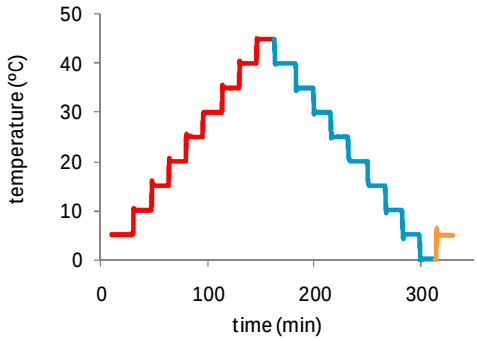


**Figure 6.2** – Heating-cooling cycle applied to the quantum dots sample. Initially, the sample was rapidly cooled from room-temperature to 5 ºC, and the first measurement was made approximately 20 minutes after temperature stabilization. The sample was then heated to 45 ºC, in 5 ºC steps, allowing for temperature stabilization for at least 15 minutes in each step before spectra acquisition. The sample was then cooled to 0 ºC and re-heated to 5 ºC, following the same procedures.

Spectra were acquired on the range between 500 and 540 nm, in 2 nm steps, with exposure times of 1 second per wavelength step. The sample was kept in dark at all times except during spectra acquisition.

Background images, used on the computational analysis, were acquired using distilled water (in place of the quantum dots sample) and following exactly the same procedures.

#### 6.2.3.2. Quantum Dots: long-term photo-excitation profiling

Six quantum dots samples were prepared by diluting 58 µL of Evitags-540 in 342 µL of three different 10mM phosphate buffers with different NaCl concentrations ($[Evitags\text{-}540]_f$ = 1 µM), according to the scheme shown in Table 6.1.

**Table 6.1** – Samples preparation scheme detailing the NaCl concentration present on the dilution buffer of each sample.

| illuminated samples | sample-A1 | sample-B1 | sample-C1 |
|---|---|---|---|
| non-illuminated samples | sample-A2 | sample-B2 | sample-C2 |
| [NaCl] (mM) | 0 | 100 | 200 |

Samples-A1, -B1 and -C1 were excited continuously with the laser beam on two different periods of time, lasting up to 9 hours each. Between the first and second excitation periods, the samples were allowed to rest in dark, at room temperature, for one day-time. During both excitation periods, images were acquired periodically at 538 nm (emission peak measured right-after the preparation of the samples). Since, continuous excitation of the quantum dots solutions results in increased fluorescence signals, the exposure-times were manually-adjusted (diminished) over the illumination time to avoid overexposed images.

Samples-A2, -B2 and -C2, used as controls, were kept in dark at all times (and at room temperature) except for spectra acquisition.

Absorption and emission spectra were acquired from all samples at several times during the 3 days took by each assay. All photoluminescence spectra were acquired at 20 ºC, on the range between 520 and 560 nm, in 2 nm steps. The absorption spectra were acquired between 400 and 700 nm, at room temperature.

## 6.3. Results and Discussion

### 6.3.1. Temperature Profiling

#### 6.3.1.1. Results

Figure 6.3 shows the evolution of the emission spectra of quantum dots throughout the heating and cooling steps. Additionally, given that the band-edge recombination of electron–hole

pairs within the CdSe core gives rise to a typical near-Gaussian emission band (Walker *et al.*, 2003), a set of optical characterizing parameters was extracted by gauss-fitting the experimental photoluminescence spectra. The variation of those parameters throughout the heating and cooling steps is plotted in Figure 6.4, where one can see that the wavelength maximum, width, and intensity are all dependent on temperature.

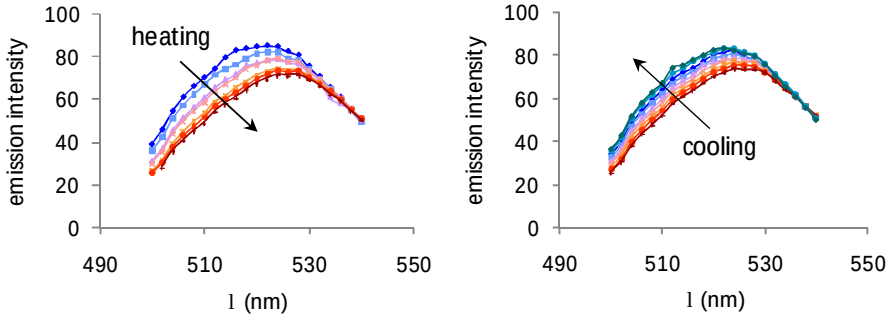


**Figure 6.3** – Evolution of the photoluminescence spectra throughout the heating (*left-hand side*) and cooling (*right-hand side*) steps.

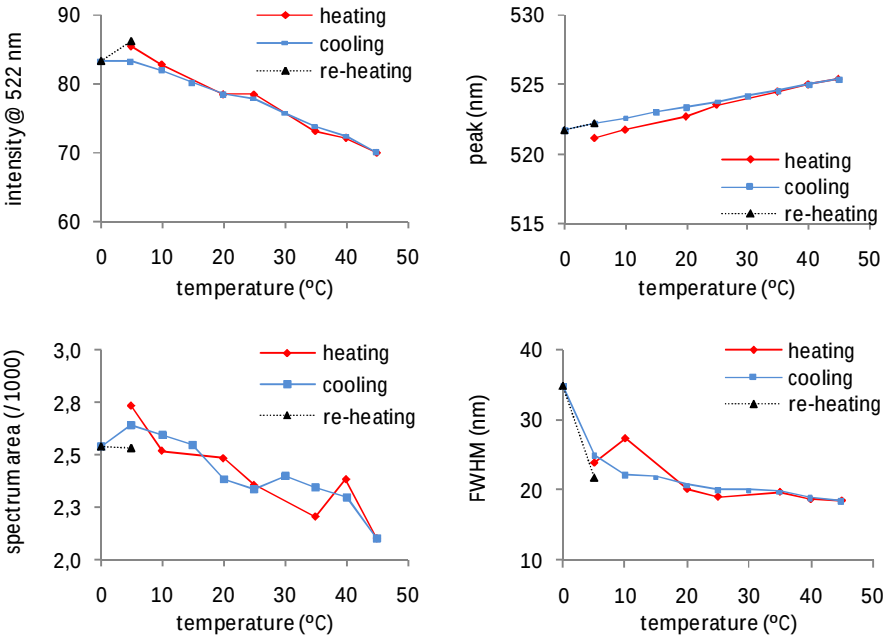


**Figure 6.4** – Variation of the optical parameters obtained by Gauss-fitting the spectra in Figure 6.3. All fittings produced correlation factors $R^2 > 0.99$. It was found that: (a) the emission peak shifts to higher wavelengths with increasing temperature, at approximately 0.11 nm/ºC (a value also reported by Liu *et al.*, 2006 and Dai et al, 2007); and (b) the emission intensity decreases linearly with increasing temperature, at approximately 0.38 /ºC.

### 6.3.1.2. Discussion

In semiconductors, the shifting to higher wavelengths of the photoluminescence emission peak with increasing temperature may be understood in terms of band gap "shrinkage", which

comes as a consequence of the broadening of the valence and conduction bands due to an increased number of vibrational states (Nepal *et al.*, 2005). The band gap wideness of bulk semiconductors generally shows a non-linear dependence on the temperature and has been described mostly by the empirical relation (Equation 6.1) proposed in 1967 by Varshni (Varshni, 1967; Nepal *et al.*, 2005; Korsunska *et al.*, 2005; Chin *et al.*, 2007; O'Donnell *et al.*, 1991).

$$E_g = E_0 - \alpha T^2/(T + \beta) \qquad \text{Equation 6.1}$$

where $\boldsymbol{\alpha}$ is the temperature coefficient, $\boldsymbol{\beta}$ is approximately the Debye temperature of the material and $\boldsymbol{E_0}$ is the band gap at 0 K. Additionally, it has been demonstrated that Equation 6.1 is valid also for semiconductor nanocrystals, with published values of $\boldsymbol{\alpha}$ and $\boldsymbol{\beta}$ for CdSe/ZnS dots in the ranges $3.2 \times 10^{-4}$ to $4.2 \times 10^{-4}$ eV/K, and 155 to 220 K, respectively (Chin *et al.*, 2007).

Using a known relation – $E = 1239.8/\lambda$ – to convert peak wavelength values into energy values, the variation of band gap width was plotted against temperature and the Varshni equation was fitted to the experimental data (Figure 6.5). The resulting fitting parameters – $\boldsymbol{E_0}$ = 2.5 ± $3.9 \times 10^{-3}$ eV, $\boldsymbol{\alpha}$ = $5.4 \times 10^{-4} \pm 1.9 \times 10^{-5}$ eV/K and $\boldsymbol{\beta}$ = 151.3 ± $9.4 \times 10^{-1}$ K – agree fairly well with the previously published values. [Published Debye temperature for bulk CdSe = 181 K (Madelung, 1999)].

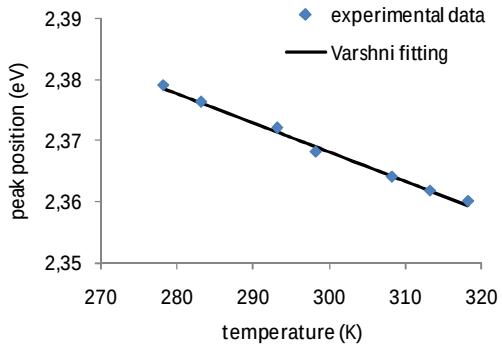


**Figure 6.5** – *Marks*: experimental data of the variation of the band-gap width as a function of the temperature. *Line*: Fit of Equation 6.1 to the experimental data ($R^2 > 0.99$)

The observed linearity of the photoluminescence intensity decline with increasing temperature (Figure 6.4) is of particular interest sensing applications and has been consistently reported by others. The effect has been attributed to thermally generated deep-traps in which

excitons “fall” and from where they recombine non-radiatively (Walker *et al.*, 2003; Liu *et al.*, 2006; Nepal *et al.*, 2005; Korshuska *et al.*, 2005).

Noteworthy, Figure 6.4 shows reversal of the photoluminescence parameters behavior upon cooling the samples. This is an indication that, within the range of temperatures studied, the Evitags do not undergo significant chemical modifications and that the temperature dependence of the optical properties can be ascribed mostly to reversible changes on the band gap width (Chin *et al.*, 2007) and to reversible formation of deep-trap states.

## 6.3.2. Long-term Photo-excitation Profiling

### 6.3.2.1. Results

Figure 6.6 shows the photoluminescence spectra evolution of sample-A1 during photo-excitation and resting periods. Samples-B1 and -C1 presented spectral behaviors very similar to that of sample-A1 and, thus, are not presented. The similarity between those responses may be better appreciated in Figure 6.7, where the intensity, emission peak, spectra integral and full-width-at-half-maximum variations are plotted. Figure 6.7 shows that, although the magnitude of the variation of each parameter presents small differences from sample to sample, the general profiles of variation are very much alike and independent of the salt concentration.

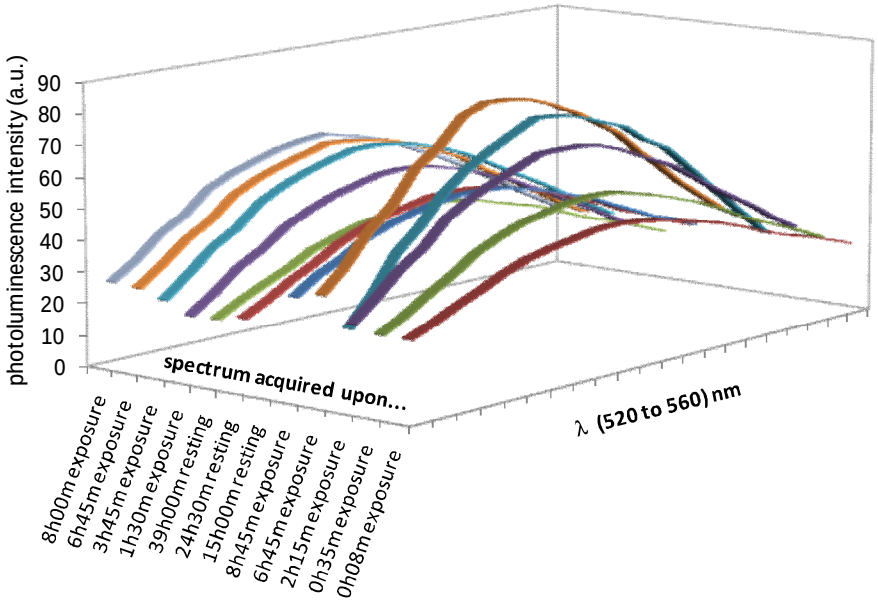


**Figure 6.6** – Photoluminescence spectra evolution of sample-A1, acquired at several times during photo-excitation and resting periods.

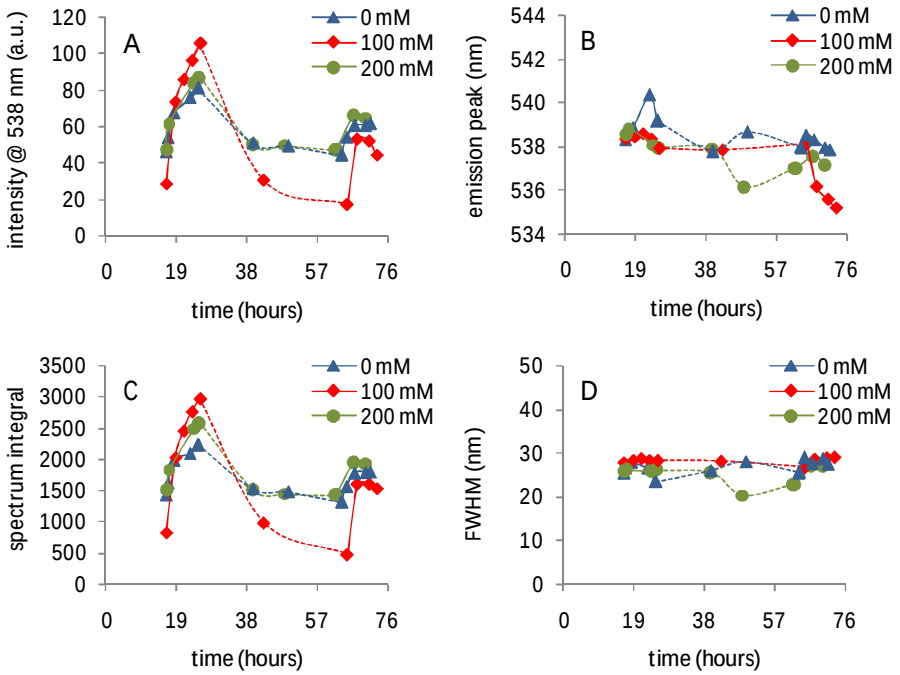


**Figure 6.7** – Variation of the optical parameters from samples -A1, -B1 and -C1 during photo-excitation (continuous lines) and resting periods (dashed lines). The parameter values were obtained by gauss-fitting the photoluminescence spectra. All fittings produced correlation factors $R^2 > 0.99$.

Figure 6.8 plots the photoluminescence spectra evolution along time of sample-A2, which was kept in dark at all times except for spectra acquisition. Figure 6.9 is the equivalent of Figure 6.7 for the non-photo-excited samples (A2, B2 and C2).

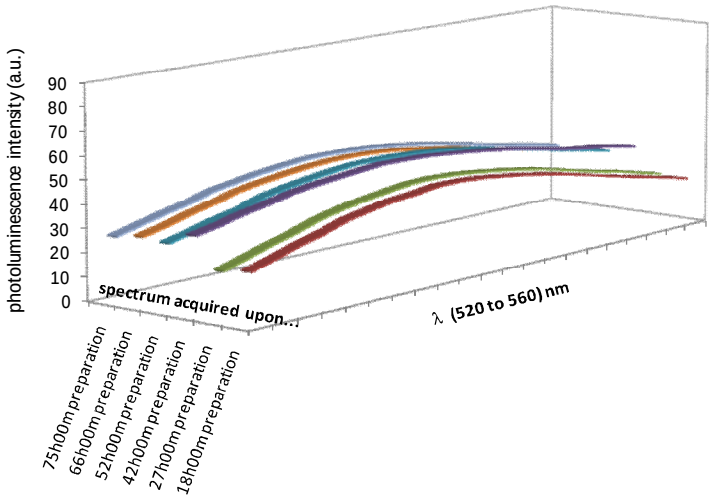


**Figure 6.8** - Photoluminescence spectra of sample-A2, acquired during the time that sample-A1 was under study.

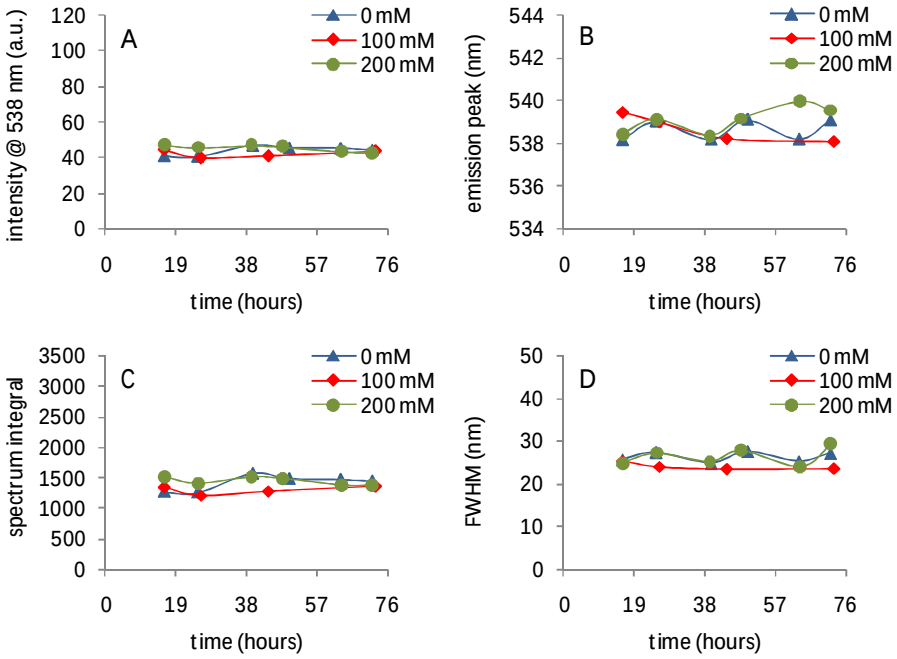


**Figure 6.9** – Variation of the optical parameters of samples -A1, -B2 and -C2 during the time that the corresponding photo-excited samples were under study. Parameter values were obtained by gauss-fitting the photoluminescence spectra. All fittings produced correlation factors $R^2 > 0.99$.

The absorption spectra from samples -A1 and -A2, acquired at several times during the assays, are plotted in Figure 6.10 (A and B, respectively). Absorption spectra from the remaining samples (both photo-excited and non-photo-excited) are very similar to those in Figure 6.10 and, thus, not shown. Figure 6.11 plots the variation of the absorption intensity at 520 nm as well as the variation of the peak position from all samples during the experiments.

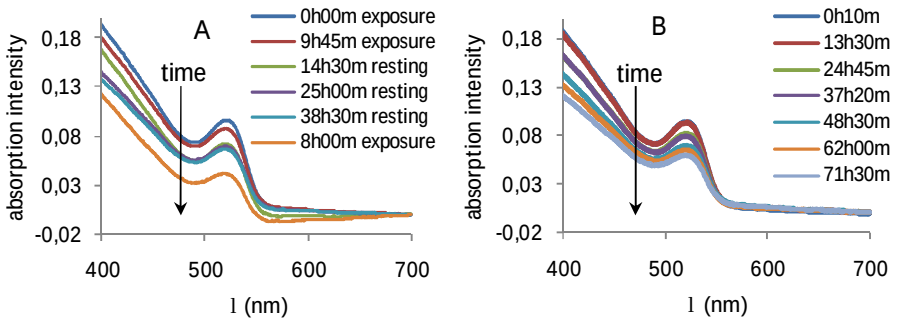


**Figure 6.10** – Absorption spectra evolution of: (A) sample-A1 and (B) sample-A2.

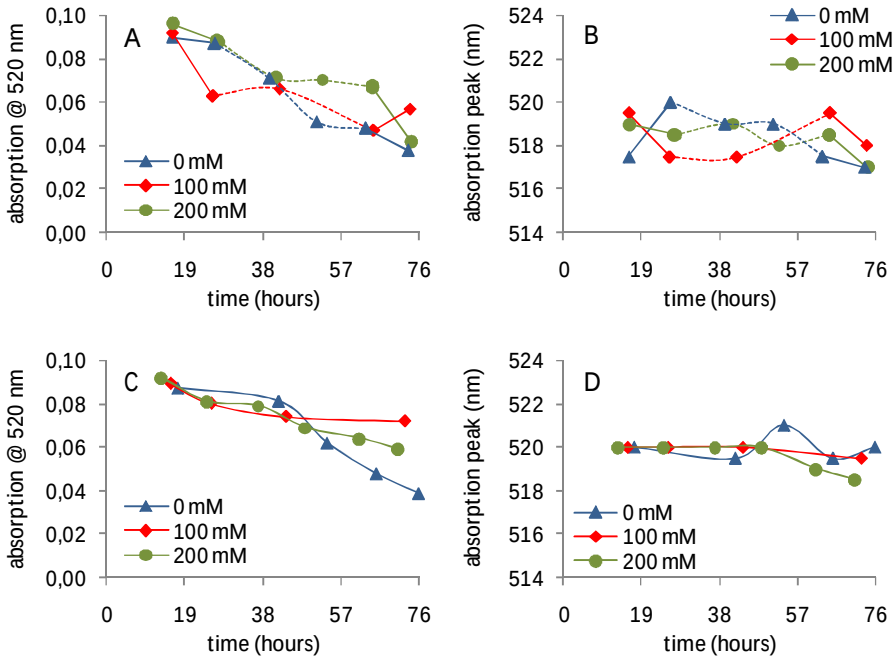


**Figure 6.11** – Variation of the absorption intensity and absorption peak position of samples exposed to long-term photo-excitation (A and B) and of samples kept in dark (C and D).

### 6.3.2.2. Discussion

Observing Figures 6.6 through 6.11, one can see that the most pronounced effect produced over the quantum dots photoluminescence profile, when continuously excited by the laser beam, is the strong increase of the emission intensity (Figure 6.7A). In fact, at the end of the first photo-excitation period, the emission intensity increased between 1.8- and 3.8-fold, while during the second period of excitation only a 1.4- to 3.0-fold increase was observed. It should be noticed though, that during the second photo-excitation period, the maximum of the emission intensity was recorded always several hours before terminating the excitation, then leveling up or even decreasing slightly. Furthermore, Figure 6.7A also shows that the resting period (dashed lines) results in the decrease of the emission intensities to values close to that obtained before starting photo-excitation (or even below).

The emission peak position and the full-width-at-half-maximum of the long-term photo-excited samples underwent only small variations, no higher than 3 and 7 nm, respectively (Figure 6.7, B and D, respectively). Nevertheless, the emission peak position seems to have a tendency to increase during the first part of both photo-excitation periods, decreasing afterwards. The variation profile of the spectra integral was found to follow closely that of the emission intensity (Figure 6.7C), being associated to the increase of the area below the spectra due to the

emission intensity increase rather than to spectra broadening, as indicated by the results in Figure 6.7D.

On the other hand, Figures 6.8 and 6.9 revel only negligible variations on the emission spectra profile of the control samples, indicating that the photoluminescence variations observed in long-term photo-excited samples can be attributed only to effects derived from the long-term photo-excitation itself.

Figure 6.11A shows that the optical absorption spectra of long-term photo-excited samples "suffer" a significant intensity decrease at 520 nm (the first absorption peak) during the assays. However, absorption spectroscopy results from non-illuminated samples show a similar intensity decrease behavior (Figure 6.11C), suggesting that it is not the long-term photo-excitation causing it. As for the variation of the position of the first absorption peak, Figure 6.11 shows that the variations are no higher than 2 nm and that there is no clear tendency for increasing or decreasing for both illuminated and non-illuminated samples.

All the results gathered suggest that the ionic strength of the buffers, in which the quantum dots were diluted, does not play any significant role on the photo-luminescent behavior of any of the samples. This is an indication that the outer capping-layer covering the quantum dots surfaces are effective in isolating the semiconductor material from the influences of the medium in which the dots are embedded.

The answer to what causes the photo-induced luminescence enhancement (Figure 6.7A) may lie on the electronic structure of the CdSe/ZnS quantum dots which may be represented as shown in Figure 6.12 (Jones *et al.*, 2003).

According to Jones and coworkers, once formed, the excitons decay to the lowest exciton state (named $|1\rangle$) in less than 1 ps, of which a portion then decays to the ground state (GS) in less than 100 ps. However, the recombination route may involve non-radiative deep-trap states (depicted on the right of Figure 6.12) originated by light-induced rearrangement of surface molecules. Then, excitons that "fall" on those trap-states may: (1) absorb energy enough to return to emitting states in $|1\rangle$ (the so called "thermalization"), resulting in delayed band-edge recombination; or (2) undergo further non-radiative decay to deep-trap levels that eventually produce a very weak deep-trap emission at longer wavelengths. It is proposed that long-term photo-excitation may increase the lifetimes of those deep-trap states, leading to an increase of the

chances that excitons "fallen" in those states thermalize back to an emitting |1⟩ state, therefore inducing a luminescence-enhancement effect.

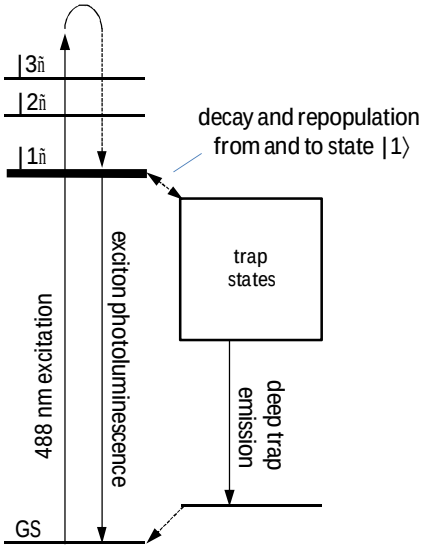


**Figure 6.12** – Representation of theoretically predicted electronic structure of CdSe/ZnS core/shell quantum dots, and proposed exciton decay route. (Adapted from Jones *et al.*, 2003)).

The results regarding the emission peak wavelength drifting (Figure 6.7B) may be qualitatively explained considering that the photoluminescence spectra of nanocrystal semiconductors are affected by electric fields – *the quantum Stark effect* – which occurs due to charging of the dots surfaces via, for instance, an Auger ionization process (Shen *et al.*, 1998; Neuhauser *et al.*, 2000). It is proposed that, under repeated photon excitation, sometimes, two electron-hole pairs may be simultaneously generated. Then, one electron-hole pair may recombine through the Auger channel by re-exciting a carrier from the other exciton through the CdSe surface energy barrier (Dneprovskii *et al.*, 2008). This emitted charge-carrier may be trapped in the surrounding medium or at the quantum dot core/shell interface, resulting in the appearance of an electric field. Subsequently, the recombination of electron-hole pairs created under this charged condition will be influenced by the electric field created by the emitted/trapped electron (Wang, 2001; Jones *et al.*, 2003). This Auger-assisted Stark effect predicts an excitonic peak shifting to lower energies with increasing electric field, as a result of the energy levels splitting and thus the reduction of band-gap (Menéndez-Proupin *et al.*, 2004; Wang, 2001; Jones *et al.*, 2003).

Thus, charge localized in surface traps could produce the initial shifting to slightly higher wavelengths while, at later times, a small and slow "shrinkage" of the quantum dots size would

result on the wavelength shift to lower wavelengths. However, data retrieved from the absorption spectra (Figure 6.11) does not allow confirming the later hypothesis since there is no clear shifting of the first absorption peak to lower wavelengths.

After computationally processed, the images acquired periodically at 538 nm from the photo-excited samples, during the two long-term photo-excitation periods, resulted in plots of the emission profile variation along time such as that shown in Figure 6.13.

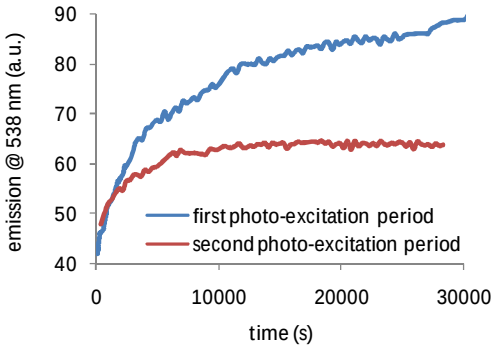


**Figure 6.13** – Emission intensity variation during the two long-term photo-excitation periods of sample-A1. Samples -B1 and -C1, present similar results.

Jones and co-workers found that the empirical stretched exponential function (also called Kohlrausch-Williams-Watts function), being commonly applied to relaxation and scattering phenomena (Cardona *et al.*, 2007), may be used also to model the rise in photo-luminescence quantum yield.

$$y = y_0 - A\,exp\left[-\left(\frac{t}{\tau}\right)^{\beta}\right] \qquad \text{Equation 6.2}$$

Here, the same function (Equation 6.2) was used to fit the emission intensity variation during long-term photo-excitation (where: $\mathbf{y_0}$ and **A** are fitting constants, **t** represents time, $\boldsymbol{\tau}$ is the system characteristic time scale and $\boldsymbol{\beta}$ ($\leq 1$) is the stretching parameter). Table 6.2 shows the resulting fitting parameters.

The results show that, in all cases, $\boldsymbol{\tau}$ decreases and $\boldsymbol{\beta}$ increases from first to second photo-excitation periods. These results, together with those presented in Figure 6.7, are an indication

that the physicochemical characteristics of the quantum dots were somehow altered by the long-term photo-excitation. However, the specificity of the induced-alterations was not determined.

**Table 6.2** – Results from fitting Equation 6.2 to the variation to the luminescence intensity during the long-term photo-excitation of samples -A1, -B1 and -C1.

| | | 1st | | | 2nd | | |
|---|---|---|---|---|---|---|---|
| sample-A1 | $y_0$ | 75,65 | ± | 0,50 | 59,87 | ± | 0,09 |
| | A | 39,84 | ± | 0,81 | 16,15 | ± | 0,39 |
| | τ | 4721,81 | ± | 166,71 | 3780,02 | ± | 125,49 |
| | β | 0,64 | ± | 0,02 | 0,79 | ± | 0,03 |
| | $R^2$ | | 0,99 | | | 0,99 | |
| sample-B1 | $y_0$ | 90,90 | ± | 0,38 | 61,32 | ± | 0,14 |
| | A | 102,98 | ± | 14,23 | 41,64 | ± | 1,92 |
| | τ | 3727,13 | ± | 120,52 | 993,67 | ± | 76,15 |
| | β | 0,64 | ± | 0,04 | 0,82 | ± | 0,09 |
| | $R^2$ | | 0,99 | | | 0,99 | |
| sample-C1 | $y_0$ | 89,12 | ± | 0,54 | 64,09 | ± | 0,09 |
| | A | 49,38 | ± | 0,82 | 18,55 | ± | 0,97 |
| | τ | 6240,51 | ± | 175,06 | 3112,41 | ± | 214,09 |
| | β | 0,71 | ± | 0,02 | 0,89 | ± | 0,06 |
| | $R^2$ | | 0,99 | | | 0,98 | |

## 6.4. Conclusions

Regarding the variation of their photoluminescence characteristics when subject to heating and cooling, it was found that Evitags show a reversible behavior within the range of temperatures studied. The energy band-gap was found to decrease linearly with increasing temperature, according to results previously reported by others. Furthermore, within the (short) range of temperatures studied, the variation of the band-gap wideness was found to fit also to the empirical Varshni equation, with fitting parameters values that agree fairly well with previously published results. Additionally, Evitags showed an apparently linear decline of the photoluminescence with increasing temperature. Although the decline is consistent with previously published results and attributed to thermally activated carrier trapping and non-radiative recombination at defects, no justification was found for the apparent linearity.

Thus, these preliminary results indicate that Evitags seem to be adequate to be used in biosensing applications, where the temperatures typically used dot not exceed the range studied here.

Evitags were found undergo a remarkable photoluminescence intensity enhancement when exposed to a below ban-gap laser beam for several hours. Furthermore, it was found that

the photo-enhancement procedure seems to impart some undetermined non-reversible changes on the physicochemical properties of the dots, since during the second period of long-term photo-excitation the photoluminescence spectra characteristics varied differently relative to the first period. One possible justification for the photo-induced luminescence enhancement, relates to the non-radiative decay of excitons to surface trap states that are created and/or photo-induced to exist long enough that there an increased possibility of their thermalization back to the exciton ground state, from where they may recombine to emit radiatively. The nature of the enhancement process is not yet understood but, independently of the model used for the interpretation, it is clear that the effect must be taken into account when considering experimental results that involve long periods of excitation.

# 7. Concluding Remarks

In this thesis, key steps were taken towards a better understanding of the physicochemical properties of gold nanoparticles and quantum dots that allow their exploitation on the development of biosensor strategies.

The absorption spectrum of colloidal solutions of gold nanoparticles is determined mostly by their surface plasmon resonances which are influenced, among other things, by environmental factors of the medium in which they are embedded and the degree of proximity between the nanoparticles. Particularly, if aggregation occurs, induced either by a shielding effect over the nanoparticles surface charges and/or as a consequence of biorecognition events that bringing the nanoparticles into close proximity, then marked spectral alterations are expected including the shifting to higher wavelengths of the SPR peak and spectrum broadening, due to the coupling of surface plasmon resonances of the individual nanoparticles. In this thesis, it was demonstrated that introducing certain amounts of ssDNA on colloidal solutions of AuNPs leads to a protection against salt induced aggregation, an effect that depends on the concentrations of both ssDNA and salt. On the other hand, identical amounts of dsDNA showed no interaction with the AuNPs solutions which aggregated when challenged with the same amounts of salt, as demonstrated by strong variations of the flocculation parameter. Consequently, the different forms of ssDNA and dsDNA interaction with AuNPs allow determining complementarity between two different DNA single-strands. Furthermore, experimental flocculation parameter data obtained from AuNPs samples containing different concentrations of ssDNA and NaCl were computed in light of a full-factorial-design, allowing obtaining of a regression model capable of predicting the combined influences of those two factors on the degree of aggregation of AuNPs solutions. The

accumulated knowledge gathered on the study of ssDNA-AuNPs interactions was further applied on the development of a colorimetrically biosensing method to detect the presence of *Influenza Virus* antigens in solution. Aptamers, being especially engineered oligonucleotide single strands and, thus, showing a similar behavior to that of "common ssDNA" on the protection of non-functionalized colloidal AuNPs against salt induced aggregation, were used as probes. The results expected were that, upon aptamer-antigen biorecognition, AuNPs should aggregate under the influence of certain amounts of salt, while in the presence of the aptamers solely, AuNPs should present an increased resistance against salt induced aggregation. It was observed that, in fact, aptamers exert a protection against salt induced aggregation over the colloidal solutions of AuNPs. However, the proposed detection strategy failed to produce a biorecognition signal. This failure was attributed to non-specific interactions between targets and nanoparticles (probably irreversible binding) which resulted also in protection against salt induced aggregation, thus, hindering the appearance of a biorecognition signal through aggregation. The potentialities of colloidal solutions of AuNPs were further applied on the development of colorimetric immunosensing strategies. In this context, a successful method was established to modify the AuNPs surfaces with a biological probe (biotin), through the formation of a self-assembled-monolayer of alkanethiol linker molecules on the nanoparticles surfaces. Then, the streptavidin-biotin was used as "ideal" target-probe pair to: (1) demonstrate the usefulness of AuNPs colloids as colorimetric signal transducing agents to detect proteinaceous analytes in solution and (2) study the streptavidin-biotin biorecognition induced aggregation kinetics.

In this thesis, the quantum dot responses to long-term photo-excitation and when exposed to different temperatures were investigated using commercially-available carboxylated-covered water-soluble core/shell quantum dots. It was found that, within the range of temperatures studied, the photoluminescence parameters varied almost linearly and reversibly, leading to believe no major physical or chemical alterations were produced on the quantum dots. On the other hand, the studied Evitags shown remarkable photoluminescence intensity enhancement when exposed to a (below ban-gap) laser beam for several hours. However, upon this photo-induced enhancement, the emission profile of the quantum dots did not return to the original status. One possible justification for these results is related to the photo-induced creation of deep-trap states that exist long enough where excitons "fall", contributing to an increased possibility of thermalization back to the exciton ground state, from where they may recombine to emit radiatively. Although the exact nature of the enhancement process is not yet understood, it

is clear that the effect must be taken into account when considering experimental results that involve long periods of excitation of the quantum dots.

## 7.1. Future work

The present work allowed opening a series of possibilities towards the development of nanoparticles-based colorimetric biosensors.

In what concerns the DNA sensing research (chapter 3) the line of investigation opened may follow now two routes. On one hand, the experimental procedure may evolve towards the detection of SNPs, namely, by finely varying the temperature of the samples around the melting temperature of the DNA hybrids. On the other hand, the mathematical design may be enhanced through the introduction of extra factors such as the particle size, DNA length and temperature.

The results from chapter 4 were inconclusive and, consequently, further research needs to be performed to answer the liabilities of the designed strategy. Most likely, AuNPs will need to be covered with some sort of SAM that inhibits non-specific iterations with haemagglutinins. This means an entirely new experimental design, probably not relying in electrostatic interactions between AuNPs and aptamers.

The research developed in chapter 5 opens doors for the application of AuNPs in immunosensing assays. The strategy designed to immobilize biotins on the AuNPs surfaces should be, in principle, adequate for immobilizing larger proteins (such as antibody and antigens) containing amine groups. Detection can then be performed relying on the aggregation signal due to crosslinking between antibody-functionalized AuNPs and antigen-functionalized AuNPs.

Since the basic steps on the understanding of the advantageous quantum dots properties for the development of biosensing assays have being taken, future work will most likely involve the combination gold nanoparticles and quantum dots in multiplexed RET-based biosensing assays.

# References


Aili D., Enander, K., Rydberg, J., Lundström, I., Baltzer, L., Liedberg, B., 2006. Aggregation-Induced Folding of a De Novo Designed Polypeptide Immobilized on Gold Nanoparticles. Journal of American Chemical Society 128, 2194-2195.

Algar, W. R., Krull, U. J., 2006. Adsorption and Hybridization of Oligonucleotides on Mercaptoacetic Acid-Capped CdSe/ZnS Quantum Dots and Quantum Dot−Oligonucleotide Conjugates. Langmuir, 22(26), 11346-11352.

Alvarez, M. M., Khoury, J. T., Schaaff, T. G., Shafigullin, M. N., Vezmar, I., Whetten, R., 1997. Optical Absorption Spectra of Nanocrystal Gold Molecules. Journal of Physical Chemistry B 101, 3706-3712.

Aslan, K., Lakowicz, J. R., Geddes, C. D., 2004. Tunable plasmonic glucose sensing based on the dissociation of Con A-aggregated dextran-coated gold colloids. Analytica Chimica Acta 517, 139–144.

Aslan, K., Luhrs, C. C., Pérez-Luna, V. H., 2004. Controlled and Reversible Aggregation of Biotinylated Gold Nanoparticles with Streptavidin. Journal of Physical Chemistry B 108, 15631-15639.

Aslan, K., Pérez-Luna, V. K., 2002. Surface modification of colloidal gold by chemisorption of alkanethiols in the presence of a nonionic surfactant. Langmuir 18, 6059-6065.

Aslan, K., Zhang, J., Lakowicz, J.R., Geddes, C. D., 2004. Saccharide sensing using gold and silver nanoparticles – A review. Journal of Fluorescence 14, 391-400.

Bagalkot, V., Zhang, L., Levy-Nissenbaum, E., Jon, S., Kantoff, P. W., Langer, R., Farokhzad, O. C., 2007. Quantum Dot˜Aptamer Conjugates for Synchronous Cancer Imaging, Therapy, and Sensing of Drug Delivery Based on Bi-Fluorescence Resonance Energy Transfer. Nano Letters 7(10), 3065-3070.

Bailey, R. E., Smith, A. M., Nie, S., 2004. Quantum dots in biology and medicine. Physica E 25, 1–12.

Baker, C. C., Pradhan, A., Shah, S. I., 2004. Metal Nanoparticles. In: Encyclopedia of Nanoscience and Nanotechnology 5, 449–473.

Balamurugan, S., Obubuafo, A., Soper, S. A., Spivak, D. A., 2008. Surface immobilization methods for aptamer diagnostic applications. Analytical and Bioanalytical Chemistry 390, 1009–1021.

Baptista, P., Pereira, E., Eaton, P., Doria, G., Miranda, A., Gomes, I., Quaresma, P., Franco, R., 2008. Gold nanoparticles for the development of clinical diagnosis methods. Analitycal and Bioanalitycal Chemistry 391, 943–950.

Bhattacharya, P., Bimberg, D., Arakawa, Y., 2007. Special Issue on Optoelectronic Devices Based on Quantum Dots. Proceedings of the IEEE 95( 9), 1718-1722.

Blagoi,G., Rosenzweig, N., Rosenzweig,Z., 2006. Fluorescence Resonance Energy Transfer-Based Sensors for Bioanalysis. In Fluorescence sensors and biosensors / edited by Thompson, R. B., Taylor & Francis Group.

Brust, M., Kiely, C. J., 2002. Some recent advances in nanostructure preparation from gold and silver particles: a short topical review. Colloids and Surfaces A: Physicochemical and Engineering Aspects 202(2-3), 175-186.

Cardona, M., Chamberlin, R. V., Marx, W., 2007. The history of the stretched exponential function. Annals of Physics 16(12), 842 – 845.

Caswell, K. K., Wilson, J. N., Bunz, U. H. F., Murphy, C. J., 2003. Preferential End-to-End Assembly of Gold Nanorods by Biotin−Streptavidin Connectors. Journal of the American Chemical Society 125(46), 13914-13915.

Chan, W. C. W., Nie, S., 1998. Quantum Dot Bioconjugates for Ultrasensitive Nonisotopic Detection. Science 281, 2016.

Chang, E., Miller, J. S., Sun, J., Yu, W. W., Colvin, V. L., Drezek, R., West, J. L., 2005. Protease-activated quantum dot probes. Biochemical and Biophysical Research Communications 334, 1317–1321.

Chen, W., Joly, A. G., Wang, S., 2004. Luminescence of Semiconductor Nanoparticles. In: Encyclopedia of Nanoscience and Nanotechnology 4, 689-718.

Chen, Y.-T., Hsu, C.-L., Hou, S.-Y., 2008. Detection of single-nucleotide polymorphisms using gold nanoparticles and single-strand-specific nucleases. Analytical Biochemistry 375, 299-305.

Chin, P. T. K., Doneg, C. M., van Bavel, S. S., Meskers, S. C. J., Sommerdijk, N. A. J. M., Janssen, R. A. J., 2007. Highly Luminescent CdTe/CdSe Colloidal Heteronanocrystals with Temperature-Dependent Emission Color. Journal of American Chemical Society 129(48), 14880-14886.

Clapp, A. R., Medintz, I. L., Mauro, J. M., Fisher, B. R., Bawendi, M. G., Mattoussi, H., 2004. Fluorescence Resonance Energy Transfer Between Quantum Dot Donors and Dye-Labeled Protein Acceptors. Journal of the American Chemical Society 126(1), 301-310.

Connolly, S., Cobbe, S., Fitzmaurice, D., 2001. Effects of Ligand-Receptor Geometry and Stoichiometry on Protein-Induced Aggregation of Biotin-Modified Colloidal Gold. Journal of Physical Chemistry B 105, 2222-2226.

Costa-Fernandez, J. M., 2006. Optical sensors based on luminescent quantum dots. Analytical and Bioanalytical Chemistry 384, 37–40.

Cui, H., Zhang, Z.-F., Shi, M.-J., Xu, Y., Wu, Y.-L., 2005. Light Emission of Gold Nanoparticles Induced by the Reaction of Bis(2,4,6-trichlorophenyl) Oxalate and Hydrogen Peroxide. Analytical Chemistry 77(19), 6402-6406.

Cui, R., Pan, H.-C., Zhu, J.-J., Chen, H.-Y., 2007. Versatile Immunosensor Using CdTe Quantum Dots as Electrochemical and Fluorescent Labels. Analytical Chemistry 79(22), 8494-8501.

Dabbousi, B. O., Rodriguez-Viejo, J., Mikulec, F. V., Heine, J. R., Mattoussi, H., Ober, R., Jensen, K. F., Bawendi, M. G., 1997. (CdSe)ZnS Core−Shell Quantum Dots: Synthesis and Characterization of a Size Series of Highly Luminescent Nanocrystallites. Journal of Physical Chemistry B 101(46), 9463-9475.

Dai, Q., Song, Y., Li, D., Chen, H., Kan, S., Zou, Bo, Wang, Y., Deng, Y., Hou, Y., Yu, S., Chen, L., Liu, B., Zou, G., 2007. Temperature dependence of band gap in CdSe Nanocrystals. Chemical Physics Letters 439, 65–68.

Daniel, M.-C., Astruc, D., 2004. Gold Nanoparticles: Assembly, Supramolecular Chemistry, Quantum-Size-Related Properties, and Applications toward Biology, Catalysis, and Nanotechnology. Chemical Reviews 104, 293-346.

Darbha, G. K., Singh, A. K., Rai, U. S., Yu, E., Yu, H., Ray, P. C., 2008. Selective Detection of Mercury (II) Ion Using Nonlinear Optical Properties of Gold Nanoparticles. Journal of American Chemical Society 130(25), 8038-8043.

Dneprovskii, V., Kabanin, D., Lyaskovskii, V., Wumaier, T., Zhukov, E., 2008. Anomalous resonant nonlinear absorption of excitons in CdSe/ZnS quantum dots. Physica Status Solidi (c) 5(7), 2503–2506.

Dobrovolskaia, M. A., Patri, A. K., Zheng, J., Clogston, J. D., Ayub, N., Aggarwal, P., Neun, B. W., Hall, J. B., McNeil, S. E., 2008. Interaction of colloidal gold nanoparticles with human blood: effects on particle size and analysis of plasma protein binding profiles. Nanomedicine: Nanotechnology, Biology, and Medicine. doi:10.1016/j.nano.2008.08.001

Driggers, R. G., 2003. Encyclopedia of Optical Engineering. CRC Press

Eck, D., Helm, C. A., 2001. Plasmon Resonance Measurements of the Adsorption and Adsorption Kinetics of a Biopolymer onto Gold Nanocolloids. Langmuir 17(4), 957-960.

Encarnação, J. M., 2007. Development of Biosensors for Molecular Analysis. PhD Thesis.

Famulok, M., Hartig, J. S., Mayer, G., 2007. Functional Aptamers and Aptazymes in Biotechnology, Diagnostics, and Therapy. Chemical Reviews 107(9), 3715-3743.

Gao, X., Chan, W. C. W., Nie, S., 2002. Quantum-dot nanocrystals for ultrasensitive biological labeling and multicolor optical encoding. Journal of Biomedical Optics 7(4), 532–537.

Gerion, D. Chen, F., Kannan, B., Fu, A., Parak, W. J., Chen, D. J., Majumdar, A., Alivisatos, A. P., 2003. Room-Temperature Single-Nucleotide Polymorphism and Multiallele DNA Detection Using Fluorescent Nanocrystals and Microarrays. Analytical Chemistry 75(18), 4766-4772.

Gestwicki, J. E., Strong, L. E., Kisseling, L. L., 2000. Visualization of Single Multivalent Receptor-Ligand Complexes by Transmission Electron Microcopy. , Angewandte Chemie International Edition 39(24), 4567 –4570.

Ghosh, S. K., Pal, T., 2007. Interparticle Coupling Effect on the Surface Plasmon Resonance of Gold Nanoparticles: From Theory to Applications. Chemical Reviews 107, 4797-4862.

Goldman, E. R., Medintz, I. L., Whitley, J. L., Hayhurst, A., Clapp, A. R., Uyeda, H. T., Deschamps, J. R., Lassman, M., Mattoussi, H., 2005. A Hybrid Quantum Dot−Antibody Fragment Fluorescence Resonance Energy Transfer-Based TNT Sensor. Journal of the American Chemical Society 127(18), 6744-6751.

Goldman, E. R., Clapp, A. R., Anderson, G. P., Uyeda, H. T., Mauro, J. M., Medintz, I. L., Mattoussi, H., 2004. Multiplexed Toxin Analysis Using Four Colors of Quantum Dot Fluororeagents. Analytical Chemistry 76(3), 684-688.

Goldman, E. R., Medintz . I. L., Mattoussi, H., 2006. Luminescent quantum dots in immunoassays. Analytical and Bioanalytical Chemistry 384, 560–563.

Goldman, E. R., Medintz, I. L., Hayhurst, A., Anderson, G. P., Mauro, J. M., Iverson, B. L., Georgiou, G., Mattoussi, H., 2004. Self-assembled luminescent CdSe–ZnS quantum dot bioconjugates prepared using engineered poly-histidine terminated proteins. Analytica Chimica Acta 534, 63–67.

Goldman, E. R., Medintz, I. L., Whitley, J. L., Hayhurst, A., Clapp, A. R., Uyeda, H. T., Deschamps, J. R., Lassman, M. L., Mattoussi, H., 2005. A Hybrid Quantum Dot−Antibody Fragment Fluorescence Resonance Energy Transfer-Based TNT Sensor. Journal of the American Chemical Society 127(18), 6744-6751.

Graham, D., Mallinder, B. J., Smith, W. E., 2000. Surface-enhanced resonance Raman scattering as a novel method of DNA discrimination. Angewandte Chemie International Edition 39, 1061-1063.

Grönbeck, H., Curioni, A., Andreoni, W., 2000. Thiols and Disulfides on the Au(111) Surface: The Headgroup-Gold Interaction. Journal of American Chemical Society 122, 3839-3842.

Grubor, N. M., Shinar, R., Jankowiak, R., Porter, M. D., Small, G. J., 2004. Novel biosensor chip for simultaneous detection of DNA-carcinogen adducts with low-temperature fluorescence. Biosensors and Bioelectronics 19, 547–556.

Guarise, C., Pasquato, L., Filippis, V., Scrimin, P., 2006. Gold nanoparticles-based protease assay. Proceedings of the National Academy of Sciences 103(11), 3978–3982

Guarise, C., Pasquato, L., Scrimin, P., 2005. Reversible Aggregation/Desaggregation of Gold Nanoparticles Induced by a Cleavable Dithiol Linker. Langmuir 21, 5537-5541.

Gueroui, Z., Libchaber, A., 2004. Single-Molecule Measurements of Gold-Quenched Quantum Dots. Physical Review Letters 93(16), 166108.

Ha, T. H., Jeong, J. Y., Chung, B. H., 2005. Immobilization of hexa-arginine tagged esterase onto carboxylated gold nanoparticles. Chemical Communications 3959–3961.

Hamula, C. L. A., Guthrie, J. W., Zhang, H.,Li, X. F., Le, X. C., 2006. Selection and analytical applications of aptamers. Trends in Analytical Chemistry 25(7), 681-691.

Han, M., Gao, X., Su, J. Z., Nie, S., 2001. Quantum-dot-tagged microbeads for multiplexed optical coding of biomolecules. Nature Biotechnology 19, 631-635

Hazarika, P., Kukolka, F., Niemeyer, C. M., 2006. Reversible Binding of Fluorescent Proteins at DNA–Gold Nanoparticles. Angewandte Chemie 118, 6981 –6984.

Hermann, T., Patel, D. J., 2000. Adaptive Recognition by Nucleic Acid Aptamers. Science 287, 820-825.

Hines, M. A., Guyot-Sionnest, P., 1996. Synthesis and Characterization of Strongly Luminescing ZnS-Capped CdSe Nanocrystals. Journal of Physical Chemistry 100(2), 468-471.

Ho, Y.-P., Kung, M. C., Yang, S., Wang, T.-H., 2005. Multiplexed Hybridization Detection with Multicolor Colocalization of Quantum Dot Nanoprobes. Nano Letters 5(9), 1693-1697.

Huang, C.-C., Huang, Y.-F., Cao, Z., Tan, W., Chang, H.-T., 2005. Aptamer-Modified Gold Nanoparticles for Colorimetric Determination of Platelet-Derived Growth Factors and Their Receptors. Analytical Chemistry 77(17), 5735-5741.

Jayasena, S. D., 1999. Aptamers: An Emerging Class of Molecules That Rival Antibodies in Diagnostics. Clinical Chemistry 45(9), 1628–1650.

Jones, M., Nedeljkovic, J., Ellingson, R. J., Nozik, A. J., Rumbles, G., 2003. Photoenhancement of Luminescence in Colloidal CdSe Quantum Dot Solutions. Journal of Physical Chemistry 107, 11346-11352.

Kampani, K., Quann, K., Ahuja, J., Wigdahl,B., Khan, Z. K., Jain, P., 2007. A novel high throughput quantum dot-based fluorescence assay for quantitation of virus binding and attachment. Journal of Virological Methods 141, 125–132.

Katz, E., Willner, I., 2004. Integrated Nanoparticle–Biomolecule Hybrid Systems: Synthesis, Properties, and Applications. Angewandte Chemie International Edition 43, 6042 – 6108.

Kell, A. J., Donkers, R. L., Workentin, M. S., 2005. Core Size Effects on the Reactivity of Organic Substrates as Monolayers on Gold Nanoparticles. Langmuir, 21, 735-742.

Kelly, K. L., Coronado, E., Zhao, L., Schatz, G. C., 2003. The optical properties of metal nanoparticles: the influence of size, shape and dielectric environment. Journal of Physical Chemistry B 107, 668-677.

Kerman, K., Endo, T., Tsukamoto, M., Chikae, M., Takamura, Y., Tamiya, E., 2007. Quantum dot-based immunosensor for the detection of prostate-specific antigen using fluorescence microscopy. Talanta 71, 1494–1499.

Kim, J. H., Morikis, D., Ozkan, M., 2004. Adaptation of inorganic quantum dots for stable molecular beacons. Sensors and Actuators B 102, 315–319.

Kim, Y., Johnson, R. C., Hupp, J. T., 2001. Gold Nanoparticle-Based Sensing of "Spectroscopically Silent" Heavy Metal Ions. Nano Letters 1(4), 165-167.

Kim, Y., Sohn, D., Tan, W., 2008. Molecular Beacons in Biomedical Detection and Clinical Diagnosis. International Journal of Clinical and Experimental Pathology 1, 105-116.

Klussmann, S., 2006. The Aptamer Handbook - Functional Oligonucleotides and Their Applications. WILEY-VCH Verlag GmbH & Co.KGaA, Weinh

Korsunska, N. E., Dybiec, M., Zhukov, L., Ostapenko, S., Zhukov, T., 2005. Reversible and non-reversible photo-enhanced luminescence in CdSe/ZnS quantum dots. Semiconductor Science and Technology 20, 876–881.

Kreibig, U., Gartz, M., Hilger, A., Hövel, H., Quinten, M., Wagner, D., Ditlbacher, 2006. A Short Survey of Optical Properties of Metal Nanostructures. Springer: Functional Properties of Nanostructured Materials, 75–110.

Kreibig, U., Quinten, M., 2004. In: Encyclopedia of Modern Optics Vol. 3

Lakowicz, J. R., 2005. Radiative decay engineering 5: metal-enhanced fluorescence and plasmon emission. Analytical Biochemistry 337, 171–194.

Lattuada, M., Wu, H., Sefcik, J., Morbidelli, M., 2006. Detailed Model of the Aggregation Event between Two Fractal Clusters. Journal of Phyical Chemistry B 110 (13), 6574-6586.

Lee, J., Kim, J., Park, E., Jo, S., Song, R., 2008. PEG-ylated cationic CdSe/ZnS QDs as an efficient intracellular labeling agent. Physical Chemistry Chemical Physics 10, 1739–1742.

Levy, M., Cater, S. F., Ellington, A. D., 2005. Quantum-Dot Aptamer Beacons for the Detection of Proteins. ChemBioChem 6, 2163 – 2166.

Lévy, R., Thanh, N. T. K., Doty, R. C., Hussain, I., Nichols, R. J., Schiffrin, D. J., Brust, M., Fernig, D. G., 2004. Rational and Combinatorial Design of Peptide Capping Ligands for Gold Nanoparticles. Journal of American Chemical Society 126, 10076-10084.

Li, D., He, Q., Cui, Y., Duan, L., Li, J., 2007. Immobilization of glucose oxidase onto gold nanoparticles with enhanced thermostability. Biochemical and Biophysical Research Communications 355, 488–493.

Li, H., Nelson, E., Pentland, A., van Buskirk, J., Rothberg, L., 2007. Assays based on differential adsorption of single-stranded and double-stranded DNA on unfunctionalized gold nanoparticles in a colloidal suspension. Plasmonics 2, 165-171.

Li, H., Rothberg, L. J., 2004. Label-free colorimetric detection of specific sequences in genomic DNA amplified by polymerase chain reaction. Journal of American Chemical Society 126, 10958-10961.

Liao, H., Hafner, J. H., 2005. Gold Nanorod Bioconjugates. Chemical Materials 17(18), 4636-4641.

Link, S., El-Sayed, M. A., 1999. Size and Temperature Dependence of the Plasmon Absorption of Colloidal Gold Nanoparticles. Journal Physical Chemistry B 103, 4212-4217.

Link, S., El-Sayed, M. A., 1999. Spectral Properties and Relaxation Dynamics of Surface Plasmon Electronic Oscillations in Gold and Silver Nanodots and Nanorods. Journal of Physical Chemistry 103(40), 8410-8426.

Link, S., El-Sayed, M. A., 2000. Shape and size dependence of radiative, non-radiative and photothermal properties of gold nanocrystals. International Reviews in Physical Chemistry 19(3), 409-453.

Liu, J., Lu, Y., 2005. Stimuli-Responsive Disassembly of Nanoparticle Aggregates for Light-Up Colorimetric Sensing. Journal of the American Chemical Society 127(36), 12677-12683.

Liu, J., Lu, Y., 2006. Fast Colorimetric Sensing of Adenosine and Cocaine Based on a General Sensor Design Involving Aptamers and Nanoparticles. Angewandte Chemie International Edition 45, 90 –94.

Liu, J., Tanaka, T., Sivula, K., Alivisatos, A. P., Frchet, J. M. J., 2004. Employing End-Functional Polythiophene To Control the Morphology of Nanocrystal−Polymer Composites in Hybrid Solar Cells. Journal of the American Chemical Society 126(21), 6550-6551.

Liu, L., Zheng, H.-Z., Zhang, Z.-J., Huang, Y.-M., Chen, S.-M., Hu, Y.-F., 2008. Photoluminescence from water-soluble BSA-protected gold nanoparticles. Spectrochimica Acta Part A 69, 701–705.

Liu, T.-C., Huang, Z.-L., Wang, H.-Q., Wang, J.-H., Li, X.-Q., Zhao, Y.-D., Luo, Q.-M., 2006. Temperature-dependent photoluminescence of water-soluble quantum dots for a bioprobe. Analytica Chimica Acta 559, 120–123

Love, J. C., Estroff, L. A., Kriebel, J. K., Nuzzo, R. G., Whitesides, G. M., 2005. Self-Assembled Monolayers of Thiolates on Metals as a Form of Nanotechnology. Chemical Reviews 105, 1103-1169.

Lynch, N. J., Kilpatrick, P. K., Carbonell, R. G., 1996. Aggregation of Ligand-Modified Liposomes be Specific Interactions with Proteins. I: Biotinylated Liposomes and Avidin. Biotechnology and Bioengineering 50, 151-168.

Madelung, O., Rössler, U., Schulz, M., 1999. Landolt-Börnstein - Group III Condensed Matter Numerical Data and Functional Relationships in Science and Technology - II-VI and I-VII Compounds; Semimagnetic Compounds.

Maenosono, S., Eiha, N., Yamaguchi, Y., 2003. Nonlinear Time-Series Analysis of Photoinduced Fluorescence Oscillation in a Water Dispersion of Colloidal Quantum Dots. Journal of Physical Chemistry B 107, 2645-2650.

McBride, J., Treadway, J., Feldman, L. C., Pennycook, S. J., Rosenthal, S. J., 2006. Structural Basis for Near Unity Quantum Yield Core/Shell Nanostructures. Nano Letters 6(7), 1496-1501.

Medintz, I. L., Clapp, A, R., Mattoussi, H., Goldman, E. R., Fisher, B., Mauro, J. M., 2003. Self-assembled nanoscale biosensors based on quantum dot FRET donors. Nature Materials 2, 630-638.

Medley, C. D., Smith, J. E., Tang, Z., Wu, Y., Bamrungsap, S., Tan, W., 2008. Gold Nanoparticle-Based Colorimetric Assay for the Direct Detection of Cancerous Cells. Analytical Chemistry 80(4), 1067-1072.

Menéndez-Proupin, E., Trallero-Giner, C., 2004. Stark effect in CdSe nanocrystals. Physica Status Solidi (c) 1(1), S42–S45.

Miller, M. M., Lazarides, A. A., 2005. Sensitivity of metal nanoparticle surface plasmon resonance to the dielectric environment. Journal of Physical Chemistry B 109, 21556-21565.

Mischler, R., Metcalfe, I. C., 2002.Inflexal®V a trivalent virosome subunit influenza vaccine: production. Vaccine 20, B17–B23.

Montgomery, D. C., 2001. Design and analysis of experiments 5th Edition. New York: John Wiley & Sons.

Montmeat, P., Marchand, J.-P., Lalauze, R., Viricelle, J.-P., Tournier, G., Pijolat, C., 2003. Physico-chemical contribution of gold metallic particles to the action of oxygen on tin dioxide sensors. Sensors and Actuators B 95, 83–89.

Mukherjee, P., Bhattacharya, R., Bone, N., Lee, Y. K., Patra, C. R., Wang, S., Lu, L., Secreto, C., Banerjee, P. C., Yaszemski, M. J., Kay, N. E., Mukhopadhyay, D., 2007. Potential therapeutic application of gold nanoparticles in B-chronic lymphocytic leukemia (BCLL): enhancing apoptosis. Journal of Nanobiotechnology , 5:4.

Mulvaney, P., 2001. Metal Nanoparticles: Double Layers, Optical Properties, and Electrochemistry. John Wiley & Sons, Inc.

Murray, C. B., Norris, D. J., Bawendi, M. G., 1993. Synthesis and characterization of nearly monodisperse CdE (E= sulfur, selenium, tellurium) semiconductor nanocrystallites. Journal of American Chemical Society 115(19), 8706-8715.

Myers, D., 1999. Surfaces, Interfaces and Colloids: Principles and Applications. Second Edition. New York: John Wiley & Sons. 519 p.

Nath, N., Chilkoti, A., 2002. A Colorimetric Gold Nanoparticle Sensor To Interrogate Biomolecular Interactions in Real Time on a Surface. Analytical. Chemistry 74, 504-509.

Nath, S., Kaittanis, C., Tinkham, A., Perez, J. M., 2008. Dextran-Coated Gold Nanoparticles for the Assessment of Antimicrobial Susceptibility. Analytical Chemistry 80(4), 1033-1038.

Neouze, M.-A., Schubert, U., 2008. Surface Modification and Functionalization of Metal and Metal Oxide Nanoparticles by Organic Ligands. Monatshefte für Chemie 139, 183–195.

Nepal, N., Li, J., Nakarmi, M. L., Lin, J. Y., Jiang, H. X., 2005. Temperature and compositional dependence of the energy band gap of AlGaN alloys. Applied Physics Letters 87, 242104.

Neuhauser, R. G., Shimizu, K. T., Woo, W. K., Empedocles, S. A., Bawendi, M. G., 2000. Correlation between Fluorescence Intermittency and Spectral Diffusion in Single Semiconductor Quantum Dots. Physical Review Letters 85(15), 3301-3304.

Niemeyer, C. M., 2001. Nanoparticles, Proteins, and Nucleic Acids: Biotechnology Meets Materials Science. Angewandte Chemie International Edition 40, 4128- 4158.

Nuopponen, M., Tenhu, H., 2007. Gold Nanoparticles Protected with pH and Temperature-Sensitive Diblock Copolymers. Langmuir 23, 5352-5357.

O'Donnell, K. P., Chen, .X. 1991. Temperature dependence of semiconductor band gaps. Applied Physics Letters 58(25), 2924-2926.

Otsuka, H., Akiyama, Y., Nagasaki, Y., Kataoka, K., 2001. Quantitative and Reversible Lectin-Induced Association of Gold Nanoparticles Modified with α-Lactosyl-ω -mercapto-poly(ethylene glycol). Journal of the American Chemical Society 123(34), 8226-8230.

Perez-Luna, V. H., Aslan, K., Betala, P., 2004. Colloidal Gold. In: Encyclopedia of Nanoscience and Nanotechnology 2, 27–49.

Pingarrón, J. M., Yáñez-Sedeño, P., González-Cortés, A., 2008. Gold nanoparticle-based electrochemical biosensors. Electrochimica Acta 53, 5848–5866.

Porter, M. D., Bright, T. B., Allara, D. L., Chidseyi, C. E. D., 1987. Spontaneously Organized Molecular Assemblies. 4. Structural Characterization of n-Alkyl Thiol Monolayers on Gold by Optical Ellipsometry, Infrared Spectroscopy, and Electrochemistry. Journal of American Chemical Society 109(12), 3559-3568.

Ratner, M., Ratner, D., 2003. Nanotechnology: A Gentle Introduction to the Next Big Idea. Prentice Hall PTR.

Rechberger, W., Hohenau, A., Leitner, A., Krenn, J. R., Lamprecht, B., Aussenegg, F.R., 2003. Optical properties of two interacting gold nanoparticles. Optics Communications 220, 137–141.

Reiss, P., Quemard, G., Carayon, S., Bleuse, J., Chandezon, F., Pron, A., 2004. Luminescent ZnSe nanocrystals of high color purity. Materials Chemistry and Physics 84, 10–13.

Rimmele, M., 2003. Nucleic Acid Aptamers as Tools and Drugs: Recent Developments. ChemBioChem 4, 963-971.

Robel, I., Subramanian, V., Kuno, M., Kamat, P. V., 2006. Quantum Dot Solar Cells. Harvesting Light Energy with CdSe Nanocrystals Molecularly Linked to Mesoscopic TiO2 Films. Journal of the American Chemical Society 128(7), 2385-2393.

Rodríguez-Viejo, J., Mattoussib, H., Heine, J. R., Kuno, M. K., Michel, J., Bawendi, M. G., Jensen, K. F., 2000. Evidence of photo- and electrodarkening of CdSeZnS quantum dot composites. Journal of Applied Physics 87(12), 8526-8534.

Salman, A., Tortschanoff, A., Mohamed,M. B., Tonti, D., van Mourik, F., Chergui, M., 2007. Temperature effects on the spectral properties of colloidal CdSe nanodots, nanorods, and tetrapods. Applied Physics Letters 90, 093104.

Sandström, P., Boncheva, M., Åkerman, B., 2003. Nonspecific and thiol-specific binding of DNA to gold nanoparticles. Langmuir 19, 7537-7543.

Sato, K., Hosokawa, K., Maeda, M., 2003. Rapid Aggregation of Gold Nanoparticles Induced by Non-Cross-Linking DNA Hybridization. Journal of the American Chemical Society 125(27), 8102-8103.

Schmid, G., 1992. Large clusters and colloids. Metals in the embryonic state. Chemical Reviews 92(8), 1709-1727.

Schmid, G., 1994. Clusters and Colloids From Theory to Applications. VCH Publishers, Inc., New York. 571p.

Schmid, G., Bäumle, M., Geerkens, M., Heim, I., Osemann, C., Sawitowski, T., 1999. Current and Future Applications of Nanoclusters. Chemical Society Reviews 28, 179-185.

Schmid, G., Corain, B., 2003. Nanoparticulated Gold: Syntheses, Structures, Electronics, and Reactivities. European Journal of Inorganic Chemistry 17, 3081-3098.

Schmitt, J., Mächtle, P., Eck, D., Möhwald, H., Helm, C. A., 1999. Preparation and Optical Properties of Colloidal Gold Monolayers. Langmuir 15(9), 3256-3266.

Schofield, C. L., Field, R. A., Russell, D. A., 2007. Glyconanoparticles for the Colorimetric Detection of Cholera Toxin. Analytical Chemistry 79(4), 1356-1361.

Sharma, J., Chhabra, R., Yan, H., Liu, Y., 2007. pH-driven conformational switch of ‘‘i-motif’’ DNA for the reversible assembly of gold nanoparticles. Chemical Communications, 477–479.

Shen, M., Y., Gotoy, T., Kurtzz, E., Zhuz,. Z., Yaoz, T., 1998 Photoluminescence properties of single CdSe quantum dots in ZnSe obtained by self-organized growth. Journal of Physics: Condensed Matter 10, L171–L176.

Shenton, W., Davis, S. A., Mann, S., 1999. Directed Self-Assembly of Nanoparticles into Macroscopic Materials Using Antibody/Antigen Recognition. Advanced Materials 11(6), 449-452.

Simonian, A. L., Good, T. A., Wang, S.-S., Wild, J.R., 2005. Nanoparticle-based optical biosensors for the direct detection of organophosphate chemical warfare agents and pesticides. Analytica Chimica Acta 534, 69–77.

Slocik, J. M., Tam, F., Halas, N. J., Naik, R. R., 2007. Peptide-Assembled Optically Responsive Nanoparticle Complexes. Nano Letters 7(4), 1054-1058.

Smith, A. M., Ruan, G., Rhyner, M. N., Nie, S., 2006. Engineering Luminescent Quantum Dots for In Vivo Molecular and Cellular Imaging. Annals of Biomedical Engineering 34(1), 3–14.

Song, S., Wang, L., Li, J., Zhao, J., Fan, C., 2008. Aptamer-based biosensors. Trends in Analytical Chemistry 27(2), 108-117.

Spiridonova, V. A., Kopylov, A. M., 2002. DNA Aptamers as Radically New Recognition Elements for Biosensors. Biochemistry (Mosc) 67(6), 850-854.

Storhoff, J. J., Lazarides, A. A., Mucic, R. C., Mirkin, C. A., Letsinger, R. L., Schatz, G. C., 2000. What controls the optical properties of DNA-linked gold nanoparticle assemblies? Journal of American Chemical Society 122, 4640-4650.

Stringer, R. C., Schommer, S., Hoehn, D., Grant, S. A., 2008. Development of an optical biosensor using gold nanoparticles and quantum dots for the detection of Porcine Reproductive and Respiratory Syndrome Virus. Sensors and Actuators B in press.

Su, K.-H., Wei, Q.-H., Zhang, X., Mock, J. J., Smith, D. R., Schultz, S., 2003. Interparticle Coupling Effects on Plasmon Resonances of Nanogold Particles. Nano Letters 3(8), 1087-1090.

Swanson, N. L., Billard, B. D., 2003. Optimization of extinction from surface plasmon resonances of gold nanoparticles. Nanotechnology 14, 353–357.

Tan, Y., Li, Y., Zhu, D., 2004. Noble Metal Nanoparticles. In: Encyclopedia of Nanoscience and Nanotechnology 8, 9–40.

Templeton, A. C., Pietron, J. J., Murray, R. W., Mulvaney, P., 2000. Solvent Refractive Index and Core Charge Influences on the Surface Plasmon Absorbance f Alkanethiolate Monolayer-Protected Gold Clusters. Journal of Physical Chemistry B 104, 564-570.

Thanh, N. T. K., Rosenzweig, Z., 2002. Development of an Aggregation-Based Immunoassay for Anti-Protein A Using Gold Nanoparticles. Analitycal Chemistry 74(7), 1624-1628.

Thaxton, C. S., Georganopoulou, D. G., Mirkin, C. A., 2006. Gold nanoparticle probes for the detection of nucleic acid targets. Clinica Chimica Acta 363, 120-126.

Thelander, C., Magnusson, M. H., Deppert, K., Samuelson, L., Poulsen, P. R., Nygard, J., Borggreen, J., 2001. Gold nanoparticle single-electron transistor with carbon nanotube leads. Applied Physics Letters, 79(13), 2106-2108.

Tombelli, S., Minunni, M., Mascini, M., 2007. Aptamers-based assays for diagnostics, environmental and food analysis. Biomolecular Engineering 24(2), 191–200.

Tominaga, M., Ohira, A., Yamaguchi, Y., Kunitake, M., 2004. Electrochemical, AFM and QCM studies on ferritin immobilized onto a self-assembled monolayer-modified gold electrode. Journal of Electroanalytical Chemistry 566, 323–329.

Turkevitch, J., Stevenson, P. C., Hillier, J., 1951. Nucleation and Growth Process in the Synthesis of Colloidal Gold. Discussions of the Faraday Society 11, 55-75.

Vaidya, B., Chen, J., Porter, M. D., Angelici, R. J., 2001. Effects of Packing and Orientation on the Hydrolysis of Ester Monolayers on Gold. Langmuir 17, 6569-6576.

van Sark, W. G. J. H. M., Frederix, P. L. T. M., van den Heuvel, D. J., van Lingen, J. N. J., Donega, C. M., Gerritsen, H. C., Meijerink, A., 2002. Time-Resolved Fluorescence Spectroscopy Study on the Photophysical Behavior of Quantum Dots. Journal of Fluorescence 12(1), 69-76.

Varshni, Y. P., 1967. Temperature Dependence of the Energy Gap in Semiconductors. Physica 34, 149-154.

Visaria, R. K., Griffin, R.J., Williams, B. W., Ebbini, E. S., Paciotti, G. F., Song, C. W., Bischof, J. C., 2006. Enhancement of tumor thermal therapy using gold nanoparticle–assisted tumor necrosis factor-A delivery. Molecular Cancer Therapeutics 5(4), 1014-1020.

Vo-Dinh, T., 2004. Nanobiosensors. In: Encyclopedia of Nanoscience and Nanotechnology 6, 53-60.

Walker, G. W., Sundar, V. C., Rudzinski, C. M., Wun, A. W., Bawendi, M. G., Noceraa, D. G., 2003. Quantum-dot optical temperature probes. Applied Physics Letters 83(17), 3555-3557.

Wang, H.-Z., Wang, H.-Y., Liang, R.-Q., Ruan, K.-C.,2004. Detection of Tumor Marker CA125 in Ovarian Carcinoma Using Quantum Dots. Acta Biochimica et Biophysica Sinica 36(10), 681–686.

Wang, L. G. , Pennycook, S. J., Pantelides, S. T., 2002. The Role of the Nanoscale in Surface Reactions: CO2 on CdSe. Physical Review Letters 89(7), 075506.

Wang, L.-W., 2001. Calculating the Influence of External Charges on the Photoluminescence of a CdSe Quantum Dot. Journal of Physical Chemistry 105, 2360-2364.

Wang, S., Mamedova, N., Kotov, N. A., Chen, W., Studer, J., 2002. Antigen/Antibody Immunocomplex from CdTe Nanoparticle Bioconjugates. Nano Letters 2(8), 817-822.

Wang, Z., Lvy, R., Fernig, D. G., Brust, M., 2006. Kinase-Catalyzed Modification of Gold Nanoparticles: A New Approach to Colorimetric Kinase Activity Screening. Journal of the American Chemical Society 128(7), 2214-2215.

Wang, Z., Ma, L., 2009. Gold nanoparticle probes. Coordination Chemistry Reviews (article in press), doi:10.1016/j.ccr.2009.01.005

Wargnier, R., Baranov, A. V., Maslov, V. G., Stsiapura, V., Artemyev, M., Pluot, M., Sukhanova, A., Nabiev, I., 2004. Energy Transfer in Aqueous Solutions of Oppositely Charged CdSe/ZnS Core/Shell Quantum Dots and in Quantum Dot−Nanogold Assemblies. Nano Letters 4(3), 451-457.

Wei, H., Li, B., Li, J., Wang, E., Dong, S., 2007. Simple and sensitive aptamer-based colorimetric sensing of protein using unmodified gold nanoparticle probes. Chemical Communications 3735–3737.

Weisbecker, C. S., Merritt, M. V., Whitesides, G. M., 1996. Molecular Self-Assembly of Aliphatic Thiols on Gold Colloids. Langmuir 12, 3763-3772.

Willard, D. M., Carillo, L. L., Jung, J., Orden, A. V., 2001. CdSe−ZnS Quantum Dots as Resonance Energy Transfer Donors in a Model Protein−Protein Binding Assay. Nano Letters 1(9), 469-474.

Wu, X., Liu, H., Liu, J., Haley, K. N., Treaway, J. A., Larson, J. P., Ge, N., Peale, F., Bruchez, M. P., 2002. Immunofluorescent labeling of cancer marker Her2 and other cellular targest with semiconductor quantum dots. Nature Biotechnology 21, 41-46.

Xu, H., Sha, M. Y., Wong, E. Y., Uphoff, J., Xu, Y., Treadway, J. A., Truong, A., O'Brien, E., Asquith, S., Stubbins, M., Spurr, N .K., Lai, E, H., Mahoney, W., 2003. Multiplexed SNP genotyping using the QbeadTM system: a quantum dot-encoded microsphere-based assay. Nucleic Acids Research 31(8), e43.

Xu, X., Han, M. S., Mirkin, C. A., 2007. A Gold-Nanoparticle-Based Real-Time Colorimetric Screening Method for Endonuclease Activity and Inhibition. Angewandte Chemie International ed. 46, 3468 –3470.

Xue, C., Arumugam, G., Palaniappan, K., Hackney, S. A., Liu, H., Liu, J., 2005. Construction of conjugated molecular structures on gold nanoparticlesvia the Sonogashira coupling reactions. Chemical Communications 1055–1057.

Yurkin, M. A., Hoekstra, A. G., 2007. The discrete dipole approximation: An overview and recent developments. Journal of Quantitative Spectroscopy & Radiative Transfer 106, 558–589.

Zhang, H., Schmid, G., Hartmann, U., 2003. Reduced Metallic Properties of Ligand-Stabilized Small Metal Clusters. Nano Letters 3(3), 305-307.

Zhao, W., Brook, M. A., Li, Y., 2008. Design of Gold Nanoparticle-Based Colorimetric Biosensing Assay. ChemBioChem 9, 2363 – 2371.

Zhao, W., Lam, J. C. F., Chiuman, W., Brook, M. A., Li, Y., 2008. Enzymatic Cleavage of Nucleic Acids on Gold Nanoparticles: A Generic Platform for Facile Colorimetric Biosensors. Small 4(6), 810–816.

Zhelev, Z., Jose, R., Nagase, T., Ohba, H., Bakalova, R., Ishikawa, M., Baba, Y., 2004. Enhancement of the photoluminescence of CdSe quantum dots during long-term UV-irradiation: privilege or fault in life science research? Journal of Photochemistry and Photobiology B: Biology 75, 99–105.

Zhong, Z., Patskovskyy, S., Bouvrette, P., Luong, J. H. T., Gedanken, A., 2004. The Surface Chemistry of Au Colloids and Their Interactions with Functional Amino Acids. Journal of Physical Chemistry B 108(13), 4046-4052.

Zhou, D., Ying, L., Hong, X., Hall, E. A., Abell, C., Klenerman, D., 2004. Compact Functional Quantum Dot−DNA Conjugate: Preparation, Hybridization, and Specific Label-Free DNA Detection. Langmuir 24(5), 1659-1664.

Zhu, L., Ang, S., Liu, W.-T., 2004. Quantum Dots as a Novel Immunofluorescent Detection System for Cryptosporidium parvum and Giardia lamblia. Applied and Environmental Microbiology 70(1), 597–598.

Zrenner, A., Ester, P., Vasconcellos, S. M., Hübner. M. C., Lackmann, L., Stufler, S., Bichler, M., 2008. Coherent optoelectronics with single quantum dots. Journal of Physics: Condensed Matter 20, 454210.